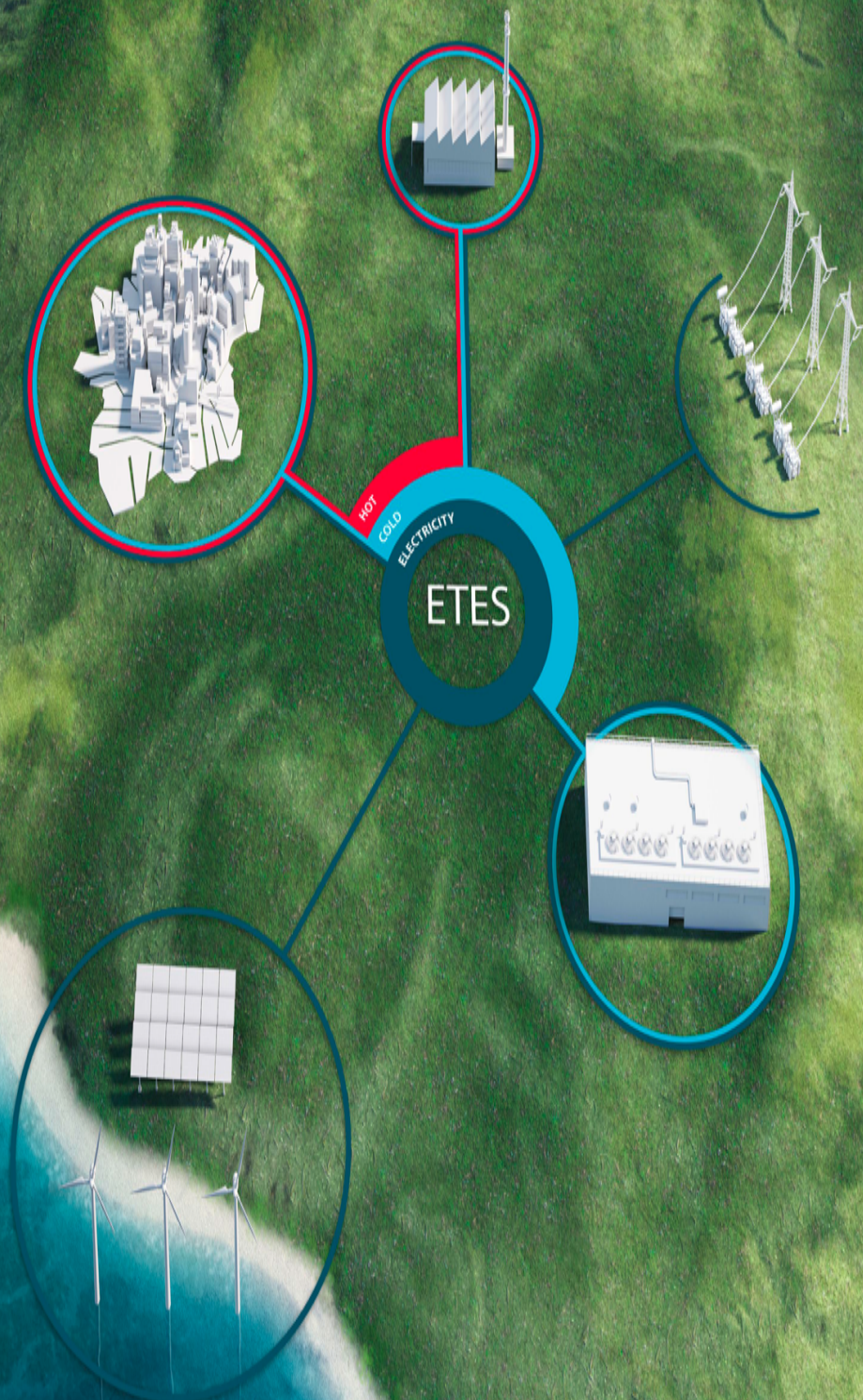


Pumped Thermal Energy Storage

Thermodynamic Modelling
And Optimization Of Waste
Heat Integrated Rankine PTES
System

Divyansh Gautam



Pumped Thermal Energy Storage

Thermodynamic Modelling And Optimization Of Waste Heat Integrated Rankine PTES System

Course Code: ME55035

Master Of Science Thesis

by

Divyansh Gautam

November 22, 2022

in partial fulfillment of the requirements for the degree of
Master of Science: Energy, Flow & Process Technology
at the Delft University of Technology,

Student number: 5226821
Project duration: February 25, 2022 – November 25, 2022
Thesis committee: Prof. dr. ir. Sikke Klein, TU Delft, supervisor
Prof. dr. ir. Rene Pecnik, TU Delft, supervisor
Prof. dr. ir. Kamel Hooman, TU Delft, examiner

Faculty of Mechanical, Maritime and Materials Engineering (3mE) · Delft University of Technology

Technische Universiteit Delft

Department of
Process & Energy

The undersigned hereby certify that they have read and recommend to the Faculty of Mechanical,
Maritime and Materials Engineering (3mE) for acceptance of the thesis entitled

Pumped Thermal Energy Storage

Thermodynamic Modelling And Optimization Of Waste Heat Integrated
Rankine PTES System

by

Divyansh Gautam

in partial fulfillment of the requirements for the degree of
Master of Science: Energy, Flow & Process Technology

Dated: November 22, 2022

Supervisor (s):

Prof.dr.ir. Sikke Klein

Prof.dr.ir. Rene Pecnik

Reader(s):

Prof.dr.ir. Kamel Hooman

Faculty of Mechanical, Maritime and Materials Engineering (3mE) · Delft University of Technology

Abstract

At present, there is a world wide awareness and concern on how the global warming could impact the daily lives and the need to switch to renewable sources of energy. Commercially, various green energy technologies such as hydro, wind, solar, nuclear fission, etc. are being used to harness their stored energy and convert it into electricity. However, amongst these, the natural sources of energy are limited in the operation by their intermittent nature. This potentially leads to the instability of the power grid system. Hence, it is difficult to replace the existing conventional fossil fired energy generation systems with their renewable counterparts, unless and until, a flexibility is introduced to damp the intermittency of renewable sources of energy.

A Pumped Thermal Energy Storage (PTES) system, which uses a combination of heat pump and heat engine to store electricity in form of heat and convert the heat back to electricity, could efficiently provide an intraday to multiday flexibility. However, the literature reveals that this technology is not mature enough and require enhanced research and experimental work.

The scope of this thesis includes a conceptual design, steady-state modelling, and optimization of a waste heat integrated PTES, alternatively called as Compressed Heat Energy Storage (CHEST) system. Two configurations of CHEST system were analysed: (i) CHEST with latent heat storage, and (ii) CHEST with sensible heat storage. A combination of R1233zD as a working fluid and sunflower oil as a sensible thermal energy storage medium were selected and a Phase Change Material (PCM) as a latent heat storage medium. Towards this end, a sensitivity analysis is performed to examine the effect of various design parameters on the performance of the system. It is found that CHEST systems are not suitable for high temperature storage applications ($> 200^{\circ}\text{C}$). Further, the effect of superheating in a heat pump, effect of waste heat source temperature on system performance is investigated.

An optimization study is conducted on CHEST with sensible storage configuration to use a single heat exchanger for charging and discharging cycle during sensible heat transfer with storage medium. A detailed comparison between the two configurations have been performed. Most notably a trade-off has to be set between the performance and economic viability of the system.

Finally, the integration of the optimised sensible heat storage configuration with a solar powered alkaline electrolyser is evaluated. A 30 MW of heat from the electrolyser unit is considered to be recovered with the help of CHEST system. Towards the end, a preliminary design of the CHEST components (heat exchangers and turbomachinery) is provided to estimate the overall sizing and performance characteristics of the components.

*Divyansh Gautam
Delft,
November 22, 2022*

Acknowledgements

With the completion of the 9 month long thesis, my education at Delft University of Technology comes to an end. I would like to use this opportunity to thank all those who helped me to push my boundaries and attain what I have today.

First of all, I would like to express my deep gratitude towards my thesis supervisors, Prof.dr.ir. Sikke Klein and Prof.dr.ir. Rene Pecnik, who provided me this opportunity to work under their expertise. Considering the novelty of the project, they helped me to gather all the required resources to complete this project. Right from Day 1, they always stood besides me to check on my progress and guided me through the right path. The weekly meetings often got extended because of the healthy and open discussion amongst us. They made me learn to think as an engineer and the art to keep things simple.

Further, I would like to thank all the faculty members of the P&E department who took the challenge to train us through the COVID-19 period. I am deeply grateful to my course professors who gave me a deep insight into different subjects. This made me capable to attempt and complete such an interesting and unique project. I also express my sincere regards to Prof.dr.ir. Kamel Hooman for being in the exam committee and reading and evaluating my thesis.

I am just in-debt to the selfless devotion of my parents for tailoring my career towards a successful path. They have always supported me in all possible ways, either emotionally, mentally or financially. I will always be grateful to my parents who sacrificed their personal life to make me stand here. I would also like to thank my sister, who has always been a best friend to me.

Last, but not the least, I would like to thank all my friends here in Delft and in India, with whom I could share my hard times and happy moments.

*Divyansh Gautam
Delft,
November 22, 2022*

Contents

Abstract	iii
Acknowledgements	v
List of Figures	ix
List of Tables	xiii
Nomenclature	xvi
1 Introduction	1
1.1 Energy Storage	3
1.1.1 Classification	3
1.1.2 Comparison of Energy Storage Systems	4
1.2 Electro-Thermal Energy Storage	6
1.2.1 Background & History	6
1.2.2 Overview and Applications	7
1.3 Thesis Overview	9
2 Pumped Thermal Energy Storage	11
2.1 Introduction	11
2.2 Archetype of Pumped Thermal Energy Storage	12
2.2.1 Brayton PTES	12
2.2.2 Rankine PTES	15
2.2.3 Performance Parameters	19
2.3 Rankine PTES - Waste Heat Integration/CHEST	21
2.4 Literature Cases	23
2.4.1 Literature case-I: DLR PTES.	23
2.4.2 Literature case-II: MAN/ABB-PTES	25
2.5 Working Fluid & Storage Medium for CHEST system	28
2.5.1 Selection criteria of working fluids	28
2.5.2 Working fluid comparison	31
2.5.3 Thermal energy storage medium	32
2.6 PTES Cycle Components	34
2.6.1 Heat exchange device	34
2.6.2 Turbomachinery	38
2.7 Research Objectives, Scope and Goal	41
2.8 Thesis Outline	42
3 Thermodynamic Design of CHEST	43
3.1 Introduction	43
3.2 Thermodynamic Model Development	44
3.2.1 Model objectives	44
3.2.2 Design input & output parameters	45
3.2.3 Design Assumptions	45
3.3 Subsystem Models	45
3.3.1 Working fluid model	45
3.3.2 Heat pump model.	46
3.3.3 Heat engine model	48
3.3.4 Thermal energy storage model	49

3.4	Sensitivity Analysis	52
3.4.1	Storage Temperature	52
3.4.2	Waste heat temperature	55
3.5	Case-I: CHEST with High Temperature Latent Storage	56
3.5.1	Input parameters	56
3.5.2	Results	58
3.6	Case-II: CHEST with High Temperature Sensible Storage	61
3.6.1	Input Parameters	61
3.6.2	Results	63
3.6.3	Optimization	65
3.6.4	Results	68
3.7	Design Comparison	71
4	Equipment Design	73
4.1	Introduction	73
4.2	CHEST Unit Coupled With Solar Powered Alkaline Electrolyser.	73
4.2.1	Thermodynamic cycle results for CHEST system	75
4.3	Heat Exchanger Design	78
4.3.1	Shell & Tube HEX	79
4.3.2	Gasketed plate HEX	82
4.4	Turbomachinery Sizing	85
4.4.1	Results	89
4.5	CHEST components overall design	89
5	Summary, Conclusions & Future Work	91
5.1	Future work	92
A	Temperature–Entropy (T-S) vapor saturation curve	93
B	Optimised Parameters for Literature Case	95
C	CO₂ Blends	97
D	Computational Model Description	99
E	Heat Exchanger Design	105
E.1	Shell and Tube HEX	106
E.2	Plate Hex	110
E.3	Widom Line	112
	Bibliography	113

List of Figures

1.1	Estimated energy demand due to estimated population growth [91].	1
1.2	Estimated CO ₂ reductions by using renewable energy [44].	2
1.3	Role of energy storage in balancing the non-uniformity between renewable energy supply and demand [46].	2
1.4	Energy storage technologies based on their storage duration and power output [68].	4
1.5	(a) Overview of global installed grid scale electricity storage systems power rating as in 2020 [66], (b) Share in the global total operational energy storage project capacity of 184.7 GW as of 2020 [2].	5
1.6	Charging and dis-charging of Carnot battery system with energy storage [66].	6
1.7	Progress of Carnot battery research [66].	7
1.8	Carnot battery proposed by Cahn, dated 1978 [16].	7
1.9	Possible configurations of ETES/Carnot Battery with typical RTE values, power output and storage duration.	8
1.10	Overview of the Thesis.	9
2.1	A schematic representation of a PTES system with ambient as the low temperature heat source [62].	11
2.2	Schematic of a Brayton PTES: charging (left), and dis-charging (right) with hot and cold storage.	12
2.3	T-S plot for reverse Brayton cycle corresponding to the charging cycle shown in Figure 2.2. The figure depicts a general T-S diagram of Argon.	13
2.4	T-S plot for Brayton cycle corresponding to the discharging cycle shown in Figure 2.2. The figure depicts a general T-S diagram of Argon.	14
2.5	Schematic of a Rankine PTES: Vapor Compression Heat Pump (VCHP) for charging (left), Thermal Energy Storage (TES) (center), and Rankine Cycle (RC) for dis-charging (right) [38].	15
2.6	T-S plot for reverse Rankine cycle corresponding to the charging cycle shown in Figure 2.5, (a) sub-critical mode, & (b) trans-critical mode. The figure depicts a general T-S diagram of CO ₂	16
2.7	T-S plot for Rankine cycle corresponding to the discharging cycle shown in Figure 2.5, (a) sub-critical mode, & (b) trans-critical mode. The figure depicts a general T-S diagram of CO ₂	17
2.8	PTES (left), Thermal Integrated PTES (TIPTES) with hot storage (center) and TIPTES with cold storage (right) [30].	18
2.9	RTE of a Carnot PTES with ambient as low temperature heat sink at temperatures of $T_a = -5, 10, \text{ and } 30 \text{ }^\circ\text{C}$, forming the upper, middle, and the lower efficiency surfaces.	19
2.10	Bad and good match between the cycle and heat sources/sinks. Bad match (upper two cases) reduces the roundtrip efficiency. Good match is on the lower two frames for sensible heat storage (left) and latent heat storage (right) [62].	20
2.11	PFD of a waste heat integrated Rankine PTES system.	21
2.12	T-S plot for a typical CHEST system corresponding to the PFD shown in Figure 2.11, with heat pump cycle in red color, Rankine cycle in blue color and storage in yellow color. The figure shows a T-S plot for isobutane as a working fluid.	22
2.13	RTE of a Carnot PTES with waste heat integration at a fixed ambient temperature, $T_a = 20^\circ\text{C}$, for different pinch of $T_{pinch} = 2, 5, \text{ \& } 10 \text{ K}$, forming the upper, middle and lower efficiency surfaces.	22
2.14	Process diagram of the subcritical PTES with low temperature heat integration [49].	23
2.15	T-S plot for subcritical ORC based PTES with low temperature heat integration while the state points correspond to the PFD shown in Figure 2.14.	24

2.16	Sample plant layout during charging (left) and discharging (right) cycle [62].	25
2.17	Process flow diagram of the TEES plant, max roundtrip solution with superheating before the HP compressor inlet [65].	25
2.18	ABB Base case Configuration: T-S plot with air-cooling corresponding to PFD of charging cycle, Figure 2.17 (left).	26
2.19	Three types of working fluids: dry ($\xi > 0$), isentropic ($\xi = 0$), and wet ($\xi < 0$) [84].	29
2.20	Saturation dome on a $T_r - \bar{s}$ diagram, (a) Effect of ω , (b) Effect of k_c , and (c) Effect of m [74].	30
2.21	Comparison of Butane, 1-Butene, & R1233zd based on (a) Molecular weight, and (b) Latent heat of vaporization.	31
2.22	(a) Specific heat (c_p), and (b) Viscosity (μ) dependence on temperature (T) for different oils.	33
2.23	Sectional view of a shell & tube heat exchanger.	34
2.24	Schematic of a gasketed plate heat exchanger.	36
2.25	Q-T diagram for <i>LMTD</i> calculation for a pure counter-current flow.	37
2.26	Schematic of a stage between stator and rotor of a typical axial turbine.	38
2.27	Turbomachines specific speed [40, 72]	39
2.28	Axial and radial compressor characteristics (left), Axial and radial turbine operating characteristics (right) [33]	40
3.1	Conceptual process flow diagram of the CHEST system for the present work.	43
3.2	QT diagram for HP evaporator	46
3.3	E-T diagram depicting energy transfer between heat pump and storage during charging cycle for (a) latent storage, and (b) sensible storage configuration.	47
3.4	E-T diagram depicting energy transfer between storage and heat engine during dis-charging cycle for (a) latent storage, and (b) sensible storage.	48
3.5	QT diagram for heat engine condenser based on the PFD shown in Figure 3.1.	49
3.6	A basic T-S diagram showing the cycle integration.	52
3.7	Effect of maximum heat engine cycle temperature and heat pump pressure ratio on (a) RTE, (b) storage size (<i>tonnes</i>) computed for a charging duration of 8 <i>hrs</i> and a waste heat load of 1 MW.	52
3.8	Effect of superheating before the inlet of compressor, with the help of a superheater, on RTE and storage size of the system.	53
3.9	A T-S representation to demonstrate the effect of maximum temperature & pressure on superheating before compressor inlet.	54
3.10	Effect of maximum hp cycle temperature & pressure on amount of superheat needed before the inlet of compressor for (a) sub-critical mode, and (b) trans-critical mode.	54
3.11	(a) Effect of waste heat temperature on the RTE (η_{RTE}) of the CHEST system, (b) T-S representation of varying heat pump evaporator temperature as a result of varying waste heat temperature. The RTE values correspond to a heat pump discharge pressure of 45 bar.	55
3.12	Process flow diagram of CHEST system with a combination of latent and sensible heat storage.	56
3.13	T-S plot for the given input conditions corresponding to the PFD shown in Figure 3.12	58
3.14	Q-T plot representing the total heat exchange between heat pump, storage and heat engine.	58
3.15	Output process flow diagram of CHEST system with a combination of latent and sensible heat storage.	60
3.16	Process flow diagram of the base case with single sensible heat storage.	61
3.17	T-S plot for the given input conditions corresponding to the PFD shown in Figure 3.16	63
3.18	E-T plot representing the total energy exchange between heat pump, storage and heat engine.	63
3.19	Process flow diagram for the optimised case with a common HEX between storage medium and charging-discharging cycles.	65
3.20	T-S plot for the optimized conditions corresponding to the PFD shown in Figure 3.19.	68
3.21	E-T plot depicting the energy transfer between heat pump, storage and heat engine cycles.	68

3.22	Output Process flow diagram for the optimised case with a common HEX between storage medium and charging-discharging cycle.	69
4.1	Plant layout of the CHEST system coupled with solar powered alkaline electrolyser unit.	73
4.2	T-S plot for the optimized conditions corresponding to the plant layout shown in Figure 4.1.	75
4.3	E-T plot depicting the energy transfer between heat pump, storage and heat engine cycles.	75
4.4	Final PFD for the case study.	76
4.5	Isobaric specific heat capacity (C_p) versus temperature (T) plot for R1233zd at an operating pressure of 48.4 bar.	80
4.6	Baljé diagram for single stage compressors [7, 8].	86
4.7	Baljé diagram for single stage turbines [7, 8].	86
4.8	Shaft speed vs Specific speed correlation for a two-stage centrifugal compressor with an overall PR of 9.5.	87
4.9	Shaft speed vs Specific speed correlation for a three-stage axial turbine with an overall PR of 18.5.	88
4.10	T-S plot with updated isentropic efficiency.	90
4.11	E-T plot depicting the energy transfer between heat pump, storage and heat engine cycles.	90
B.1	Range of parameters for optimisation	95
B.2	Optimum Parameters	95
C.1	Effect of dopant on the critical point [28].	97
C.2	Gross cycle efficiency CSP applications [28].	98
C.3	(a) P-T diagram of (C_6F_6) with standard Peng-Robinson EoS [26], (b) T-S diagrams of simple recuperative condensing supercritical cycle for the mixture with 84% CO ₂ molar content [26].	98
D.1	Different Python class defined in thermodynamic model	99
D.2	Steady flow energy process	100
D.3	Heat exchanger block diagram	101
D.4	Compressor and turbine block diagram	101
D.5	Flow through an expansion valve	102
D.6	Thermophysical properties of phase change materials	103
E.1	Tube side friction factors	107
E.2	Tube side heat transfer factors	108
E.3	Shell side friction factors	109
E.4	Shell side heat transfer factors	109
E.5	Widom line for CO ₂ from experimental calculations [93].	112

List of Tables

1.1	Ideal characteristics of long duration energy storage and its significance.	3
1.2	Quantitative & Qualitative comparison of different energy storage technologies [13, 36].	4
2.1	Potential sources of low grade waste heat.	23
2.2	Quantitative & Qualitative comparison of potential PTES technologies.	27
2.3	Thermo-Physical properties of selected working fluids evaluated at $T = 30^{\circ}C$	28
2.4	Thermo-physical properties of common storage mediums.	32
2.5	Fluid velocity limits in shell & tube HEX	35
2.6	Allowable pressure drop for fluids in shell & tube HEX	35
2.7	Operating range of the shell & tube, and gasket plate HEX [81]	36
3.1	Modelling criteria	44
3.2	Input and output parameters of the thermodynamic model.	45
3.3	Thermophysical properties of selected PCM's	50
3.4	Input parameters for the latent storage case shown in Figure 3.12.	57
3.5	Operating conditions for the design configuration shown in Figure 3.12.	60
3.6	Input parameters for the base case shown in Figure 3.16.	62
3.7	Operating conditions for the design configuration shown in Figure 3.16.	64
3.8	Fixed and variable input parameters for the optimized case shown in Figure 3.19.	67
3.9	Heat pump and heat engine cycle optimized state points based on the input parameters given in Table 3.8 for the design configuration shown in Figure 3.19.	69
3.10	Optimized operating conditions for the design configuration shown in Figure 3.19.	70
3.11	Comparison of design configuration and performance parameters of the CHEST system corresponding to Figure 3.12 & 3.19.	71
4.1	Input parameters for the plant layout shown in Figure 4.1.	74
4.2	Optimized operating conditions for the plant layout shown in Figure 4.1.	77
4.3	Input design conditions of heat exchangers in heat pump cycle.	78
4.4	Input design conditions of heat exchangers in heat engine cycle.	78
4.5	Input design conditions of gas cooler for different zones.	79
4.6	Shell and Tube design specifications for the Gas Cooler.	81
4.7	Shell and Tube design specifications for the Common HEX and Gas cooler.	81
4.8	Plate HEX design specifications for evaporator, recuperator and condenser.	84
4.9	Input specifications of the turbomachines of the CHEST system shown in Figure 4.1.	85
4.10	Preliminary design specifications of the compressor and turbine used in the CHEST system shown in Figure 4.1.	89

Nomenclature

Physical symbols

\dot{m}	Mass flow rate [kg/s]
v	Velocity [m/s]
A	Cross-sectional area [m^2]
C_p	Specific heat at constant pressure
C_v	Specific heat at constant volume
E	Energy storage capacity [MWh]
f	Friction factor [-]
G	Mass flux [kg/sm^2]
g	Acceleration due to gravity [m/s^2]
h	Specific enthalpy [kJ/kg]
N	Shaft speed [rpm]
P	Pressure [MPa]
Q	Heat load [MW_{th}]
s	Specific entropy [$kJ/kg - K$]
T	Temperature [$^{\circ}C$]
U	Energy density [MWh/m^3]
U_0	Overall heat transfer coefficient [W/m^2K]
V	Volume [m^3]

Greek Letters

α	Heat transfer coefficient [W/m^2K]
β	Corrugation angle [rad]
η	Efficiency [-]
κ	Specific heat ratio [-]
λ	Thermal conductivity [$W/m - K$]
μ	Dynamic viscosity [$Pa \cdot s$]
ω	Acentric factor [-]
ρ	Density [kg/m^3]

Subscripts

ch charging

$comp$	compressor
$cond$	condenser
cr	critical
dch	discharging
eq	equivalent
$evap$	evaporator
is	isentropic
lat	latent
LV	Liquid-Vapor
rec	recuperator
sat	saturated
sen	sensible
SP	single phase
sup	superheating
th	thermal
TP	two phase
$turb$	turbine

Dimensionless Numbers

Bd	Bond number
Bo	Boiling number
D_s	Specific diameter
M_u	Mach number
N_s	Specific speed
Pr	Prandtl number
Re	Reynolds number

Abbreviations

ANN	Artificial Neural Networks
$CAES$	compressed Air Energy Storage
$CAPEX$	Capital Expenditure
CB	Carnot Battery
$CHEST$	Compressed Heat Energy Storage

<i>CHP</i>	Combined Heat and Power	<i>P2P</i>	Power-to-Power
<i>COP</i>	Coefficient Of Performance	<i>PCM</i>	Phase Change Material
<i>CSP</i>	Concentrated Solar Power	<i>PFD</i>	Process Flow Diagram
<i>DLR</i>	German Aerospace Center	<i>PHES</i>	Pumped Hydro Energy Storage
<i>EH</i>	Electric Heating	<i>PR</i>	Pressure Ratio
<i>ETES</i>	Electro-Thermal Energy Storage	<i>PSH</i>	Pumped Storage Hydropower
<i>GWP</i>	Global Warming Potential	<i>PTES</i>	Pumped Thermal Energy Storage
<i>HE</i>	Heat Engine	<i>PV</i>	Photovoltaic
<i>HEX</i>	Heat Exchanger	<i>RTE</i>	Round Trip Efficiency
<i>HP</i>	Heat Pump	<i>sCO₂</i>	super-critical CO ₂
<i>HTS</i>	High Temperature Storage	<i>SF</i>	Sunflower
<i>LCOES</i>	Levelised Cost Of Energy Storage	<i>SLSQP</i>	Sequential Least Squares Programming
<i>LDES</i>	Long Duration Energy Storage	<i>T – E</i>	Thermo-Economic
<i>LMTD</i>	Log Mean temperature Difference	<i>T – S</i>	Temperature-Entropy
<i>LTS</i>	Low Temperature Storage	<i>TE</i>	Thermal Engine
<i>MBDOE</i>	Million Barrels per Day of Oil Equivalent	<i>TEMA</i>	Tubular Exchangers Manufacturers Association
<i>MGA</i>	Miscibility Gap Alloys	<i>TES</i>	Thermal Energy Storage
<i>NFPA</i>	National Fire Protection Association	<i>TIPTES</i>	Thermally Integrated Pumped Thermal Energy Storage
<i>ODP</i>	Ozone Depletion Potential	<i>VCHP</i>	Vapor Compression Heat Pump
<i>ORC</i>	Organic Rankine Cycle		

Introduction

Growing population entails the increasing demand of energy and electricity irrespective of its source of generation as shown in Figure 1.1. Moreover, the power sector contributes to $\sim 1/3^{rd}$ of the global CO₂ emissions while a greater fraction of energy consumption is dependent on fossil based resources for heating purposes (eg: industrial and residential heating), transport fuels, agricultural applications etc. Following the Paris agreement, emphasis has been made on mitigating the dependence on fossil energy resources and decarbonizing the industry [23]. As such, this necessitates focusing on: (i) tripling or quadrupling the energy production to meet the energy demands, (ii) transformation of fossil fired to renewable energy based power generation, and (iii) maintaining balance between the transition while meeting the transitional costs.

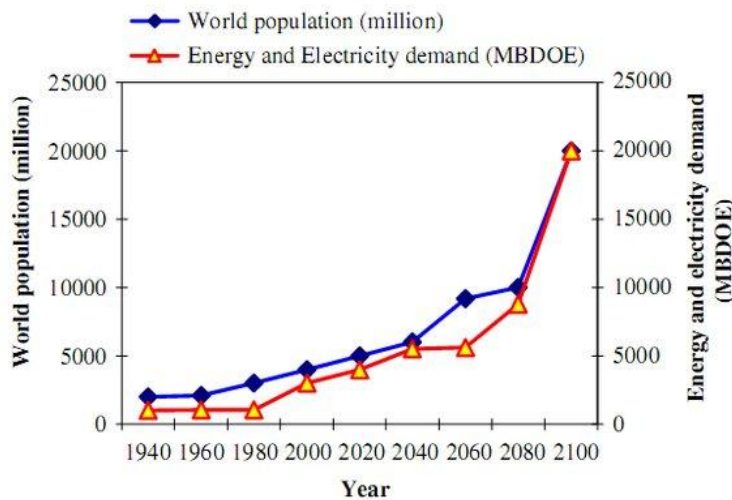


Figure 1.1: Estimated energy demand due to estimated population growth [91].

Although transition to renewable energy supply will greatly contribute in reducing CO₂ emissions, as shown in Figure 1.2, it offers some critical challenges that needs to be addressed: (i) power supply and demand imbalances, (ii) change in transmission flow patterns, and (iii) decrease of system inertia. However, certain energy storage technologies are in place to deal with challenges associated with renewable energy grid balancing, but they are either very expensive and short-timed (eg: Li-ion batteries) or are dependent on geographical location (eg: pumped hydro power). Thus, it is crucial to devise newer technologies that could not only address the issues mentioned above but are also economically viable and environmentally sustainable.

Long Duration Energy Storage (LDES) technologies could be an efficient means of addressing the problems stated above. LDES, in short, is described as '*any technology that can be used to store energy*

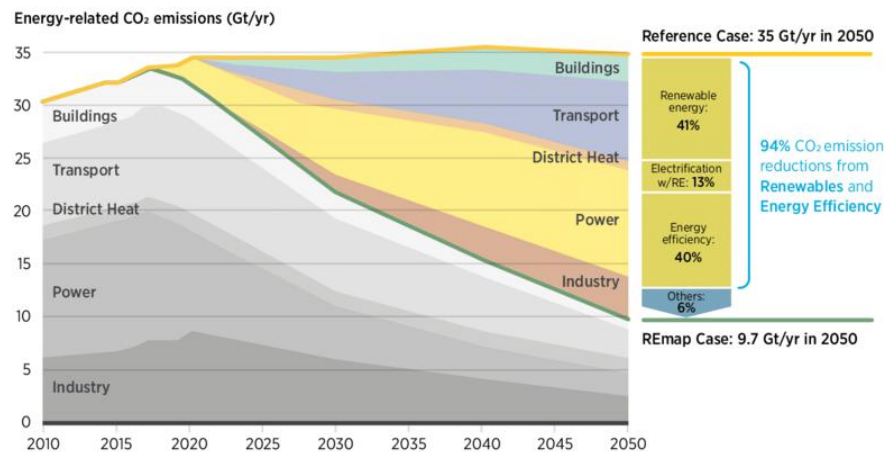


Figure 1.2: Estimated CO₂ reductions by using renewable energy [44].

for extended periods of time and scaled up inexpensively to provide electricity for numerous hours, days, or even weeks, and has the potential to contribute considerably to the economy's decarbonization' [23].

Figure 1.3 depicts, in a very concise manner, how energy storage could resolve the power supply & demand issue of the renewable energy grids. From Figure 1.3, hydro-power (blue profile) provides a constant power output, while wind (green profile) and solar energy (yellow profile) involves climatic dependency. An energy storage system acts as a buffer between the shortage and surplus of energy from the renewable sources in order to maintain the required energy demand. At times of excess energy supply, energy storage system stores this extra energy as depicted by the orange contour in Figure 1.3. On the other hand, when there is an energy deficit, the energy storage releases this energy to fulfill the energy demands as portrayed by the purple contour in Figure 1.3.

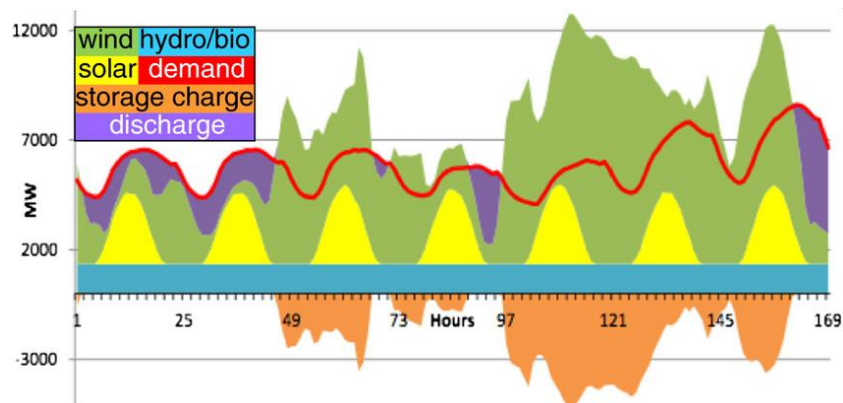


Figure 1.3: Role of energy storage in balancing the non-uniformity between renewable energy supply and demand [46].

Energy storage technologies could be of much help by providing flexibility into the power sector across different spans [23]:

- **Intraday flexibility**:- This provides for the smoothing out of daily changes in supply and demand (capacity < 12 hrs) for eg: peak energy demand in the evening.
- **Multiday/week flexibility**:- Flexibility in balancing supply and demand swings from day to week (capacity- 12 hrs to few weeks) eg: taking weather anomalies into account.
- **Seasonal Flexibility**:- Seasonal storage incorporates flexibility to manage seasonal imbalances in supply and demand (capacity- more than a month) eg: energy demand peaks in winter.

Apart from balancing the supply & demand fluctuations in the renewable energy grid, the energy storage technologies should also comply with certain characteristics as listed in the Table 1.1. However, neither of the energy storage technologies can demonstrate all the characteristics simultaneously, as evident from the Table 1.2. These characteristics have also been outlined in the report published by McKinsey & Company [23].

Ideal characteristics	Significance
De-couple Power & Energy capacities	<ol style="list-style-type: none"> allows for the independent design of charging and discharging cycles provides long term storage without additional power capacity
widely deployable and scalable	<ol style="list-style-type: none"> allows small-scale testing for initial deployment which can be ramped up as the system matures no geographical limitations and can be integrated with existing plants
low storage costs	helps in greater penetration of renewable energy in power grids
high energy density	allows for prolonged energy storage duration without extra costs
long lifetime	it involves a one time investment without the need of frequent replacement
low storage losses	provides a greater utilization of stored energy
high round trip efficiency	indicates higher degree of conversion from power-to-heat-to-power at minimum losses

Table 1.1: Ideal characteristics of long duration energy storage and its significance.

This thesis will be primarily focused on the medium-to-long term storage systems, which claim to enhance the system flexibility and stability, required by an increasing renewable share in the power generation.

1.1. Energy Storage

1.1.1. Classification

Based on the working principle, LDES can be classified into the following four main categories: (i) Mechanical, (ii) Chemical, (iii) Electro-chemical, and (iv) Electro-thermal energy storage technologies as depicted in Figure 1.4.

- Mechanical:** This storage concept utilises the excess electricity to store energy in the form of potential or kinetic energy while exploiting the same to generate power during the electricity demand. For eg: Pumped Storage Hydropower (PSH), Compressed Air Energy Storage (CAES), etc.
- Chemical:** This involves storing energy by means of altering the chemical bonds of certain compounds. For eg: water electrolyser is powered to produce H_2 , which is stored and further used to generate electricity.
- Electro-chemical:** Li-ion battery is a typical example of the electro-chemical energy storage. Batteries use an electro-chemical oxidation-reduction reverse reaction to transform the chemical energy contained in their active components into electric energy. Other examples include: flow batteries, metal air batteries, etc.
- Electro-Thermal:** Electro-thermal energy storage system stores electrical energy in the form of heat. This is later converted back to electricity by means of the thermodynamic power cycles. For eg: pumped thermal energy storage, liquid air energy storage, etc.

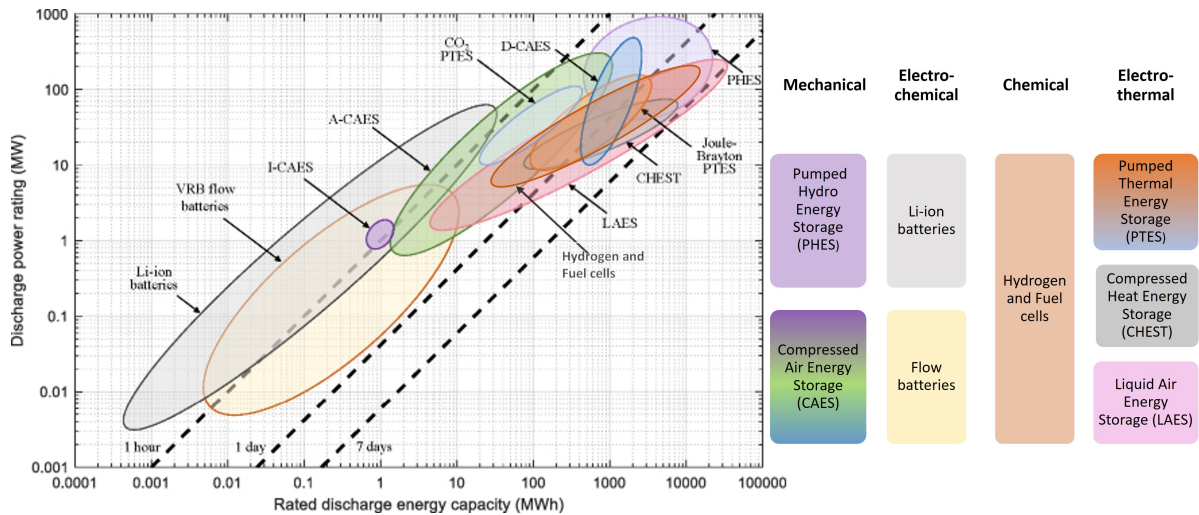


Figure 1.4: Energy storage technologies based on their storage duration and power output [68].

1.1.2. Comparison of Energy Storage Systems

An overview of the different energy storage types in the order of their storage duration and range of power output is given in the Figure 1.4. Both in terms of storage duration and discharge power output, PSH leads in the energy storage systems. Moreover, Thermal Energy Storage (TES) technologies also depict a competitive energy capacity, power output and storage duration as compared to other energy storage systems. A more detailed comparison of different energy storage types based on the characteristics mentioned in Table 1.1 has been listed in Table 1.2.

Storage types	Mechanical		Chemical	Electro-chemical		Electro-thermal
Technology	PSH	CAES	H ₂ production and fuel cells	Li-ion	Flow battery	TES
Development Stage	Commercialised	Initial commercialization	Pilot stage	Commercialised	Initial commercialization	Initial commercialization
Power output (MW)	100-5000	1-400	1e-6 - 50	0.1-50	1-200	0.1-300
Cost range	1504-2422 (\$/kW) 150-242 (\$/kWh)	973-1259 (\$/kW) 97-126 (\$/kWh)	2793-3488 (\$/kW) 279-349 (\$/kWh)	1410-1950 (\$/kW) 350-490 (\$/kWh)	2000-2440 (\$/kW) 500-610 (\$/kWh)	1700-1800 (\$/kW) 20-60 (\$/kWh)
Discharge Duration	several hours to days	several hours to days	several hours to months	minutes to few hours	several hours	several hours
Round Trip efficiency	60-90%	40-80%	20-70%	85-90%	55-85%	30-60%
Energy Density (Watt-hour/litre)	0.2-2	3-12	500-3000	200-600	16-60	50-500
Lifetime (years)	40	30	30	10	15	30
	suitable for large scale (>100 MWh)		suitable for large scale (>100MWh)	suitable for smaller scale (<10 MWh)		Better for industrial to large scale (>10 MWh)
	100% depth of discharge	limited depth of discharge	~50% depth of discharge	Limited depth of discharge		full depth of discharge
	Cheap on very large scale		cheap on large scale	often cheaper on smaller scale		Cheap on large scale
	possible storage losses		possible losses	no storage losses		1% loss per day
	Geographically dependent		location independent	No geographical limitations		location independent

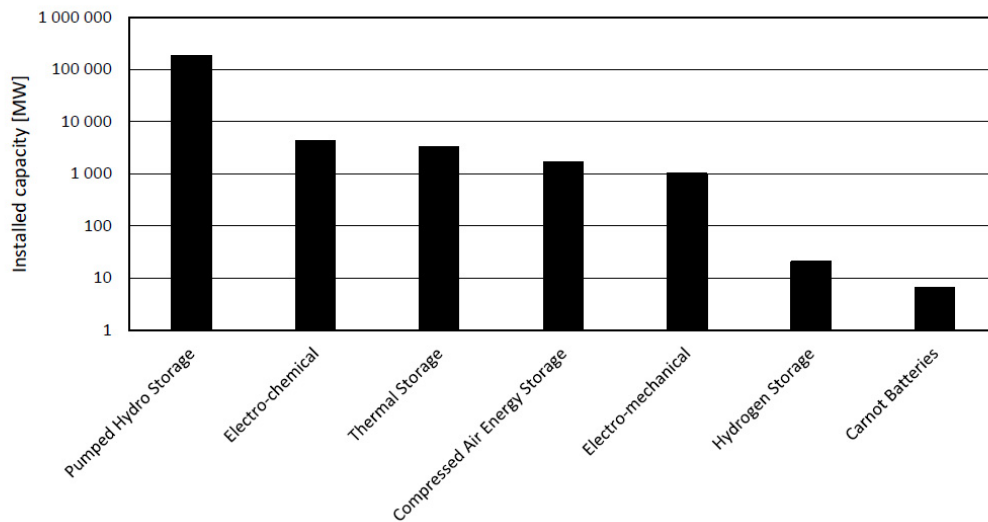
Table 1.2: Quantitative & Qualitative comparison of different energy storage technologies [13, 36].

From Table 1.2, it is obvious that TES possess the potential to be a cost competitive, efficient and environmentally sustainable solution for the renewable grid scale energy storage.

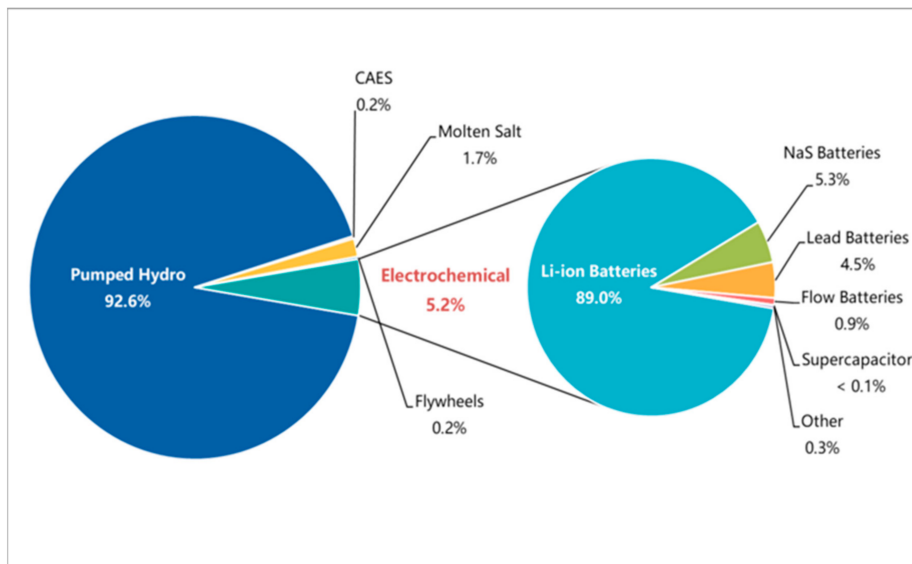
PSH, the first realised solution for grid scale energy storage, has the maximum share (~ 92.6%) of the present total installed capacity of 184.7 GW as shown in Figure 1.5b. PSH is quite simple in its operation, provides long durability, highly efficient and mainly very mature technology. However,

its geographical dependence limits its scalability, since these projects require water resource in its vicinity and huge areas at sufficient elevations to store the water. PSH also has negative social and environmental implications, since construction sites require cutting down vegetation, displacing people and disturbing the natural habitat of the local flora and fauna.

Electro-chemical energy storage has merely ~5% of the total installed capacity but still accounts for 2nd highest share in energy storage, as evident from Figure 1.5. Li-ion batteries holds around 89% of total installed capacity of electro-chemical energy storage while others such as lead batteries, flow batteries, super-capcitors have a very low contribution as shown in Figure 1.5b. Batteries are more attractive for the short scale energy output, since it is quite expensive for large scale energy storage, Table 1.2. While being highly efficient and having large power density, it comes with shorter life time and safety issues (eg: Li-ion batteries can be a fire hazard).



(a)



(b)

Figure 1.5: (a) Overview of global installed grid scale electricity storage systems power rating as in 2020 [66], (b) Share in the global total operational energy storage project capacity of 184.7 GW as of 2020 [2].

TES, on the other hand, is an immature technology and has recently gained interest in the large scale energy storage sector. Low energy storage costs at a larger scale while providing long storage duration is a distinguishing feature of TES. From Figure 1.4, Carnot batteries based on TES (eg: PTES, LAES) exhibit lesser energy density than standard Li-ion batteries, but they are intended to provide higher power ratings. Moreover, Carnot batteries have a long lifetime, are safe to operate and have no social or environmental implications, since they don't require large land mass for their installation and the working fluids chosen are non-hazardous in nature. These features of the Carnot battery make it a more promising solution for the cheap and sustainable energy storage system. Considering these potential aspects of the Carnot battery system, the following section have been tailored to summarise the capabilities of different Carnot battery technologies.

1.2. Electro-Thermal Energy Storage

Electro-Thermal Energy Storage (ETES), also called as Carnot battery, [66], work on the idea of storing electricity as thermal energy during the charging cycle, either in sensible, latent, or thermo-chemical storage, and converting the stored heat into electricity during the discharging cycle (Figure 1.6). Although, Carnot battery holds the lowest share amongst other energy storage solutions (Figure 1.5a), it is a rapidly growing group of technologies (Figure 1.7), which focuses on medium to long duration of energy storage. Compared to the most mature LDES solution, the PSH, Electrochemical & CAES, the overall efficiency of Carnot battery is lower, as listed in Table 1.2. However, over time, the low Levelized Cost of Energy Storage (LCOES) of the Carnot battery will undoubtedly outperform the existing energy storage systems by storing excess cheap renewable energy for a period of hours to several days.

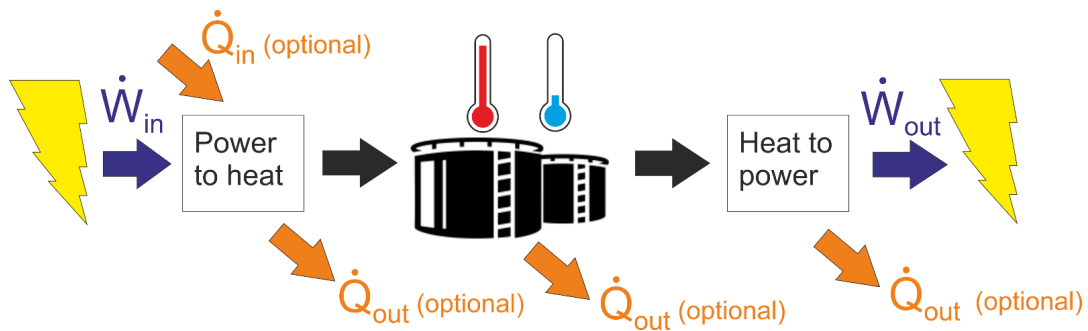


Figure 1.6: Charging and dis-charging of Carnot battery system with energy storage [66].

The ETES systems are characterised by their Round Trip Efficiency (RTE). It is defined as the product of the Coefficient of Performance (COP) of the charging cycle (Power-to-heat) and the efficiency (η = the ability to convert heat into work) of the discharging cycle.

$$\eta_{RTE} = COP_{charging} \times \eta_{discharging}. \quad (1.1)$$

1.2.1. Background & History

The concept of ETES dates back to 20th century. Mehmet Mercangöz et al. (2012) describes the work of Marguerre who proposed a similar set-up in 1924 [62]. His work represented storage of energy partially in the form of heat and partially as compression work against the ambient pressure. However, Cahn (1978) was the first to patent a typical Carnot battery based on reversible heat pumping, as shown in Figure 1.8, which dates back to 1978 [15, 16]. Since then the research in ETES commenced, but was progressing at a very slow pace. However, a sudden increase in the research of ETES is seen in the last decade, as shown in Figure 1.7, which is primarily because of the growing intermittent cheap renewable supply in the power grids and the immense need of electricity storage in large capacities.

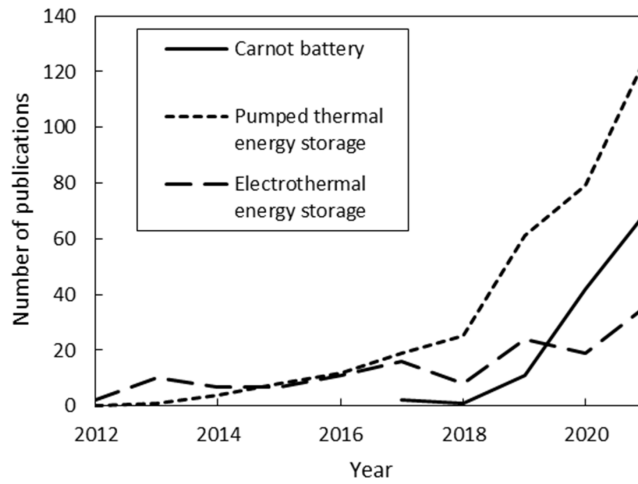


Figure 1.7: Progress of Carnot battery research [66].

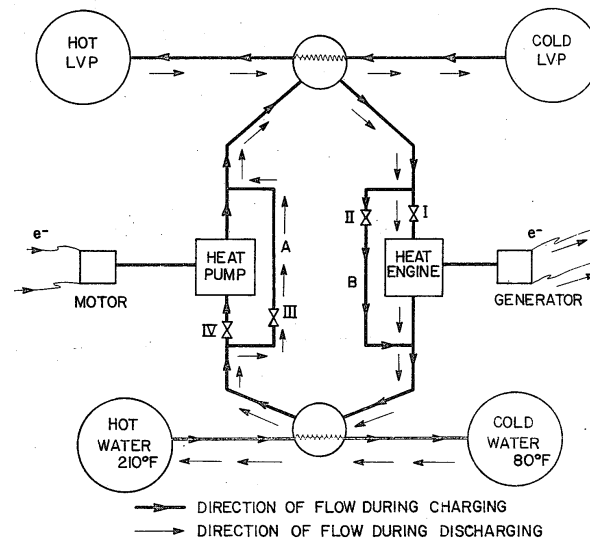


Figure 1.8: Carnot battery proposed by Cahn, dated 1978 [16].

1.2.2. Overview and Applications

Based on the working principle of ETES system, a number of different configurations could be realised. In order to account for these possibilities, a classification of ETES is given in Figure 1.9. ETES has been classified on the basis of three parameters: (i) charging method, (ii) dis-charging method, and (iii) types of thermal energy storage.

With reference to Figure 1.9, an ETES primarily employs either direct electric heating or specific thermodynamic cycles (eg: vapour compression heat pump, Brayton heat pump) to transform excess electrical energy from renewable energy grid into thermal energy. This energy can be stored in sensible TES (eg: by heating volcanic rocks, sand, water in liquid medium, etc.), in latent TES (eg: phase change materials, ice+water at 0°C, etc.) or in thermochemical energy storage (eg: using heat to dissociate metal hydroxides while storing heat as chemical energy and generating heat in the reverse reaction). Finally, a discharging method, either direct heat to power (eg: using thermo-photovoltaic cell) or standard power cycles (eg: Rankine cycle, Brayton cycle, Stirling engine, etc.) can be used to generate electricity.

Theoretically, each method under 'charging' can be coupled with the different methods given under

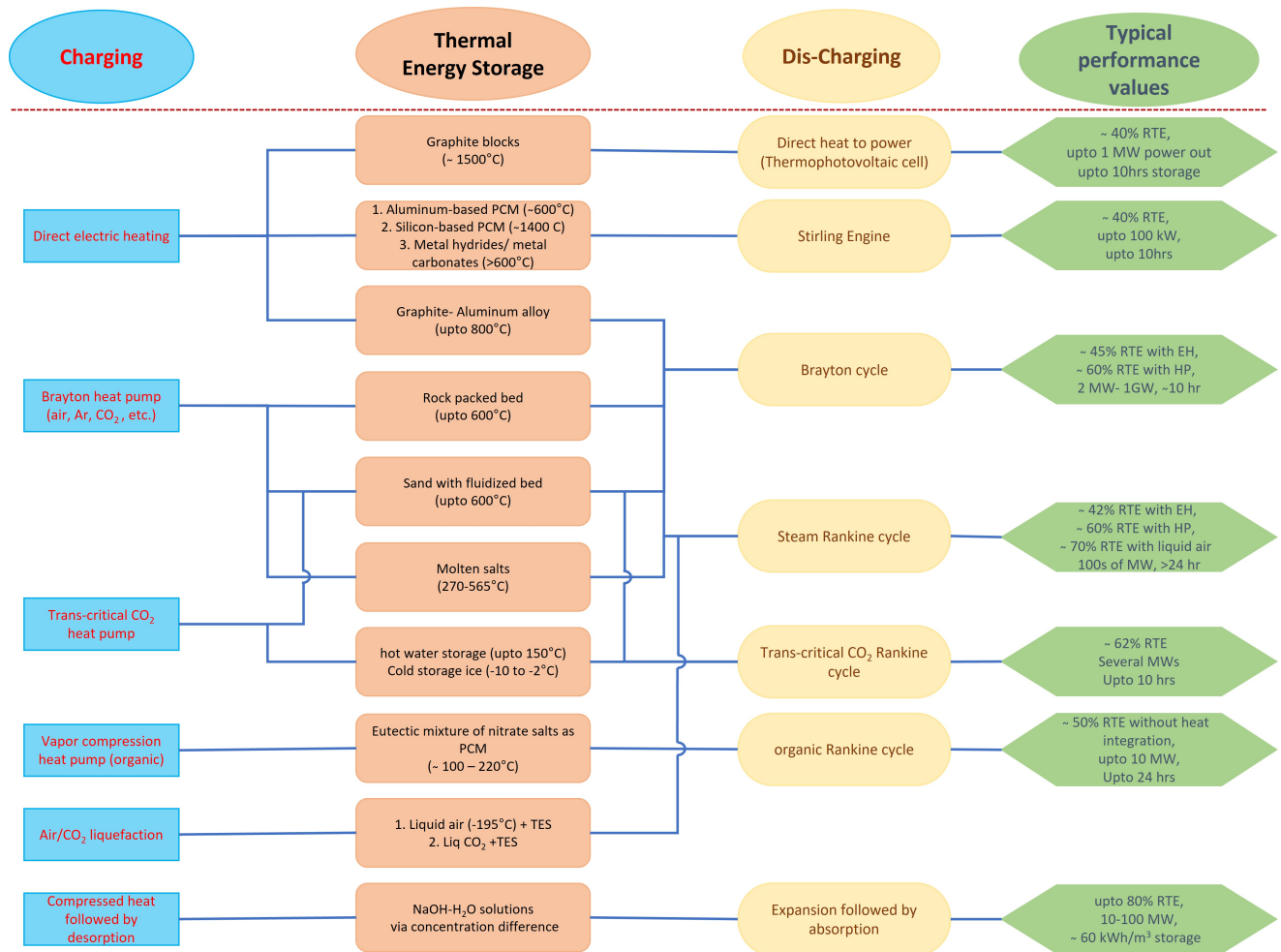


Figure 1.9: Possible configurations of ETES/Carnot Battery with typical RTE values, power output and storage duration.

'dis-charging', while choosing any energy storage medium. From Figure 1.9, for example, if direct electric heating is chosen as the charging method, then either direct heat to power method or any of the thermodynamic power cycles can be chosen as a discharging method, while using either sensible, latent TES or thermochemical energy storage. However, due to the technical limitations, every combination would not be feasible.

Figure 1.9 maps out the feasible configurations of ETES system. These configurations listed out already have a commercial background, i.e. these have been either tested on a pilot scale or are still pending a proof of concept. The commercial development of different configurations can be found in the work of Novotny et al. (2022) [66].

From Figure 1.9, it is obvious that direct electric heating is used as a charging method in order to attain high storage temperatures ($> 600^{\circ}\text{C}$). However, direct electric heating is limited by a COP equal to 1, and thereby, a low RTE of the system. Nevertheless, in order to have improved RTE, electric heating can be used in combination to Brayton heat pumps for HTS [4, 12]. On the other hand, trans-critical Rankine cycle and VCHP are seen to be suitable for low to medium thermal storage with highest RTE of around 60%. Other configurations based on LAES and Lamn Hoingmann process (involves thermo-chemical energy storage) provide much higher efficiencies due to reduced thermodynamic losses.

In general, ETES systems find a wide range of applications. Low temperature configurations find their way in integrating low grade heat to store energy and develop power while also providing options

for district heating and cooling. On a contrary, high temperature ETES configurations have been theoretically demonstrated to integrate with solar fields, nuclear power plants, etc. for storing energy at elevated temperatures.

1.3. Thesis Overview

Previous section presented an overview of the various ETES technologies, which composed of many possible configurations. Of these, Pumped Thermal Energy Storage (PTES) systems could be a promising technology for providing energy storage from intra-day to inter-day situations with a higher power rating (Figure 1.4). This thesis deeply looks into a conceptual development of a PTES system. An overview of the procedure to carry out the main tasks of the thesis has been presented in Figure 1.10. Initially, a literature study is performed for the complete PTES system, which is included in Chapter 2. This involves comparing main PTES technologies and selecting a reliable and simple technology. Moreover, a study is also conducted on various integral components of the PTES system such as: working fluid, storage medium, heat recovery systems and turbomachinery. Based on the literature review, a set of research questions are formulated, which are used as a direction to carry out the main thesis work in Chapter 3-5.

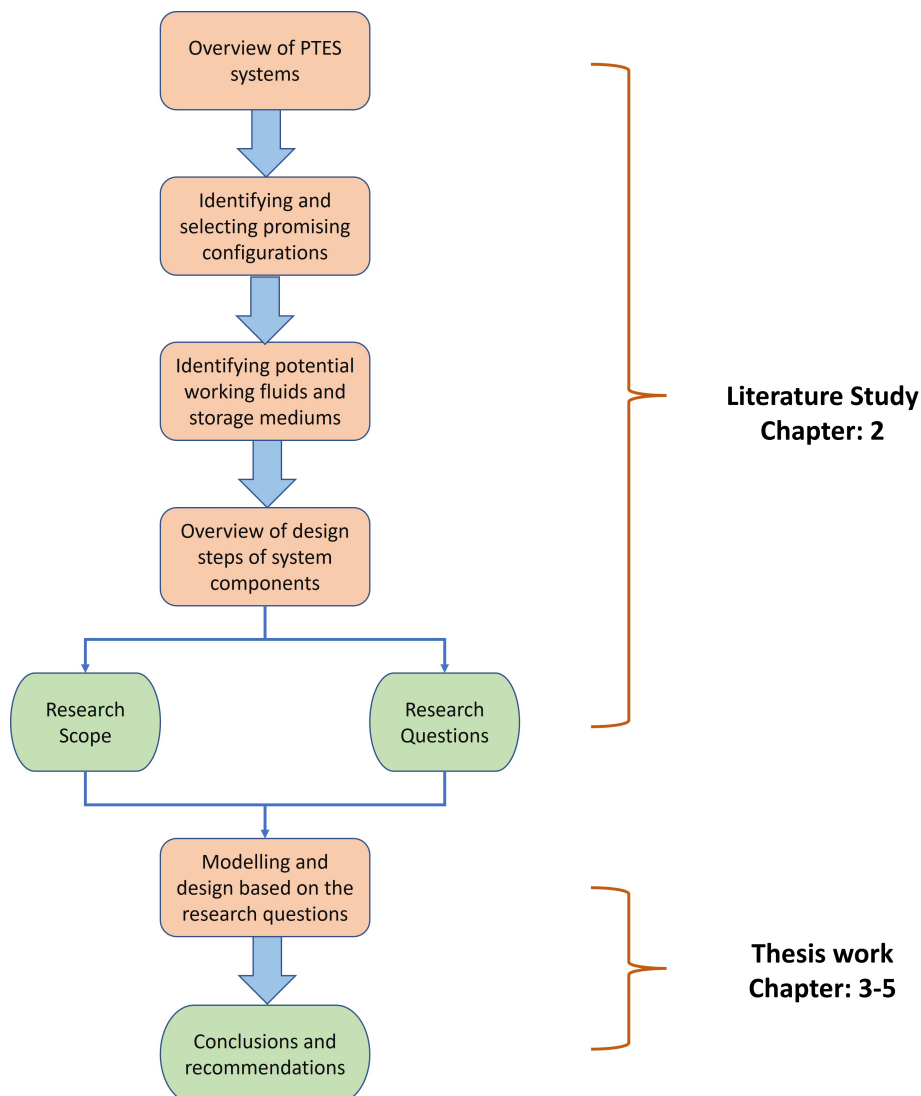


Figure 1.10: Overview of the Thesis.

Pumped Thermal Energy Storage

2.1. Introduction

Pumped Thermal Energy Storage (PTES) makes use of the thermodynamic cycles for its operation. It utilises the concept of a heat pump to upgrade the heat from low temperature to high temperature reservoir during the charging cycle while generating work in the discharging cycle using a heat engine. An important benefit of the PTES system is its ability to deliver high round trip efficiency while providing energy storage from few hours to several days, as shown in Figure 1.4. Moreover, PTES systems exhibit the ability to recover waste heat and transform it to work and thereby increasing the RTE. A schematic of a simple PTES system is shown in Figure 2.1.

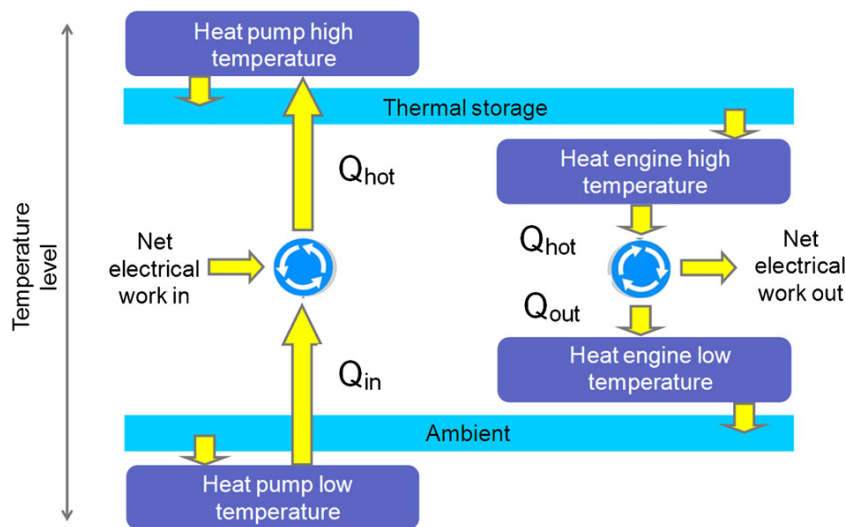


Figure 2.1: A schematic representation of a PTES system with ambient as the low temperature heat source [62].

The Figure 2.1 depicts a combination of a Carnot heat pump and heat engine operating between same temperature levels. The heat pump is allowed to operate between a low temperature source (ambient) and a high temperature thermal energy storage (HT-TES). An external electrical work is fed to the heat pump, which makes it possible to pump heat from a low temperature (Q_{in}) to high temperature storage (Q_{hot}). A heat engine, on the other hand, transforms the heat absorbed from the HT-TES (Q_{hot}) into electrical work, while rejecting a part of the heat (Q_{out}) back to the low temperature sink (ambient). The working fluid, TES and the design of thermodynamic cycle are an integral component of a PTES system.

A PTES system is mainly characterised by its round trip efficiency (η_{RTE}), which is defined as the ratio of the net work output from the heat engine to the net work input to the heat pump. For an ideal/Carnot

PTES system, as shown in Figure 2.1, the RTE can be formulated as a function of heat source and sink temperatures as given in Equation (2.2).

$$\eta_{RTE} = \frac{W_{elec,OUT}}{W_{elec,IN}} = COP_{HP} * \eta_{HE} \quad (2.1)$$

$$\eta_{RTE} = \frac{T_{high-HP}}{T_{high-HP} - T_{low-HP}} * \frac{T_{high-HE} - T_{low-HE}}{T_{high-HE}} \quad (2.2)$$

where, $T_{high-HE}$, T_{low-HE} indicate the high and low operating temperatures of a heat engine while $T_{high-HP}$, T_{low-HP} represent the high and low operating temperatures of a heat pump respectively.

Further, a PTES system can operate in three different thermodynamic modes: sub-critical, trans-critical and super-critical mode, depending upon the state of the working fluid.

- **sub-critical:** If the working fluid, through its complete course of a thermodynamic cycle, tends to be below its critical point, it would be termed as sub-critical cycle, eg: organic Rankine cycle, ammonia refrigeration cycle, etc.
- **trans-critical:** If the working fluid tends to be above its critical point in any one of the thermodynamic process constituting a thermodynamic cycle, it would be named as trans-critical cycle, eg: CO₂ heat pump cycle, etc.
- **super-critical:** If the working fluid, through its complete course of a thermodynamic cycle, tends to be above its critical point, it would be termed as super-critical cycle, eg: air Brayton cycle.

Till date, most of the PTES technologies under research is based on either Rankine or Brayton cycle system while some involve Stirling cycles [31, 66]. Novotny et al. (2022) reports the use of some hybrid thermodynamic cycles (eg: Combined Brayton & Rankine cycle) on a conceptual level [66]. However, the following sections will only consider Rankine & Brayton cycle systems due to their wide application, and further discuss the constituent elements of a PTES system.

2.2. Archetype of Pumped Thermal Energy Storage

2.2.1. Brayton PTES

A Brayton PTES consists of a Brayton heat pump, Brayton heat engine and a sensible TES as shown in the Figure 2.2. The system operates on reverse Brayton cycle during charging while use Brayton cycle for discharging, the individual charging and discharging cycles have been discussed in following sections.

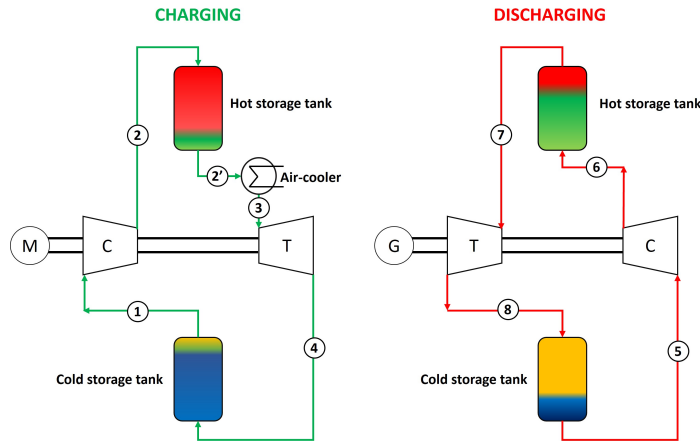


Figure 2.2: Schematic of a Brayton PTES: charging (left), and dis-charging (right) with hot and cold storage.

Reverse Brayton cycle - charging

A Brayton heat pump is used for charging the TES, which follows a reverse Brayton cycle. A simple single-stage configuration for the charging process is shown on the left side in Figure 2.2. An ideal reverse Brayton cycle has four internal reversible processes (two isobaric and two isentropic process) marked by the order 1-2s-3-4s-1 on the T-S diagram as shown in Figure 2.3:

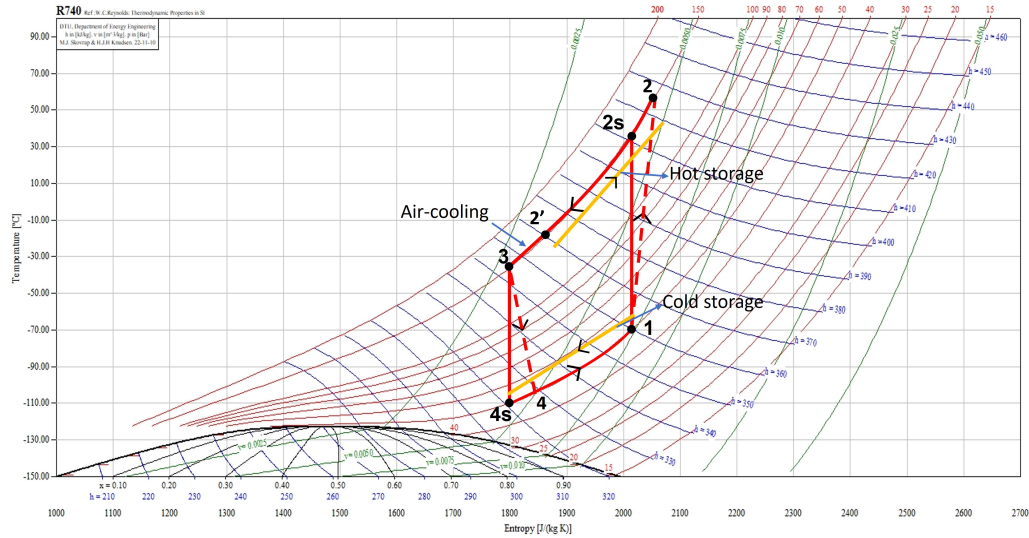


Figure 2.3: T-S plot for reverse Brayton cycle corresponding to the charging cycle shown in Figure 2.2. The figure depicts a general T-S diagram of Argon.

- 1-2s: Isentropic compression; 1-2: real compression
- 2-3: Isobaric heat rejection to hot storage
- 3-4s: Isentropic expansion; 3-4: real expansion
- 4-1: Isobaric heat addition from cold storage

A Brayton heat pump is characterised by a non-isothermal heat addition (4-1) and heat rejection process (2-3), which favors a sensible heat transfer at the source and sink. Further, it involves a super-critical thermodynamic cycle, where the working fluid is in single phase through out the cycle, as is evident from Figure 2.3. This facilitates using the work produced in the expansion process to partly compress the working fluid. This leads to defining the performance of a Brayton heat pump as follows:

$$\text{COP}_{HP} = \frac{Q_H}{W_{comp} - W_{turb}} = \frac{Q_{2-3}}{W_{1-2} - W_{3-4}}. \quad (2.3)$$

Traditionally, Brayton heat pumps had a limited application in cooling and heating sectors, owing to its modest performance compared to vapor compression cycles [6]. This has been attributed to the high specific volume of working fluid in supercritical conditions, which requires a large work input per unit of head output. However, operating the cycle in a selected region, for example: expansion/compression near critical point, provides substantial reduction in specific volume and further reduction in compression/expansion work. This leads to better thermodynamic performance of Brayton heat pump, which could be comparable to its two-phase counterpart [6].

Brayton cycle - discharging

A Brayton heat engine is used for producing work from the heat stored in the TES. It follows a simple Brayton cycle, alternatively called as gas turbine cycle, as shown on the right in Figure 2.2. An ideal Brayton cycle is composed of 4 major components: (i) gas cooler (cold storage), (ii) a compressor, (iii) gas heater (hot storage), and (iv) a gas turbine. The main thermodynamic processes in an ideal Brayton cycle is shown in Figure 2.4:

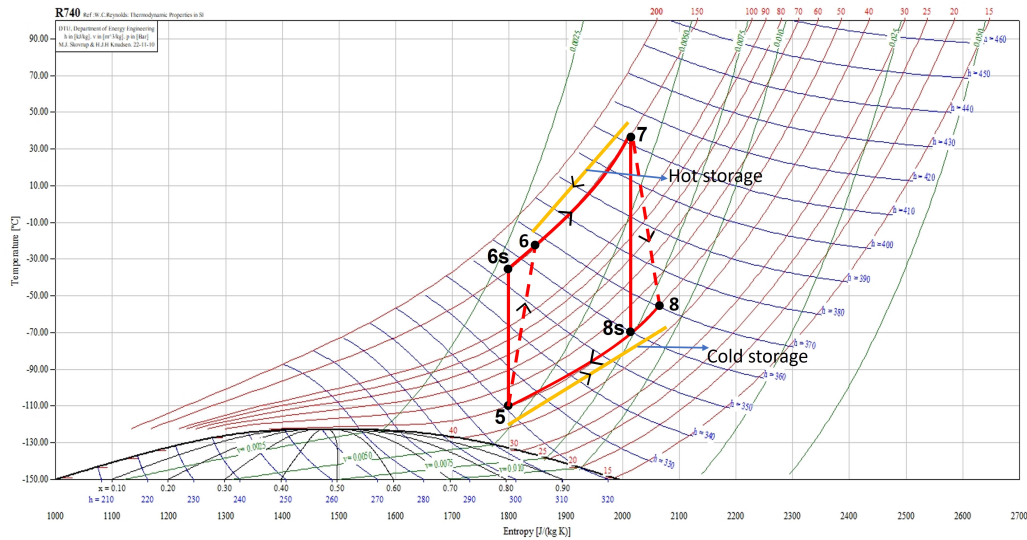


Figure 2.4: T-S plot for Brayton cycle corresponding to the discharging cycle shown in Figure 2.2. The figure depicts a general T-S diagram of Argon.

- 5-6s : Isentropic compression; 5-6: Real compression
- 6-7 : Isobaric heat addition from hot storage
- 7-8s : Isentropic expansion; Real expansion
- 8-5 : Isobaric heat rejection to cold storage

Brayton cycle can be operated at very high temperatures, beyond 500 °C for absorbing heat from hot storage. This brings its wide application as a power cycle in high temperature industries such as: concentrated solar plants (CSP), nuclear reactors, etc. Based on the working state of the operating fluid, Brayton cycles operate in super-critical mode. This allows the turbine and compressor to be mounted on a same shaft so that a part of turbine work output can be used to provide the work input of the compressor. This leads to defining the thermal efficiency of an ideal Brayton cycle as follows,

$$\eta_{th} = \frac{W_{turb} - W_{comp}}{Q_H} \quad (2.4)$$

$$= 1 - \frac{1}{PR^{(\kappa-1)/\kappa}} \quad (2.5)$$

where, PR is the pressure ratio (p_2/p_1) and $\kappa = c_p/c_v$, specific heat ratio. Equation (2.5) represents the ideal Brayton cycle efficiency (i.e. considering isentropic efficiency of compressor and turbine = 1). In general, increasing the PR (Equation (2.5)), could be a straightforward method to improve the efficiency of a Brayton cycle. Moreover, the cycle efficiency is negatively impacted by the turbomachinery efficiency and pressure losses, which is discussed in later sections. The overall power output from such cycles could be between 30-500 MW_e depending upon the performance requirement of the gas turbine while an efficiency of ~40% could be achieved, which is comparable to the efficiency of Rankine cycles [79].

Working fluid and storage medium

Considering the operating conditions of a Brayton PTES, air and other inorganic fluids such as Ar [24, 53], CO₂ [4, 19], N₂ [67], etc. are the most suitable and prominently used working fluids pertaining to their high thermal stability.

The non-isothermal heat transfer in Brayton PTES system across the storage leads to using a sensible storage medium. The potential storage mediums for this system are: solid rock packed beds, sand, molten salts, etc.

2.2.2. Rankine PTES

PTES based on the Rankine system combine the Rankine heat pump and a standard Rankine heat engine, which follows vapor compression refrigeration cycle and Rankine cycle respectively, as shown in Figure 2.5. Meanwhile, the cycles operate between two thermal energy storage, a cold TES and a hot TES. The working principle of each individual cycle is discussed in the following sections.

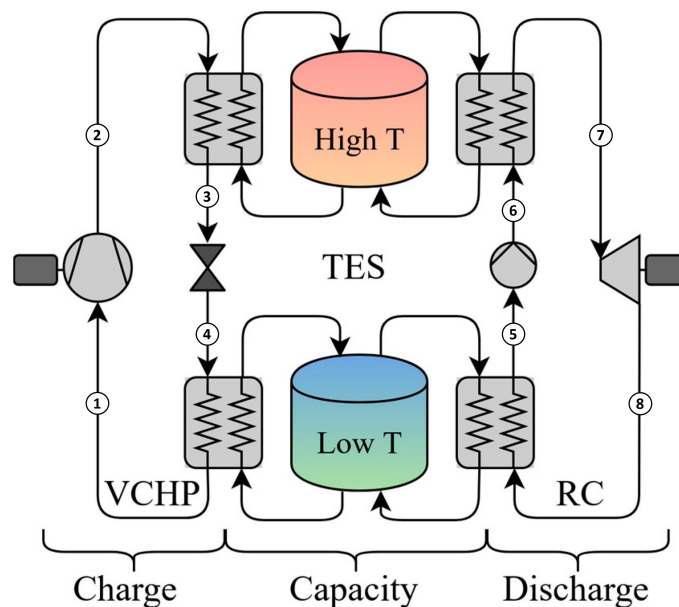


Figure 2.5: Schematic of a Rankine PTES: Vapor Compression Heat Pump (VCHP) for charging (left), Thermal Energy Storage (TES) (center), and Rankine Cycle (RC) for dis-charging (right) [38].

Reverse Rankine cycle - charging

A Rankine PTES uses reverse Rankine cycle, which operates on the vapor compression heat pump/refrigeration principle for the charging of the TES, as shown on the left in Figure 2.5. A heat pump cycle undergoes the following thermodynamic processes:

- 1-2s: Isentropic compression; 1-2: Real compression
- 2-3: Isobaric heat rejection to hot storage
- 3-4: Isenthalpic expansion
- 4-1: Isobaric heat absorption from cold storage

The underlying principle of reverse Rankine cycle/refrigeration cycle is marked by heat exchange at the low temperature heat source/sink or the cold storage in the two phase (liquid-vapor) region (4-1) as shown in Figure 2.6. The excess renewable power supply is used to power the compressor, which converts a low grade heat to a higher grade (1-2), thereby storing heat in a high temperature storage. A

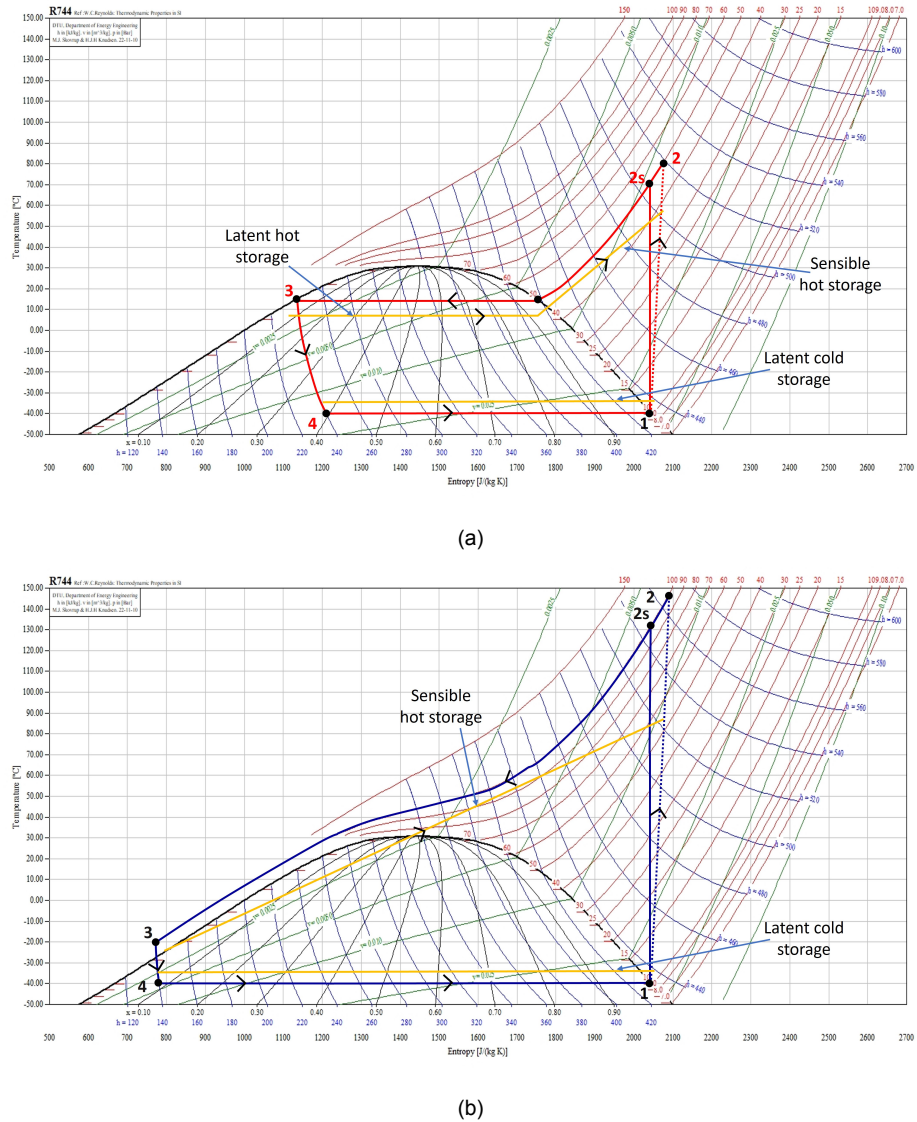


Figure 2.6: T-S plot for reverse Rankine cycle corresponding to the charging cycle shown in Figure 2.5, (a) sub-critical mode, & (b) trans-critical mode. The figure depicts a general T-S diagram of CO_2 .

reverse Rankine cycle can be operated in either sub-critical (Figure 2.6a) or trans-critical mode (Figure 2.6b). While the former involves a two phase condensation of the working fluid (2-3) (Figure 2.6a), the latter allows isobaric cooling via a gas cooler (2-3) (Figure 2.6b) in a super-critical region. Furthermore, a throttle valve or a two phase expander can be used for the final expansion (3-4), Figure 2.6, to the evaporator pressure and temperature. A throttle valve involves a constant enthalpy expansion while an expander provides isentropic expansion.

A reverse Rankine cycle is characterised by its high Coefficient of Performance ($\text{COP} > 1$), which is defined as the ratio of the heat discharged in the condenser to the net work input. From Figure 2.6,

$$\text{COP}_{HP} = \frac{\text{Heat rejected in condenser}}{\text{Net work input}} = \frac{Q_{2-3}}{W_{1-2}}. \quad (2.6)$$

Rankine cycle - discharging

A simple ideal Rankine cycle, in a PTES system, is used to transform the heat available from the TES to electrical power output, as shown on the right in Figure 2.5. The ideal cycle consists of four major components: (i) evaporator/gas-heater (hot storage), (ii) turbine, (iii) a condenser (cold storage), and (iv) a pump. The thermodynamic processes undergoing this cycle are as shown in Figure 2.7b:

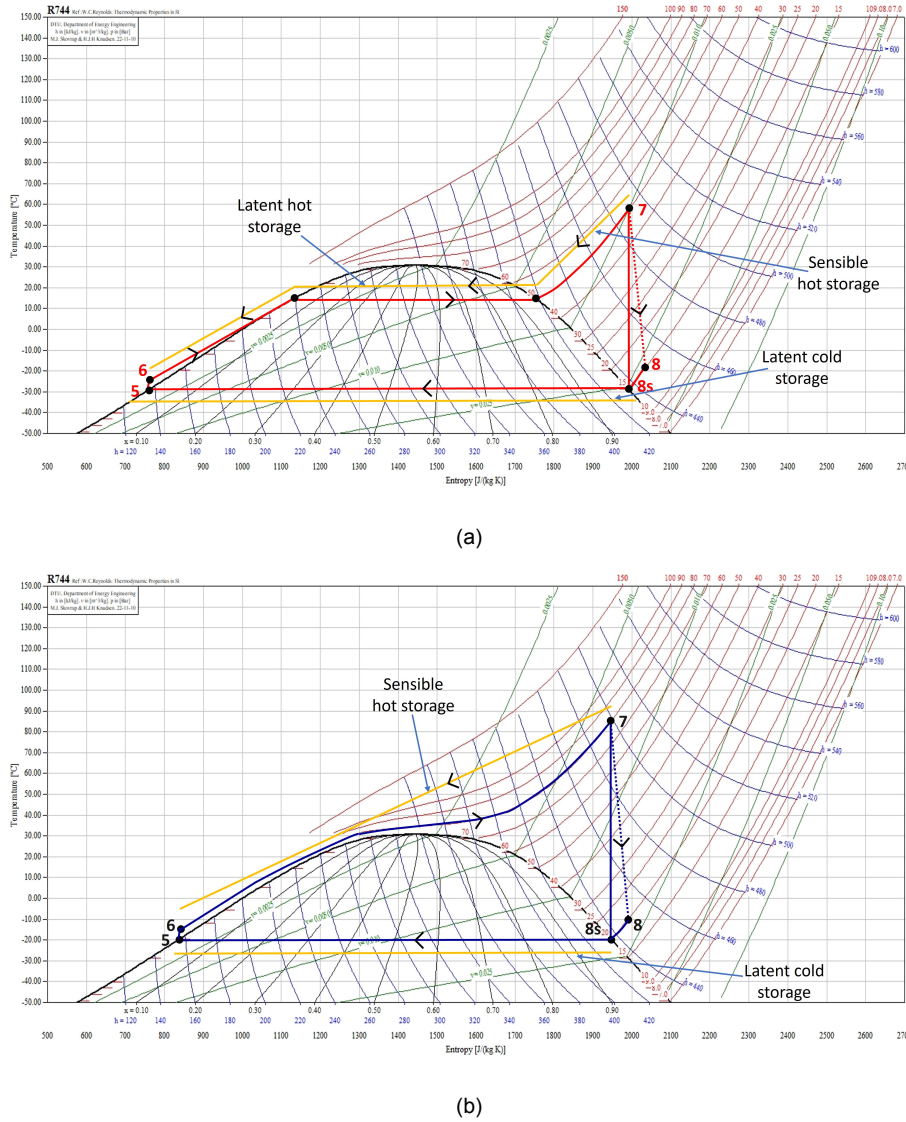


Figure 2.7: T-S plot for Rankine cycle corresponding to the discharging cycle shown in Figure 2.5, (a) sub-critical mode, & (b) trans-critical mode. The figure depicts a general T-S diagram of CO₂.

- 5-6 : Pumping
- 6-7 : Isobaric heat addition from hot storage
- 7-8s : Isentropic expansion; 7-8: Real expansion
- 8-5 : Isobaric heat rejection to cold storage

A Rankine cycle finds its application across a wider temperature range, from small scale - low temperature CHP plants to large scale - high temperature steam power plants, nuclear reactors, etc. For the PTES application, the working fluid is converted to high pressure and temperature vapor(6-7) using the heat

stored in the high temperature TES, which is then expanded via the turbine to generate shaft power (7-8). The expanded working fluid is further condensed while rejecting heat to the low temperature heat sink (8-5) or cold storage. Finally, the condensed working fluid is pumped back to its high pressure (5-6) and the cycle continues. A Rankine cycle is characterised by the cycle thermal efficiency, which is defined as the ratio of net work produced to the heat available at high temperature storage. Although a certain amount of work is needed to operate the pump, it is significantly lower than the turbine output work and can be neglected while evaluating the efficiency.

$$\eta_{RC} = \frac{W_{turbine}}{Q_H} = \frac{W_{7-8}}{Q_{6-7}}. \quad (2.7)$$

Working fluid and storage medium

For Rankine PTES applications, fluids from different chemical families (eg: organic fluids, CO₂, etc.) can be used. However, organic fluids are best suited to operate at low temperatures as required by Rankine PTES systems. Additionally, the use of organic fluids at high temperatures is limited by their low critical temperature and thermal degradation (>200-250°C) [51], which is the reason, organic fluid based Rankine systems are generally operated at sub-critical state. Yet another alternative which is quite in research since last decade is the use of inorganic fluids, eg: CO₂ for Rankine based PTES system operating in trans-critical regime [66]. Trans-critical CO₂ PTES employs low temperature heat exchange at sub-critical state with latent heat storage (eg: PCM) while sensible heat storage (eg: liquid or solid based) for heat exchange at high temperatures. While some authors have given a theoretical insight to trans-critical CO₂ based PTES system [17, 18, 75], others have provided an evidence of the feasibility of the technology from commercial point of view [47, 62].

Since a Rankine PTES system can operate in both sub-critical and trans-critical mode, a wide choice of storage mediums could be available. The storage medium could be either a latent heat storage, a sensible heat storage, or a combination of both as shown in Figure 2.7. Potential storage mediums for a Rankine PTES include: hot water, PCMs, molten salts, sand, thermal oils, etc. as high temperature storage mediums. For cold storage mediums, ice can be used.

Rankine PTES configurations

A standard sub-critical organic heat pump and organic Rankine cycle constitutes a possible configuration for pumped TES. These systems are best suited to be used at low temperatures, specifically because of the low boiling point and high molecular weight of the organic fluids/refrigeration fluids. A schematic representing such a thermal integration is shown in Figure 2.8.

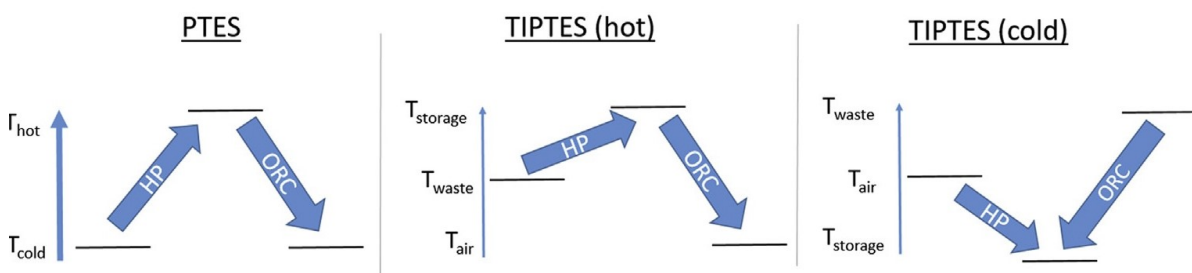


Figure 2.8: PTES (left), Thermal Integrated PTES (TIPTES) with hot storage (center) and TIPTES with cold storage (right) [30].

PTES shown towards the left in Figure 2.8, is the usual PTES cycle operating between two thermal storage's. The other two depicts waste heat integration with a hot storage configuration (center) and a cold storage configuration (right). The RTE of the standard PTES is always < 1, however a RTE > 1 can be obtained for PTES with thermal integration [30].

For the hot storage configuration in Figure 2.8, the waste heat (typically > 50°C) is used to vaporize the working fluid at a pressure higher than the ambient. A heat pump upgrades this waste heat during

the charging cycle to store in a high temperature TES. Further, a Rankine cycle is operated in the dis-charging cycle to reject the heat to the ambient while generating work. Since the RTE of a PTES is greatly affected by the performances of the individual cycle, from Equation (2.1), an increase in both the COP of heat pump and thermal efficiency of heat engine results in a higher RTE. O. Dumont et al.(2020) maps the performance of thermally integrated PTES for hot and cold storage configuration and reports a higher P2P ratio for hot storage configuration [30].

2.2.3. Performance Parameters

Round Trip Efficiency (RTE) is an important parameter to assess the performance of any PTES system. It is alternatively mentioned as Power-to-Power (P2P) ratio, which is defined as the ratio of net work produced from the system to the net work input to the system and is given in Equation (2.1).

Effect of storage temperature on the performance of PTES system

Considering a simple Carnot PTES system, as shown in Figure 2.1, which consists of a Carnot heat pump and a Carnot heat engine. Realising a thermal storage with temperature T_{TES} as a high temperature storage medium, ambient with temperature T_A as the low temperature heat sink and a finite temperature difference between the heat exchangers T_{pinch} , the RTE given in Equation (2.2) can be modified as:

$$\eta_{RTE} = \frac{T_{TES} + T_{pinch}}{(T_{TES} + T_{pinch}) - (T_A - T_{pinch})} \times \frac{(T_{TES} - T_{pinch}) - (T_A + T_{pinch})}{T_{TES} - T_{pinch}}. \quad (2.8)$$

Based on the Equation (2.8), a plot (Figure 2.9) is produced depicting the dependence of the RTE of a Carnot PTES on the TES temperature, cold sink temperature and pinch across HEX. This figure is a theoretical illustration, which neglects the efficiency losses across turbomachines and other electric components such as motor and generator.

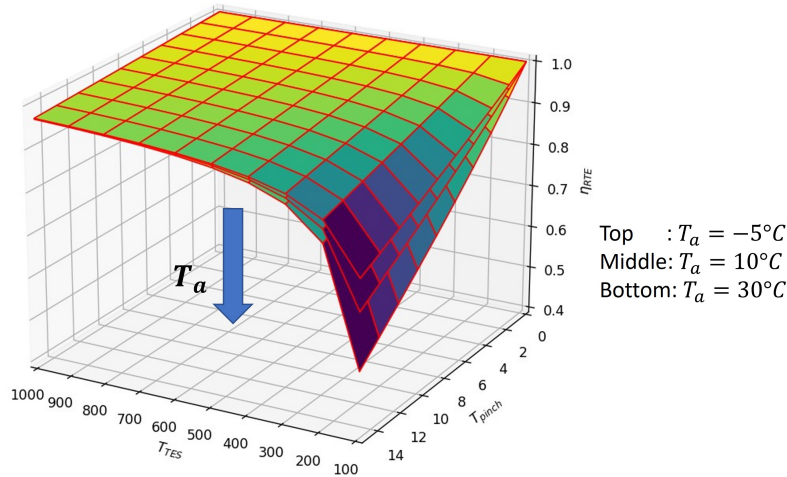


Figure 2.9: RTE of a Carnot PTES with ambient as low temperature heat sink at temperatures of $T_a = -5, 10,$ and 30°C , forming the upper, middle, and the lower efficiency surfaces.

Some of the important generalisations from Figure 2.9 are as follows:

- Irrespective of the hot storage temperature T_{TES} , and the ambient temperature T_A , the RTE is equal to 1, if the heat transfer across the HEX takes place over an infinitely small difference.
- For greater temperature differences, T_{pinch} , a sharp decline in RTE can be observed. This can be attributed to the loss of reversibility. However, this influence is lower at high storage temperatures.
- High RTE is observed for low ambient temperatures. This is caused by reduction in heat pump COP while a large increase in heat engine efficiency. This implies, PTES RTE is strongly influenced by heat engine thermal efficiency.

- Finally, increasing the hot storage temperature above 400°C doesn't impact the PTES RTE anymore for a given temperature difference (T_{pinch}) and ambient temperature (T_A).

Considering the generalisations from Carnot PTES system, similar conclusions can be made for real PTES systems as well. Some of the major factors affecting the RTE of a real PTES system are:

1. Performance of Heat Exchanger:

Ideal thermodynamic heat exchange processes consider an infinite heat exchanger surface area and thus negligible approach temperatures. However, a finite temperature difference has to be maintained between the heat exchanging mediums, since it acts as the driving potential for the heat transfer process to occur.

As evident from Figure 2.9, RTE decreases sharply with the increasing minimum temperature difference. For PTES system, in order to improve the RTE, it is important to have a nearly constant temperature difference during the course of heat exchange. This requires that the temperature profile of the working fluid and the storage medium matches precisely with each other. This is illustrated in the Figure 2.10.

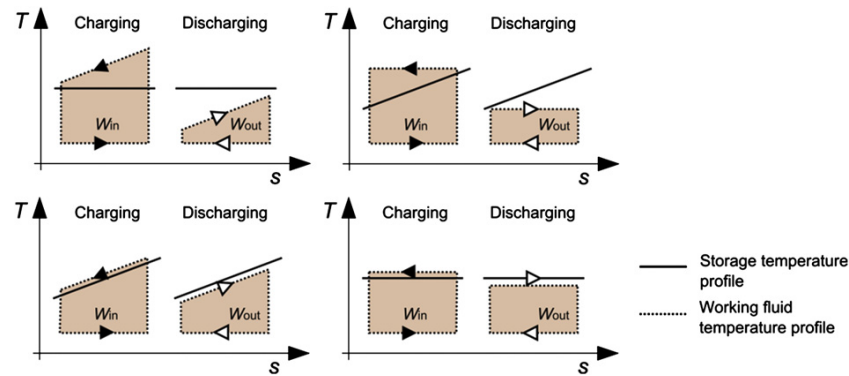


Figure 2.10: Bad and good match between the cycle and heat sources/sinks. Bad match (upper two cases) reduces the roundtrip efficiency. Good match is on the lower two frames for sensible heat storage (left) and latent heat storage (right) [62].

A bad thermal profile matching, upper two cases of Figure 2.10, results in a wide gap between the input work and the obtained work output. This is mainly because of the heat loss at the two heat exchanging interfaces: (i) working fluid to storage medium (charging), and (ii) storage medium to working fluid (dis-charging).

2. Performance of Turbomachinery:

For ideal Rankine and Brayton based cycles, the compression and expansion is considered to undergo an isentropic (reversible adiabatic) process. However, in real cycles, these processes deviate from the ideal processes. As such, a factor termed as isentropic efficiency is defined for turbomachinery.

For a compressor/pump, isentropic efficiency is the ratio of the work input for an isentropic process to the actual work input, which is < 1 . This implies, the losses in the compressor due to the irreversibility results in consumption of more power in order to attain the required outlet conditions.

Similarly, for a turbine, isentropic efficiency gives the ratio of the actual work output to the work output received in an isentropic process (ideal cycle), which is again < 1 . This implies, due to the irreversibility within turbine, a lower power output would be obtained for the same operating conditions.

The RTE of a real PTES cycle including the effects of turbomachinery efficiencies would result into:

$$\eta_{RTE,real} = COP_{HP,real} * \eta_{HE,real} \quad (2.9)$$

$$= \eta_{is,comp} \eta_{is,turb} \frac{\dot{W}_{is,turb}}{\dot{W}_{is,comp}} \quad (2.10)$$

where, $\eta_{is,comp}$ & $\eta_{is,turb}$ is the isentropic efficiency of the compressor and turbine respectively while $\dot{W}_{is,turb}$ & $\dot{W}_{is,comp}$ is the ideal/isentropic work performed/required by the turbine or compressor respectively. Therefore, a higher isentropic efficiency of turbomachines is necessary to attain high RTE.

3. Pressure losses:

Working fluid encounters frictional losses during its course of flow and across different components in a thermodynamic cycle. This frictional loss results in a pressure drop across each component and in the connecting pipes. A greater drop in pressure values can all together prevent the turbine from rotating due to low pressure in the system [70]. Ghalya Pikra et al.(2022) lists the pressure drop studies of different components done by various researchers, which show that the pressure drops reduce the system's efficiency [70].

2.3. Rankine PTES - Waste Heat Integration/CHEST

A Rankine PTES with waste heat integration represents the hot storage configuration mentioned in Figure 2.8. It is alternatively called as Compressed Heat Energy Storage (CHEST) because an input waste heat is compressed to store in high temperature TES. A simple process flow diagram depicting the principle of CHEST is shown in Figure 2.11. The corresponding T-S curve is shown in Figure 2.12.

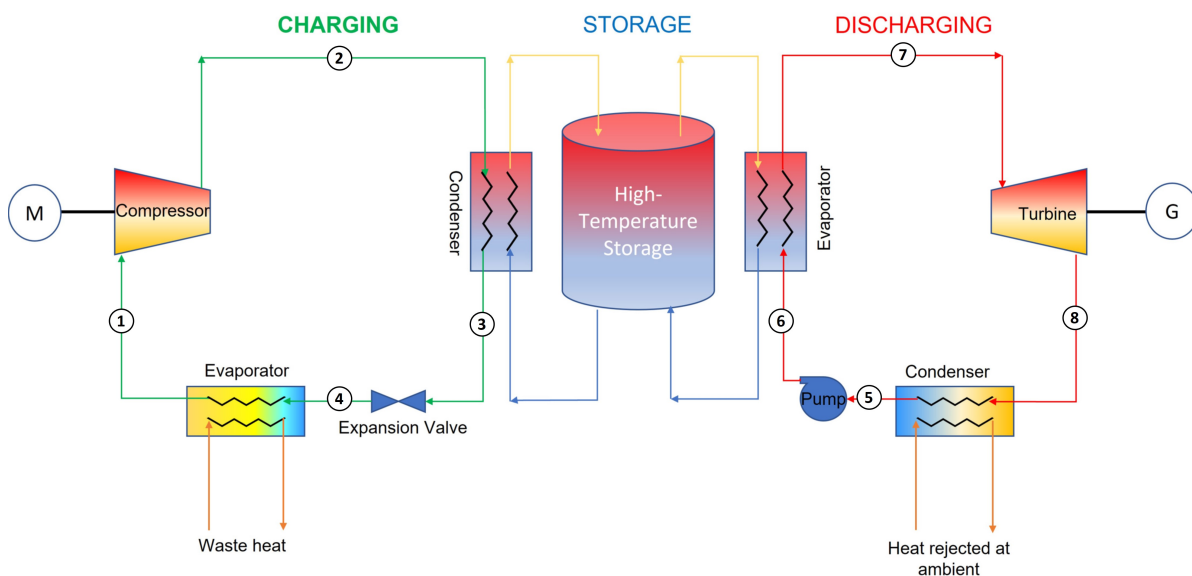


Figure 2.11: PFD of a waste heat integrated Rankine PTES system.

Unlike a standard PTES system, with TES at both the hot and cold ends of the cycle, the CHEST system consists of only hot TES. In a CHEST system, a waste heat at $\sim 50 - 100^\circ\text{C}$ is used to vaporise the working fluid in the heat pump evaporator (4-1) at a pressure greater than the ambient. Using an external electric work input, a compressor upgrades this waste heat, now carried by the working fluid, to a high temperature-high pressure conditions (1-2). Working fluid rejects this high grade heat to a high temperature TES while getting condensed/cooled (2-3). Further, the working fluid is expanded through an expansion valve to reach its original conditions (3-4), where it again absorbs the waste heat (4-1) and the charging cycle continues.

On the other hand, the heat stored in the high temperature TES is transferred to the working fluid during a discharge cycle. The working fluid is heated and evaporated using this stored heat (6-7). From high temperature and pressure conditions, the working fluid is expanded through a turbine, thus generating work (7-8). The fluid is further cooled and condensed while rejecting heat to the ambient (8-5). Finally, the liquid fluid is pumped back to high pressure conditions (5-6), where it absorbs the heat from the TES (6-7) and the discharging cycle continues.

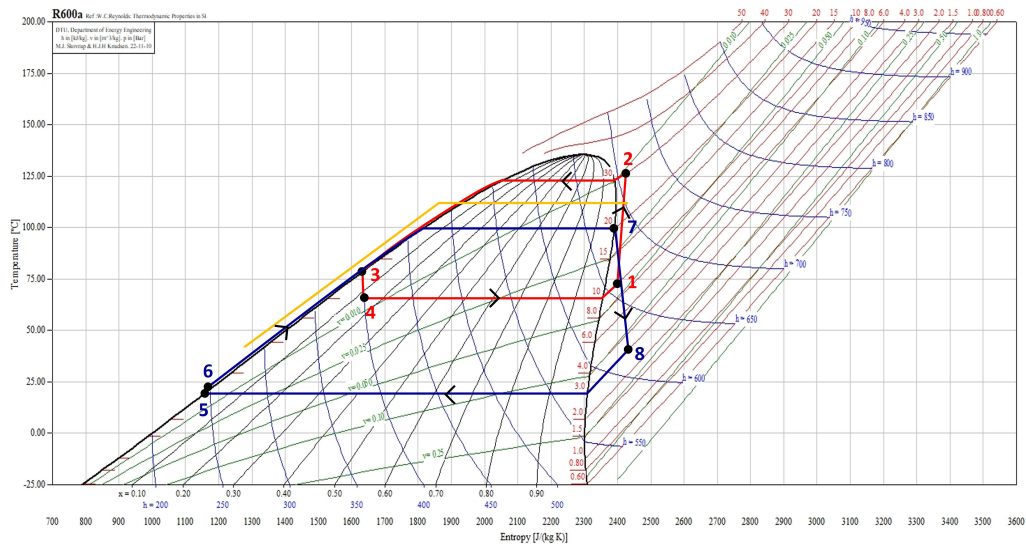


Figure 2.12: T-S plot for a typical CHEST system corresponding to the PFD shown in Figure 2.11, with heat pump cycle in red color, Rankine cycle in blue color and storage in yellow color. The figure shows a T-S plot for isobutane as a working fluid.

The key aspect of a CHEST system is the difference between the waste heat source and sink temperature while the hot storage temperature remains the same. The idea behind the CHEST system by introducing waste heat at the heat pump evaporator is to keep low temperature lifts (alternatively small pressure ratio) within the heat pump during charging while carrying out expansion at a higher pressure ratio within a heat engine during discharging cycle. A low temperature lift increases the COP of heat pump while a greater expansion ratio improves the thermal efficiency of the heat engine. A simultaneous increase in COP and thermal efficiency results in higher overall round trip efficiency, which could exceed more than 100%.

To demonstrate the effect of waste heat integration, a Carnot PTES is considered with a hot TES and the effect of waste heat temperature is shown on the performance of the system at various TES temperatures and pinch conditions in the Figure 2.13. This figure is a theoretical illustration, which neglects the efficiency losses across turbomachines and other electric efficiencies.

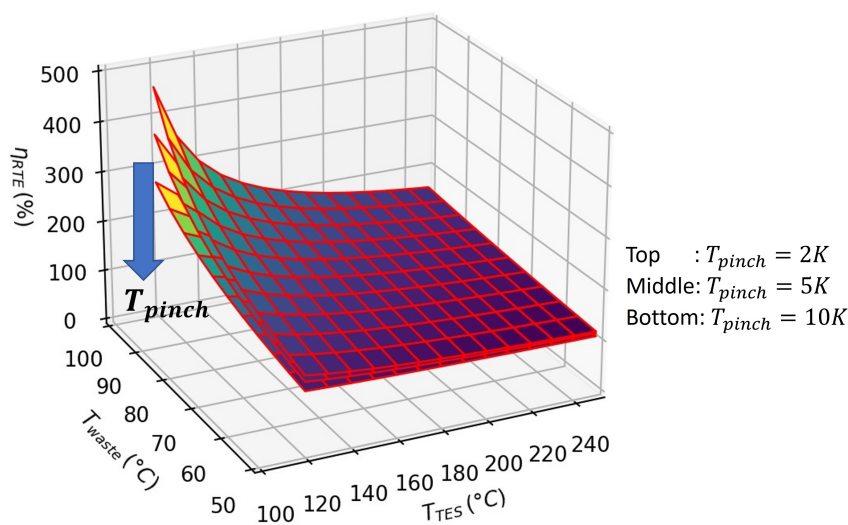


Figure 2.13: RTE of a Carnot PTES with waste heat integration at a fixed ambient temperature, $T_a = 20^\circ\text{C}$, for different pinch of $T_{pinch} = 2, 5, \& 10\text{K}$, forming the upper, middle and lower efficiency surfaces.

A CHEST system is highly dependent on the availability of the waste heat. Moreover, it is important to identify whether the heat availability (at source) and use (at sink) patterns, match both in terms of quantity and timing. In other words, there should be a continuous supply of waste heat in sufficient quantities to operate the PTES system. Generally, a waste heat is categorised into low grade ($T_{waste} < 100^{\circ}C$), medium grade ($100 < T_{waste} < 300^{\circ}C$), and high grade ($T_{waste} > 300^{\circ}C$) heat [29]. Further, a PTES system is suitable for integrating low grade waste heat, so that the low grade heat can be converted to high grade heat and stored and used for further applications. Otherwise, for an available high grade waste heat, a Rankine cycle can directly be operated without the need of using a heat pump.

The potential sources of low grade waste heat that can be integrated with Rankine PTES are listed in Table 2.1. Other than the ones mentioned in the table below, there are many industrial low grade waste heat sources available below $100^{\circ}C$ such as pasteurization, flue gases, engines coolant, etc. [29, 52].

Heat Source	Temperature ($^{\circ}C$)	Reference
Data Centers	25-40	[39, 86]
Electrolyzers	75-80	[50, 55]
Industrial air dryers	70-100	[73]

Table 2.1: Potential sources of low grade waste heat.

2.4. Literature Cases

Following the different configurations of the PTES system, as shown in Figure 2.8, some of the PTES design concepts given by certain research institutes and companies are discussed as a literature case and compared in the following sections.

2.4.1. Literature case-I: DLR PTES

This literature case is concerned with the application of ORC system for PTES. German Aerospace Center (DLR) has given an ORC based PTES concept, as shown in Figure 2.14, which facilitates storing heat at hot side in both latent (LH-TES) and sensible (SH-TES) heat storage medium.

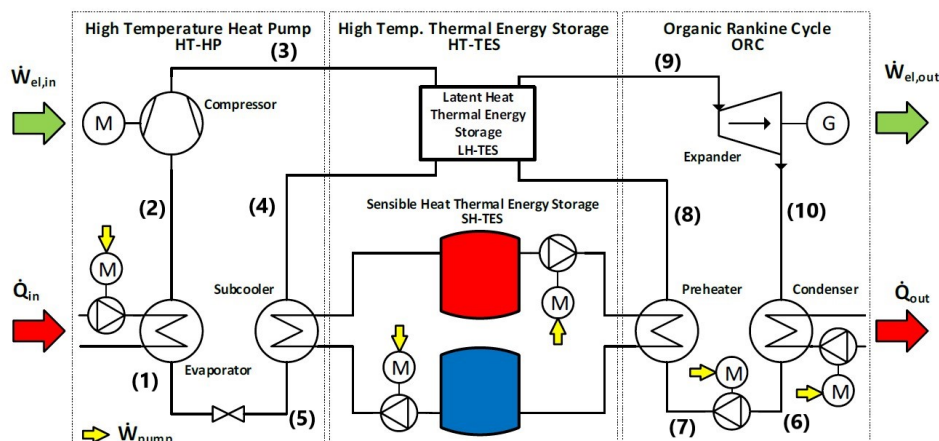


Figure 2.14: Process diagram of the subcritical PTES with low temperature heat integration [49].

This literature case is based on the concept of thermal integration in PTES, hot storage configuration in Figure 2.8, which involves pumping waste heat to a high temperature storage medium. This concept allows the PTES system to operate at two different heat source and heat sink temperature levels of the system. For the HP cycle, the source temperature (waste heat) is kept sufficiently high compared

to the power cycle sink temperature (ambient). Doing so, the temperature lift in HP cycle reduces, thus improving the COP, while a greater temperature range is available for the fluid to expand in the discharge cycle, thereby augmenting the thermal efficiency of the power cycle. Collectively, an increase in both COP as well as thermal efficiency could result in P2P ratio > 1, Figure 2.15.

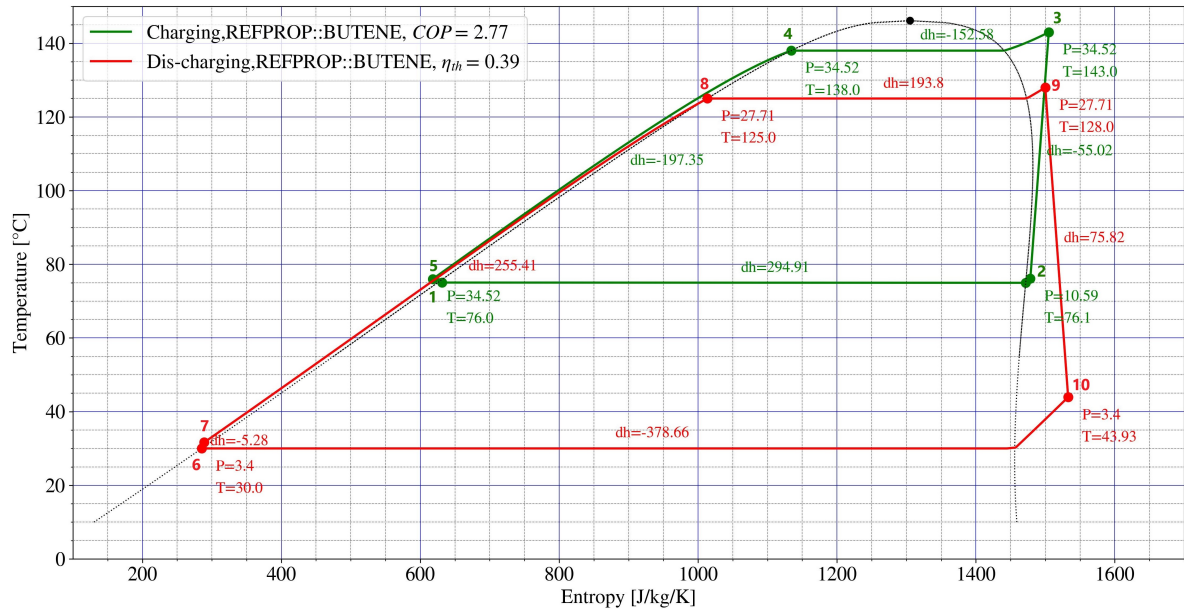


Figure 2.15: T-S plot for subcritical ORC based PTES with low temperature heat integration while the state points correspond to the PFD shown in Figure 2.14.

The T-S plot, shown in Figure 2.15, doesn't account for pressure losses across the HEX and is based on the optimised parameters as given by DLR [49]. Butene is chosen as the working fluid.

In the charging cycle, waste heat is used to evaporate the working fluid (1-2), which is compressed from (2-3) to high temperature & pressure. The latent heat of condensation (3-4) is stored in the PCM (eutectic mixture of KNO_3 & LiNO_3) with a melting temp of 133°C . The sensible heat available (4-5) is stored in a pressurised water thermocline and finally throttled to the original state. During the discharging cycle, the working fluid is preheated by the heat stored in the water thermocline (7-8) and is further evaporated followed by super-heating using the latent heat stored in the PCM (8-9). The hot and pressurised fluid is allowed to expand (9-10) to generate power followed by rejecting heat (10-7) to the heat sink (ambient).

In order to ensure the uniform charging and discharging of hot energy storage medium, the ratio of latent and sensible heat should be constant during charging and discharging cycles. Otherwise, this would result in a part of the high temperature TES discharged while other still left with some energy. This can be formulated as given in Equation (2.11),

$$\left| \frac{Q_{latent}}{Q_{sensible}} \right|_{charging} = \left| \frac{Q_{latent}}{Q_{sensible}} \right|_{dis-charging} \quad (2.11)$$

The model presented in Figure 2.15 gives a RTE of 1.07 for a source temperature (T_{source}) of 80°C and a sink temperature (T_{sink}) of 20°C . Henning Jockenhöfer et al. (2018) showed the dependence of the RTE on the T_{source} and T_{sink} for different approach temperatures across the HEX. A maximum RTE of 1.25 was estimated for $T_{source} = 100^\circ\text{C}$, $T_{sink} = 15^\circ\text{C}$ and $\Delta T = 5\text{K}$ [49].

2.4.2. Literature case-II: MAN/ABB-PTES

This literature case is based on the standard Rankine PTES configuration as earlier shown in Figure 2.8. MAN Energy Solutions and ABB Corporate Research collaborated to create a Rankine PTES technology that could be used as a standalone system or integrated into other facilities as shown in Figure 2.16. This PTES system is a fairly low temperature system with a reversible trans-critical CO₂ Rankine cycle [62]. A detailed description of the system is provided in their documented patent [61].

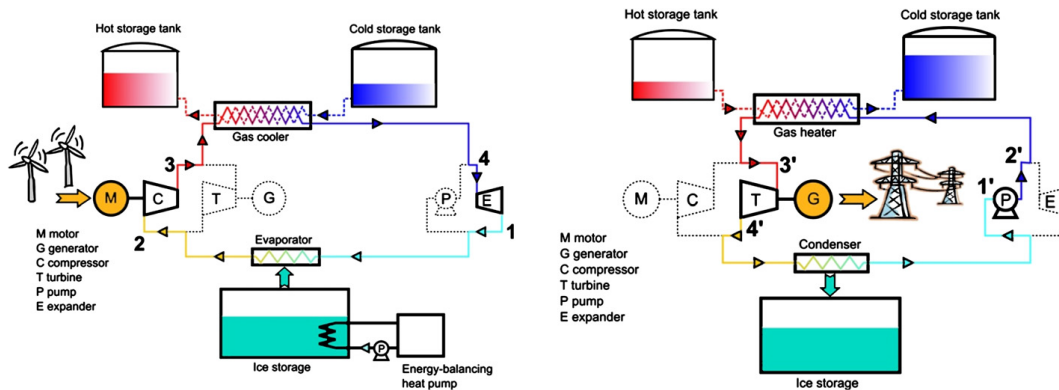


Figure 2.16: Sample plant layout during charging (left) and discharging (right) cycle [62].

A schematic of the base case is shown in Figure 2.17, which involves a variation from the reference layout, Figure 2.16, in terms of heat integration and method of removing heat due to entropy generation.

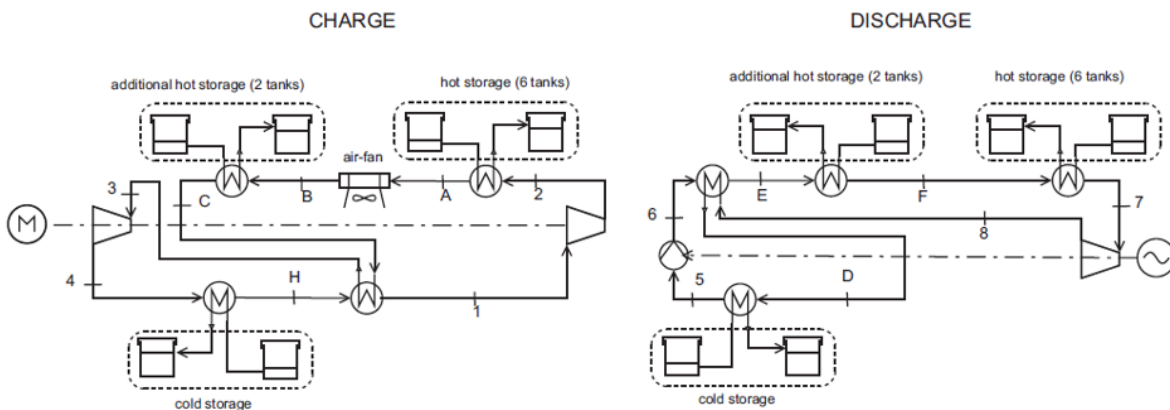


Figure 2.17: Process flow diagram of the TEES plant, max roundtrip solution with superheating before the HP compressor inlet [65].

As can be seen in Figure 2.17, internal heat recovery has been employed in both the charging and discharging cycles in the form of super-heating and pre-heating respectively. Super-heating before compression mainly helps in two ways: (i) for same compressor power it increases the outlet temperature, and (ii) for same compressor outlet conditions it reduces the specific power input. While (i) allows to reach higher storage temperatures thus providing the HE cycle a boost in its efficiency, (ii) increases the COP of the HP cycle.

For this kind of PTES system, the thermal balancing of the system is necessary. Due to the irreversibilities in the thermodynamic processes, the excess heat accumulated within the system ultimately gets discharged at the cold storage side. This implies that the energy released by vapor condensation during the HE cycle exceeds the energy used for evaporation during the HP cycle. This excess heat needs to be rejected to the ambient to attain steady-state conditions. For this, an air cooler has been employed, which rejects heat to the ambient and is relatively cheap and simple as compared to the additional ammonia cycle incorporated in the reference case [64].

Based on the optimised parameters included in Appendix B, a T-S plot is produced, Figure 2.18, with the HEX approach temperature of 5K. The marked state points corresponds with the order maintained in Figure 2.16. Referring to Figure 2.18, for HP cycle in green, state 1-2 indicates polytropic compression followed by state 2-C: isobaric gas cooling, state C-3: internal heat recuperator, state 3-4: polytropic expansion, 4-H: evaporation and finally H-1: super-heating. Similarly for the HE cycle in red, state 5-6: polytropic pumping, state 6-E: preheating, state E-7: super-critical heating, state 7-8: polytropic expansion, 8-D: internal heat recuperator and finally D-5: condensation.

A sample calculation is provided in the Appendix B, in order to estimate the required air-cooling. A cold utility of ~ 610 kW has to be removed which is around 38% of the input electric power. In terms of specific enthalpy, a cooling of 49.5 kJ/kg has to be provided in the charging cycle.

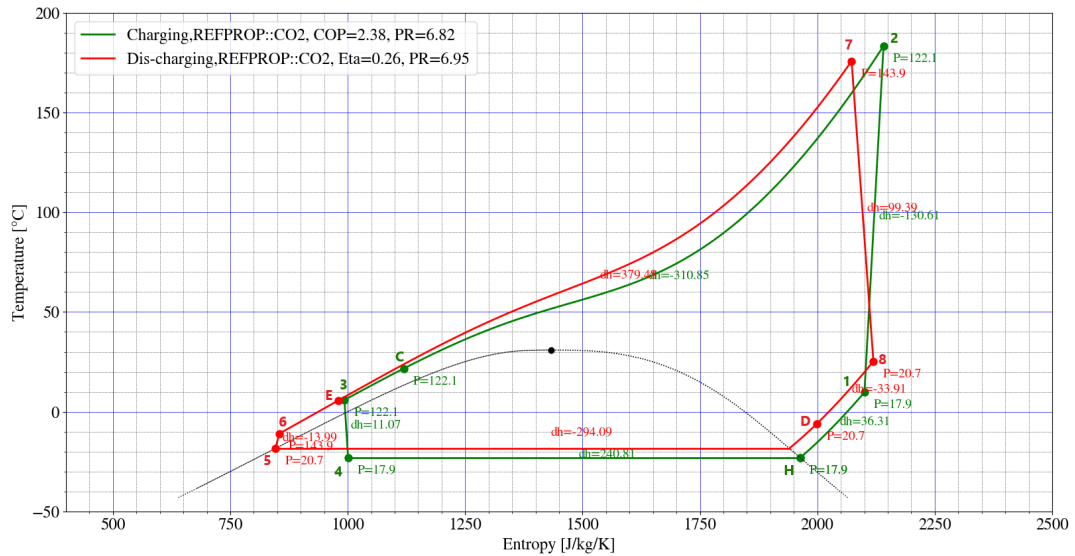


Figure 2.18: ABB Base case Configuration: T-S plot with air-cooling corresponding to PFD of charging cycle, Figure 2.17 (left).

An important point to note here is that the excess heat can be removed from either the charging or discharging cycle or partly from both. In this configuration, as shown in Figure 2.17 (left), air-cooler is installed in the gas cooling phase of the charging cycle (2-C), Figure 2.18. The high density heat is first stored in the first set of hot storage tanks, Figure 2.16, followed by discharging excess heat to the ambient and finally the remaining heat is again stored in another set of storage tanks. Based on the calculations made the RTE of the cycle comes out to be 62.3%, which precisely matches with the RTE indicated in [65]. This value is 2.3% point more than the reference case.

Observations and conclusions from literature case-I&II

The Table 2.2 lists out the key operating conditions and conclusions of the thermodynamic design of PTES incorporated in the literature case-I&II.

Literature Case-PTES	Working Fluid	High Temp Storage	Operating Temperature (°C)	Operating pressure (MPa)	Research conclusions	Research gap
DLR	Butene	KNO ₃ +LiNO ₃ water	charging: 80-133 dis-charging: 20-133	charging: 1.0-3.5 discharging: 0.34-2.8	<ol style="list-style-type: none"> 1. integration of low temperature heat- possibility of RTE>1 2. PTES can also act as a energy management system (smart district heating application) 3. heat exchanger is main contributor to exergy loss 	<ol style="list-style-type: none"> 1. no optimisation provided for heat exchangers and turbomachinery 2. development of a PCM storage
ABB/MAN	trans-critical CO ₂	pressurised water	0-120	charging: 1.8-12.2 discharging: 2.0-14.4	<ol style="list-style-type: none"> 1. superheating before compression ($\Delta T_{sup} \sim 30K$) yielded the highest efficiency 64% 2. pressure levels of charging & discharging cycle - key design parameter 3. Turbomachinery optimum design - an indispensable factor for high performance of cycle 	<ol style="list-style-type: none"> 1. mentions waste heat driven cycle but no detailed numerical analysis has been carried out.

Table 2.2: Quantitative & Qualitative comparison of potential PTES technologies.

Based on the key aspects of both the literature cases, PTES with heat integration provides a more promising solution, however it is highly dependent on the availability of waste heat. On contrary to the literature case-II, an interesting fact is that, there is no need of placing an extra heat rejection unit in literature case-I. This is because the heat pump source temperature is much higher than the heat engine sink temperature and the sensible energy deficit created due to this can be compensated by partly exchanging heat with latent storage. Moreover, there are less number of components in literature case-I, which mitigates the potential exergy losses across each component. Further, this results in lower overall costs of the plant.

In this thesis, the work is mainly build up on the concept of the literature case-I, i.e. to integrate waste heat with the PTES system. The following sections describe the selection criteria of the working fluid and storage medium for the waste heat integrated PTES system.

2.5. Working Fluid & Storage Medium for CHEST system

The working fluid is an essential component of any thermodynamic cycle, and the thermal storage medium is foundation of the PTES technology. The working fluid and the storing media are inseparable in a PTES system. The working fluid is the primary fluid that undergoes multiple thermodynamic processes in a cycle and is mostly responsible for the process's output. Nonetheless, the ability of the storage media to absorb energy while retaining it for an extended period of time and releasing it on demand are some of the critical elements in determining system performance. Finally, an optimal temperature difference (pinch point) between the working fluid and the storage medium is necessary to drive the charging and discharging cycles.

2.5.1. Selection criteria of working fluids

There are many working fluids, some of which are now in commercial use while others are being researched. Each fluid has its own set of characteristic thermo-physical properties which makes them suitable for a specific thermodynamic cycle. These properties determine the cycle's operating conditions and performance while also offering an estimate of its environmental and economic sustainability.

Table 2.3 lists a number of potential working fluids for Rankine PTES system. The table mainly lists the organic working fluids which are best suitable for low/medium grade waste heat integration [80]. CO₂ and water have been included as a reference fluid. The intensive properties of the working fluid have been evaluated at $T = 30^\circ\text{C}$. This table tends to be very handy in getting an idea of how effectively a working fluid can operate in a typical sub-critical or trans-critical Rankine cycle PTES system. The molecular weight gives an idea about the density of the fluid; the critical point suggests the possible operating regime; ω , k_c , and m are Lee-Kesler's parameters which controls the shape of the T-S curve [74]; vapor specific heat could be used to estimate the turbine/compressor power while latent heat provides an idea of heat absorbed or heat discharged; GWP and ODP are necessary indicators of the impact of working fluid on environment and ozone layer; and finally the last three columns provide the NFPA safety designation for the refrigerants (0-safe; 4-dangerous).

Working Fluids	Name	Type	Mol. Wt. (g/mol)	T_{cr} (°C)	P_{cr} (bar)	ω	k_c	m	Vapor C_p kJ/kg-K	Latent Heat (kJ/kg)	GWP	ODP	Flammability (Red)	Toxicity (Blue)	Instability (Yellow)
R123	Freon 123	Isentropic	153	183.7	36.6	0.2819	1.0699	-0.0465	0.7	169	77	0.02	0	2	1
R236ea	HexaFluoro-Propane	dry	152	139.3	35	0.3688	1.0572	-0.035	0.9	153	1370	0	0	1	0
R245ca	PentaFluoro-Propane	dry	134	174.4	39.3	0.3546	1.0565	-0.0477	0.92	201	693	0	1	3	0
R245fa	PentaFluoro-Propane	isentropic	134	154	36.5	0.3776	1.0608	-0.0488	0.92	202	1030	0	1	2	0
R365mfc	PentaFluoro-Butane	dry	148	187	32.6	0.3774	1.0466	-0.0313	1	193	794	0	0	1	0
R-600	Butane	Isentropic	58	152	38	0.2008	1.0677	-0.0646	1.8	356	4	0	4	1	0
R-601	Pentane	dry	72	196.5	33.7	0.251	1.0503	-0.0499	1.7	363	0.1	0	4	1	0
R-601a	Isopentane	dry	72	187	33.8	0.2274	1.0509	-0.0696	1.73	342	0.1	0	4	1	0
	Butene	Isentropic	56	146	40	0.1919	1.0802	-0.0827	1.7	355	4	0	4	1	0
R1233zd(E)	HydroChloro-FluoroOlefin	Isentropic	130.5	165.6	35.7	0.3024			0.84	186	5	3E-4	0	2	0
R141b	Freon 141b	Isentropic	117	204.4	42.1	0.2195	1.0786	-0.0561	0.8	224	700	0.11	1	2	0
CO ₂	Carbon di-oxide	wet	44	31	73.8	0.2239	1.2857	-0.1092	5	152	1	0	0	2	0
H ₂ O	Water	wet	18	374	220.6	0.3443	1.2912	-0.0423	1.9	2430	0	0	0	0	0

Table 2.3: Thermo-Physical properties of selected working fluids evaluated at $T = 30^\circ\text{C}$.

The importance of each of the measured properties and quantities, in Table 2.3, in selecting a suitable working fluid is discussed in the following sections.

Nature of working fluids

Working fluids can be classified as: (i) Wet, (ii) Dry, and (iii) Isentropic fluids based on the slope of the vapor saturation curve (dT/ds) in the T-S diagram. The extent of the dryness of a fluid is given by the inverse of the vapor saturation curve slope i.e. $\xi = ds/dT$. Referring to Figure 2.19, a $\xi <$

0 characterises a wet fluid (eg: R21) while $\xi > 0$ is for a dry fluid (eg: isopentane) and $\xi = 0$ for an isentropic fluid (eg: R142b). The term 'wet' refers to the fluid impinging on the turbine blades when it expands from saturated vapor conditions into a two-phase zone during isentropic expansion. Whereas, a dry and isentropic fluid always expands in a gaseous phase with isentropic fluid having an almost vertical vapor saturation curve.

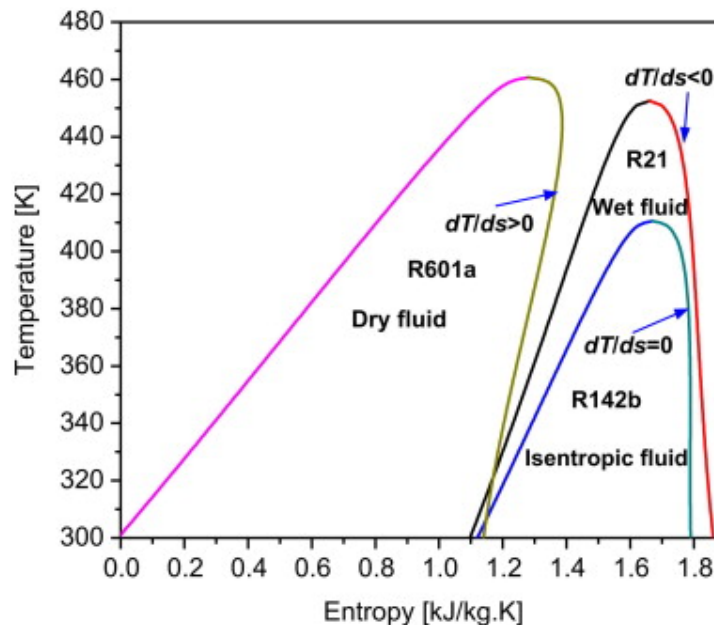


Figure 2.19: Three types of working fluids: dry ($\xi > 0$), isentropic ($\xi = 0$), and wet ($\xi < 0$) [84].

This leads to opting dry and isentropic fluids for sub-critical cycles, mainly the ORC. On top of that, even for trans-critical cycles, dry fluids are reported to perform better than wet fluids even if the expansion involves a liquid-vapor co-existence region [20]. Nevertheless, isentropic fluids provide an edge over dry fluids since the turbine outlet conditions are more closer to vapor saturation line in the former case. This helps in reducing the condenser load as compared to the too dry condition, which demands an extra heat recovery system.

While this classification is an important tool for selecting fluids for sub-critical cycles, it is of low importance for super-critical cycles as the fluid always tends to be above the critical point. The optimum selection of the working fluid considering the nature of shape of the T-S vapor saturation requires a more generic physics-based model. Alejandro Rivera-Alvarez et al.(2020) presents such a model which accurately determines the shape of the T-S vapor saturation curve for any fluid based on three input variables: acentric factor (ω), k_c , and m [74], which can be defined here as follows,

- **Acentric Factor (ω)** : It is a measure to quantify how far a substance's thermodynamic characteristics deviate from what the two-parameter PCS predicts. It correlates the deviation in the thermodynamic properties of the fluids containing non-spherical molecules with the spherical counterparts.
- **k_c** : It gives the ideal-gas ratio of specific heats at the critical temperature.
- **m** : It is the exponent of the ideal-gas ratio of specific heats vs temperature power relationship as per the following relationship: $k = k_c T_r^m$ [74].

The further details of the model have been included in the Appendix A. A representative plot showing the effect of acentric factor (ω), k_c and m on the T-S vapor saturation curve is shown in Figure 2.20.

The acentric factor (ω) primarily controls the width of the saturation dome as evident from Figure 2.20a. For a constant value of k_c and m , increasing the ω value widens the dome and vice-versa. The value of ω varies from -0.4 to 0.7 for most of the fluids [74]. The k_c parameter decides the skewness of

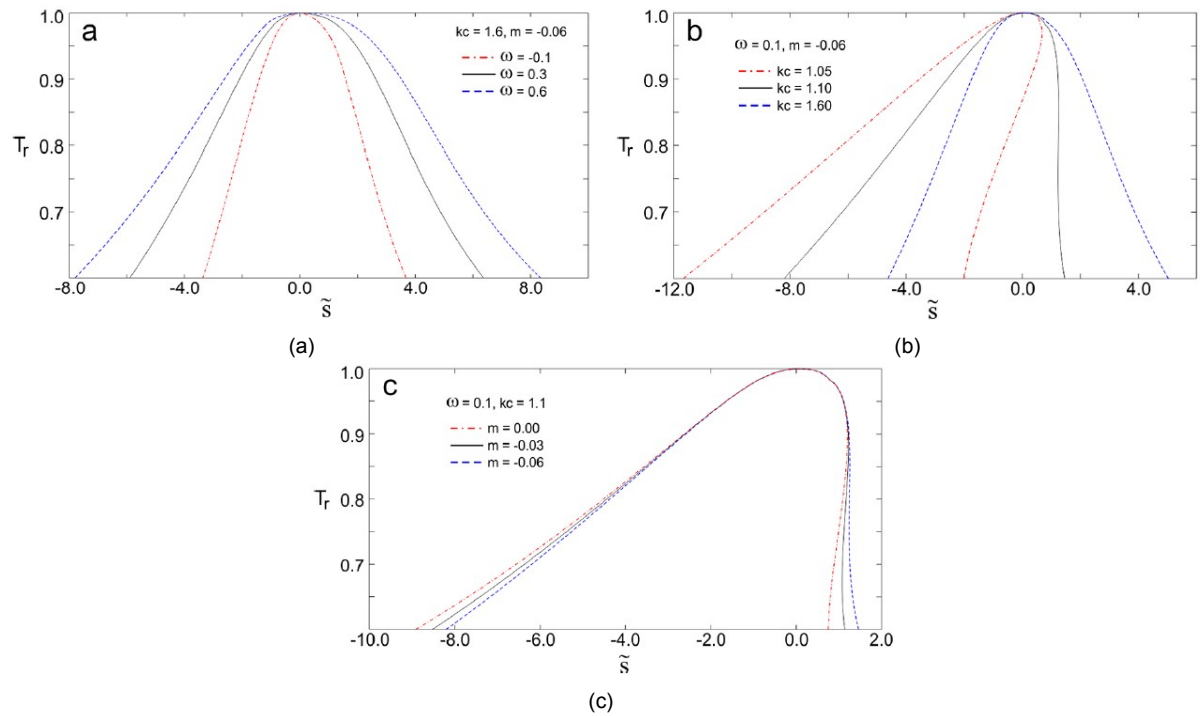


Figure 2.20: Saturation dome on a $T_r - \tilde{s}$ diagram, (a) Effect of ω , (b) Effect of k_c , and (c) Effect of m [74].

the saturation dome, which is associated with the wetness or dryness of the fluid, as shown in Figure 2.20b. For a constant ω and m , a larger value of k_c reflects a symmetrical distribution of the dome, both on liquid and vapor saturation side, while a lower k_c produces a left-skewed shape. The k_c value has a typical range between 1 and 5/3 [74]. Correspondingly, for constant ω and k_c values, m shifts the liquid and vapor saturation lines in the same direction. A typical range of m is from -0.1 to 0 [74]. Values close to zero displaces the curve towards left while shifting towards right as m moves farther away from zero.

Physical properties

H. Chen et al. (2010) states that the working fluids with high density, low liquid specific heat and high latent heat contribute to a high power output [20]. However, for a Rankine PTES cycle a high liquid specific heat is required in order to transfer maximum heat across storage through sensible heat transfer during charging and discharging cycles. A highly dense fluid ensures cutting down the size of the cycle components i.e HEX and turbomachinery. This is because a larger mass can be accommodated within a smaller volume, improving the component's compactness. High latent heat facilitates enhanced heat absorption from low temperature sources during a charging cycle.

Further, the critical point plays an important role in selecting a suitable working fluid. A critical point of a fluid is fixed/defined by a critical temperature and critical pressure. For a waste heat integrated Rankine PTES system, a critical temperature below 130 – 140°C is undesirable. This is because a low critical temperature will bring the evaporation temperature of the heat pump near to the critical point. As a result, this would lower the latent heat of evaporation, which would further require high mass flow of the working fluid and bigger equipment's. Similarly, a higher critical temperature and pressure would entail higher temperature lifts and pressure ratio for trans-critical configuration, which has a negative effect on the heat pump performance.

Thermal & Chemical stability

Many working fluids when subjected to higher operating temperatures, lose their chemical integrity and tends to decompose [69]. This leads to power loss or, even worse, deterioration of system components, i.e. HEXs and turbomachinery. The thermal stability of a working fluid largely dictates its operational

applications (eg: an organic fluid can not be used in a Brayton cycle). Moreover, the working fluid must also be non-corrosive and suitable with system component materials and lubricating oil.

Safety & Environmental Aspects, Availability & Cost

From safety point of view, the working fluids must be inflammable while having high auto-ignition temperatures. They should be non-toxic and non-explosive in nature. An ideal working fluid should offer a value of Ozone Depletion Potential (ODP) < 0.1 and low values of Global Warming Potential (GWP = 1 for CO_2). Finally, a trade off can be set between the availability, costs, and thermo-physical properties for the desired performance output.

2.5.2. Working fluid comparison

From Table 2.3, all the fluids listed can be further categorised into safe and unsafe fluids based on their potential to harm the surrounding and environment. All severe toxic fluids (Toxicity ≥ 3), unstable fluids, fluids with high ODP (> 0.1) and GWP (> 10) are eliminated from further selection. Further, all wet and dry fluids are also excluded from further analysis, since isentropic fluids are best suitable to perform in a Rankine PTES system.

The working fluids left after scrutinizing the Table 2.3 are: Butane (R-600), 1-Butene, and HydroChloroFluoroOlefin (R1233zD). All these fluids share a similar critical point, which lies in the acceptable limit of the Rankine PTES ($\sim 130 - 140^\circ\text{C} < T_{cr} < 200^\circ\text{C}$) while having a lower critical pressure. As mentioned earlier, molecular weight plays an important role in fluid selection. A higher molecular weight implies a high density of fluid, which is essential in enhancing the compactness of the cycle components. In addition to that, a high latent heat of evaporation of the working fluid is also necessary. A high latent heat ensures utilization of the waste heat to its maximum potential. The three fluids sorted above have been compared based on their molecular weight and latent heat of vaporization, as shown in Figure 2.21.

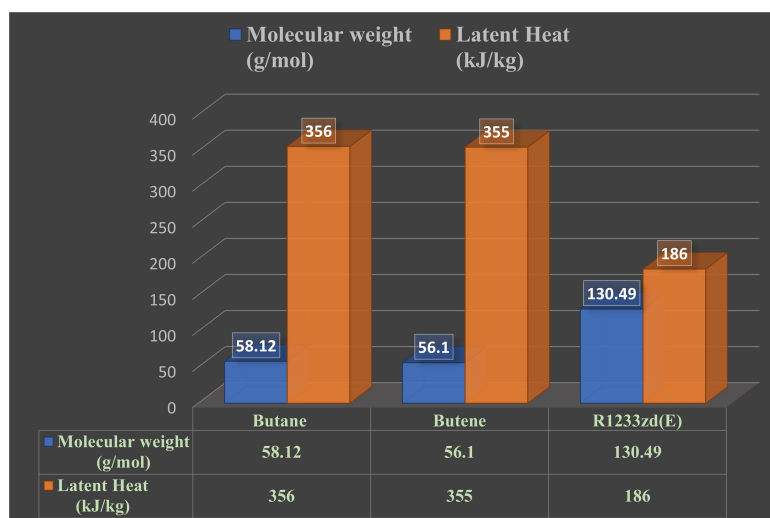


Figure 2.21: Comparison of Butane, 1-Butene, & R1233zD based on (a) Molecular weight, and (b) Latent heat of vaporization.

From Figure 2.21, while R1233zD outperforms the other two fluids in terms of molecular weight, it possess 50% lower latent heat compared to Butane and 1-Butene. This implies R1233zD is roughly denser two times than Butane and Butene, however for a given heat load, R1233zD will require twice the mass flow as compared to other fluids.

From Table 2.3, it can be observed that Butane and Butene are highly flammable, whereas, R1233zD is inflammable in nature. However, R1233zD has shown to pose material compatibility issues. Sebastian Eyerer et al. (2019) conducted a similar experimental study to check the feasibility of modern ORC working fluids (eg: R1233zd(E)) to replace common refrigerants (eg: HFC's) [34]. Although R1233zd(E) came out to be an efficient refrigerant, it posed serious material compatibility issues. The investigation

concluded the use of olefins as a replacement to HFC's, however, demanded individual material compatibility investigations when using R1233zd(E) [34].

In comparison to the working fluids mentioned above, CO₂ also exhibits excellent thermo-physical properties along with absolutely zero ODP and a lower GWP. But a lower critical point of CO₂, as evident from Table 2.3, doesn't allow for medium grade heat integration. Use of dopants with CO₂ have resulted in raising the critical point of the CO₂ mixture [25, 26, 27, 28]. This could be a potential solution for using CO₂ as a working fluid for the CHEST system, which can provide an added advantage of better connection between the sensible heat storage and the working fluid. The effect of adding a dopant in CO₂ and available options have been discussed in Appendix C.

Further, a suitable working fluid will be selected in Chapter 3 considering the requirements of the case to be analysed.

2.5.3. Thermal energy storage medium

Depending upon the mechanism of the heat transferred into or from the storage medium, Thermal Energy Storage (TES) can be divided into: (i) Sensible TES, (ii) Latent TES, and (iii) Thermo-chemical energy storage. Sensible heat storage is characterised by a temperature glide upon absorbing or rejecting heat while the latent heat storage incorporates a phase change of the storage medium. Thermo-chemical energy storage, in contrary, exploits the chemical reaction mechanisms to store and release heat.

For a PTES system, it is preferred that the thermal profiles of working fluid and the storage medium matches to a great extent. Figure 2.10 highlights the possible good and bad thermal matches. As can be inferred, a bad profile match could lead to high exergy loss. If the working fluid has a temperature glide during the heat exchange with the storage medium, it is advisable to choose a sensible heat storage medium. Whereas a latent heat storage should be used in a zero temperature glide zone. However, the choice between sensible and latent heat storage is mainly dependent on the type of application. Other factors are: cost and availability of storage medium, storage conditions (eg: pressure), thermal and chemical stability, density, etc.

Table 2.4 lists the common high temperature storage mediums used in various thermal energy storage applications.

Possible storage mediums	Nature of heat storage	Operating Temperature (°C)	Volumetric heat capacity (MJ/m ³ -K)	Phase Enthalpy (kJ/kg)	Thermal Conductivity (W/m-K)
pressurised hot water	sensible	100-250	4.2	-	0.62-0.68
sand [71]	sensible	upto 1000	2.1-2.9	-	1.7-5
rock packed bed [32]	sensible	200-1400	~2.2-2.5	-	~1
molten salts [9]	sensible	300-600	1.8-6.2	-	0.45-1.25
thermal oils [59, 35]	sensible	upto 250	1.6-2.3	-	0.14-0.16
MGA [88, 77]	sensible+ latent	600-1400	0.3-1.2 MJ/L	200-1900	150-275
eutectic mixture of Nitrate salts [21]	latent	100-220	2-4	0.080-0.265	< 0.7

Table 2.4: Thermo-physical properties of common storage mediums.

Moreover use of sensible storage instead of latent storage is preferred due to complex heat transfer mechanisms and pressurised heat exchanging devices for the latter. In case of a solid sensible TES, the working fluid is in direct contact with the storage medium. This involves a disadvantage of high pressure drops. Moreover, the storage medium needs to be operated at pressure of the working fluid. Taking the storage conditions into account, from Table 2.4, the most common options available are:

pressurised hot water, and thermal oils. Of these choices, water exhibits excellent thermo-physical properties. But using water as a storage medium at such high temperatures ($\sim 200^\circ\text{C}$) incurs heavily pressurised (25-40 bar) storage tanks, which would not be a feasible solution.

Thermal oils are potentially a very good alternative for hot storage medium at storage temperatures of around 200°C . Oils can be heated and stored at atmospheric pressure, requiring cheap storage costs, which makes it a worthy choice. Performance of oils as a thermal energy storage medium have already been investigated for specific applications, for example: solar cookers [59]. The investigation suggests use of edible oils (eg: sunflower oil) as a heat storage medium instead of commercial heat transfer fluids (eg: Shell Thermia C, etc.).

A number of edible oils are readily available in the market. It is important to compare them on the basis of certain crucial thermo-physical properties such as: specific heat capacity, viscosity, and density. These properties ultimately dictate the heat transfer characteristics and also give an estimate of the storage size. O.O. Fasina et al. (2008) lists the specific heat capacity and viscosity dependency on temperature [35]. The data obtained from the work of O.O. Fasina et al. (2008) is used to plot the dependency of specific heat capacity and viscosity on temperature for selected edible oils, as shown in Figure 2.22. The curve for Duratherm-HF is based on the data obtained from the catalogue of Duratherm's heat transfer fluids [1] and is included in the plots as a reference. Also, the viscosity of water has been included as a reference.

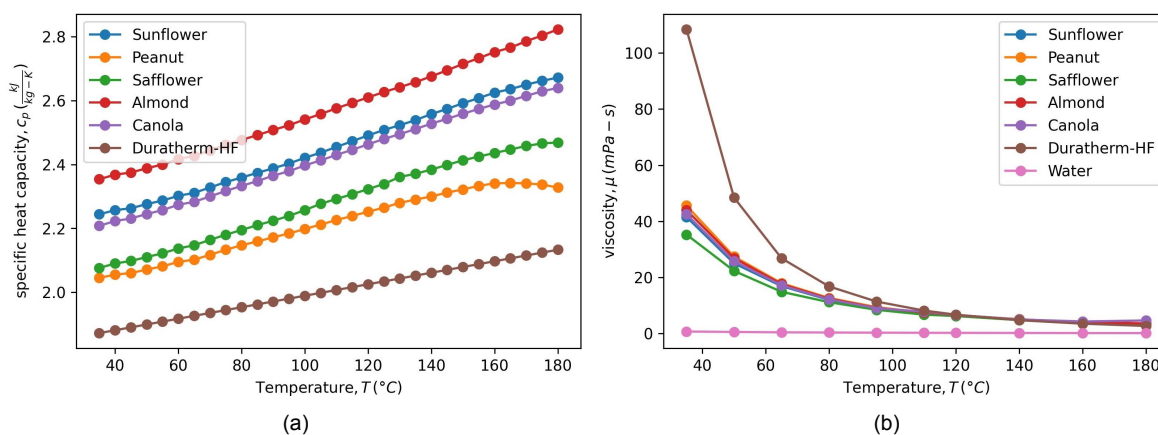


Figure 2.22: (a) Specific heat (c_p), and (b) Viscosity (μ) dependence on temperature (T) for different oils.

From Figure 2.22a, it can be observed that the specific heat for different oils varies significantly from each other at all temperature levels. Whereas, the viscosity tends to be similar for all oils beyond 60°C , as evident from Figure 2.22b. Moreover, the smoke point of all edible oils is well above 200°C [42].

A high specific heat oil is a desirable choice as it allows a low mass flow for a given heat duty and temperature difference. From Figure 2.22a, almond oil and sunflower oil have the highest specific heats among other oils with almond oil on the top. However, sunflower oil is more readily and cheaply available than Almond oil.

2.6. PTES Cycle Components

With reference to the process flow diagram shown in Figure 3.1, a PTES cycle mainly consists of heat interacting and work interacting devices. All kind of heat exchangers (eg: evaporator, condenser, recuperator, etc.) fall under the category of heat interacting devices while all turbomachines (eg: turbine, compressor, and pump) are categorised within work interacting devices. These two categories are primarily responsible for changing the thermodynamic state of working fluid in order to achieve the desired cycle output.

The following sections will focus on providing a theoretical background of these devices, their selection criteria and design procedure.

2.6.1. Heat exchange device

A heat exchanger (HEX), in principle, is employed to transfer heat from one substance to another by means of conduction, convection, radiation or a combination between these. In process industries, it is mainly the fluid streams which exchange heat. There are numerous heat exchangers which can be classified based on the application or the function required (eg: boiler, condenser, cooler, heat pipe, recuperator, etc.). However, this section will deal with the categorisation made on the basis of the technology used.

Based on the technology, heat exchangers can be classified into: shell & tube HEX, gasketed plate HEX, spiral plate HEX, printed circuit HEX, etc. Of these, the most common and standard HEX's are shell & tube, and plate heat exchangers which have a wide application. These two HEX's will only be discussed in this section.

Shell & Tube HEX

It is one of the most common type of HEX used in process industries [37, 81]. A typical sectional view of the shell & tube HEX is shown in figure 2.23.

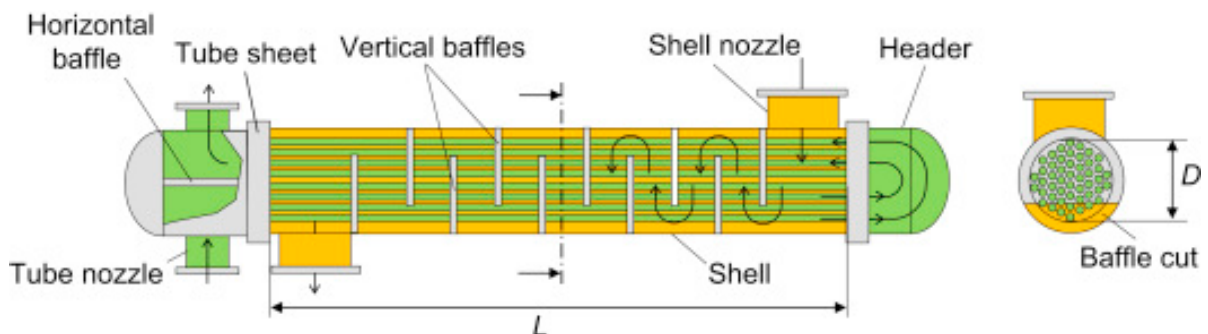


Figure 2.23: Sectional view of a shell & tube heat exchanger.

Mainly, it consists of a tube bundle enclosed within a cylindrical shell. The end of the tubes are held by the means of tube sheet, which separates the fluid at tube side and shell side. Throughout the length of the tubes, they are supported by vertical baffles which are also responsible to direct the shell side fluid across the tube bundle. Additionally, baffles also induce required turbulence which increases the heat transfer coefficient at shell side, but at a cost of higher pressure drop. The operating range of shell & tube HEX is included in Table 2.7.

Depending upon the design requirements, shell & tube HEX is available in different configurations as designated by TEMA and can be found in Sinott and Towler [81]. Similarly the tubes can be arranged in different configurations (eg; 1 pass, 2 pass, 4 pass upto 16 passes).

Apart from the design criteria, fluid allocation to shell side and tube side is often a challenge. There are some thumb rules that need to be considered while allocating the fluids:

1. Corrosion: most corrosive should be on tube side, since tubes are easy to replace.
2. Fouling: most fouling fluid should be on tube side, since tube side has higher velocity which minimizes fouling. Moreover tubes are easier to clean.
3. Operating pressures: high pressure fluid to be placed on tube side, otherwise, a pressurised shell would pose uneven stress on the outside of tubes, which could lead to tube rupture.
4. Viscosity: highly viscous fluids should be kept on shell side, since turbulent flow can be achieved at lower Reynolds number (~ 200) in shell [81].

Moreover, there are certain industrial practices which limit the fluid velocities and pressure drop on the shell side and tube side. These limits are illustrated in Table 2.5, and 2.6.

• **Fluid velocity:**

Type of fluid		Velocity	
		Tube side	Shell side
Liquids		1-4 m/s	0.3-1 m/s
Vapors*	Vacuum	50-70 m/s	
	atm pressure	10-30 m/s	
	high pressure	5-10 m/s	

Table 2.5: Fluid velocity limits in shell & tube HEX

*the lower values in the prescribed range are applicable to fluids with high mol. wt.

• **Allowable pressure drop:**

Type of fluid		Allowable Pressure drop ΔP (kPa)
Liquids	< 1 mPa-s	35
	1-10 mPa-s	50-70
Gas and Vapors	High Vacuum	0.4 - 0.8
	Medium Vacuum	$0.1 \times P_{abs}$
	1-2 bar	$0.5 \times P_{gauge}$
	> 10 bar	$0.1 \times P_{gauge}$

Table 2.6: Allowable pressure drop for fluids in shell & tube HEX

Gasket Plate HEX

A gasketed plate heat exchanger is another widely used HEX after shell & tube type. However much more compact and cheaper than shell & tube HEX. A schematic of a gasketed plate heat exchanger showing its working principle is illustrated in Figure 2.24.

It mainly comprises of a stack of thin metal plates, closely spaced, bolted and clamped together in a frame. Further, a thin gasket is used to seal the plates around the edges, which directs the fluid and prevent them from mixing. The plates also include corrugations carved on them in order to ensure efficient heat transfer across the plates. The corrugations tend to increase the surface roughness, which leads to a turbulent flow between the plates, thereby developing a high heat transfer coefficient, but again at a cost of a significant pressure drop.

Plate HEX's allow for pure counter-current flow, which further makes it possible to attain very low approach temperatures of upto 1 K [81]. They present a distinct feature of providing heat load flexibility. This means with a change in heat load, the number of plates can be adjusted (added or removed) to match the required area for desired heat load.

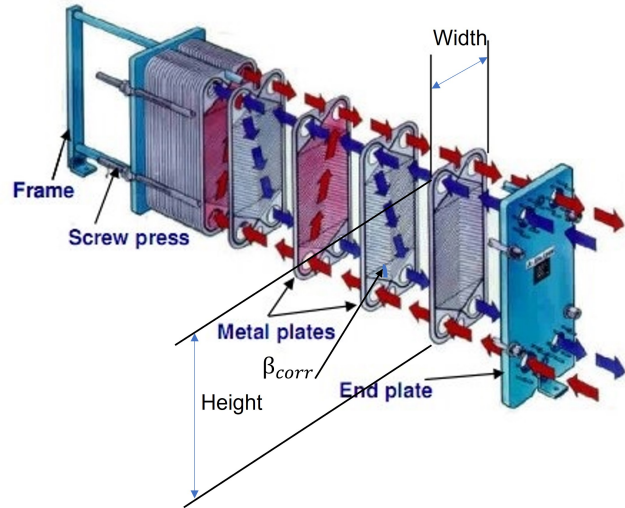


Figure 2.24: Schematic of a gasketed plate heat exchanger.

Gasket plate HEX also have certain industrial limitations. Due to the configuration of plates, they are poor at resisting high pressures. As such, they can not be used between fluid streams with high differential pressures. The operating range of gasket plate HEX is included in Table 2.7.

Type	Temperature (°C)	Pressure (bar)	$\Delta T_{approach, min}$ (°C)
Shell & Tube	-200 to 700	upto 200	10
Plate	-40 to 180	30	1

Table 2.7: Operating range of the shell & tube, and gasket plate HEX [81]

Design Procedure

The primary objective of carrying out a preliminary design of a heat exchanger is to evaluate the required heat transfer area and a corresponding overall heat transfer coefficient for the required heat duty Q . An overall heat transfer equation for such a system is given by,

$$Q = U_0 A \Delta T_m, \quad (2.12)$$

$$\Delta T_m = \frac{(T_{h,in} - T_{c,out}) - (T_{h,out} - T_{c,in})}{\ln\left(\frac{T_{h,in} - T_{c,out}}{T_{h,out} - T_{c,in}}\right)}. \quad (2.13)$$

where, ΔT_m is the Log Mean Temperature Difference (*LMTD*) and is calculated based on the Q-T diagram shown in Figure 2.25. *LMTD* is purely dependent on the process fluid operating conditions at the inlet and outlet of a heat exchanger. The *LMTD* calculated in Equation (2.13) is for a pure counter-current flow, however the actual flow path in heat exchangers is never 100% counter-current. In order to consider the effect of deviation from counter-current condition, an additional correction factor (F) is applied to the *LMTD* calculated from Equation (2.13). The overall heat load of a heat exchanger can then be written as:

$$Q = U_0 A (F \Delta T_m). \quad (2.14)$$

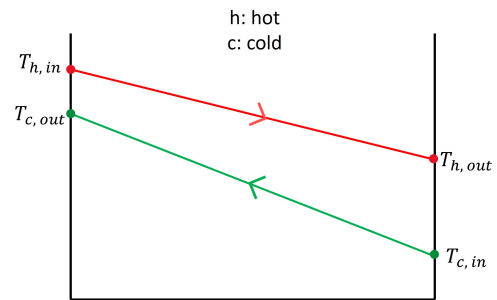


Figure 2.25: Q-T diagram for *LMTD* calculation for a pure counter-current flow.

A general procedure to carry out a preliminary design of a HEX is as follows:

1. Define the heat load (Q) and fluid stream properties. Evaluate any unknown data from the input conditions.
2. Calculate the *LMTD* from the fluid inlet-outlet temperatures based on Equation (2.25). Apply a necessary *LMTD* correction factor (F) based on the type of HEX.
3. Assume an overall heat transfer coefficient (U_0) for the type of fluids and nature of heat transfer. This value can be taken from standard books [37, 81].
4. Calculate the overall heat transfer area based on the assumed U_0 value.
5. Select a suitable and standard geometry to match the required area.
6. Calculate the individual heat transfer coefficients for both the fluid streams using standard correlations.
7. Calculate overall heat transfer coefficient from the individual coefficients while taking fouling resistance into consideration.
8. Check if the difference between assumed and calculated U_0 values is within 30%. If yes, continue further to evaluate pressure drop, otherwise, return to step 5 and change the geometry based on the calculated U_0 value.

A detailed design procedure and heat transfer correlations for different heat transfer conditions are included in Appendix E and Chapter 4 respectively.

2.6.2. Turbomachinery

Turbomachines, in principle, are devices in which energy is transferred between a rotor and a continuously flowing fluid. Either the kinetic energy of fluid is converted into pressure energy, as done in compressors, or the pressure energy is converted into kinetic energy, as in the case of expanders. A turbomachine consists of rows of stationary blades (stator) and rows of rotating blades (rotor), forming channels between consecutive blades as depicted in Figure 2.26.

A row of stator channels combined with a row of rotor channels form the stage of a turbomachine (0-1-2) from Figure 2.26. A turbomachine can have a number of stages, but is dependent on the work transfer to or from the fluid. Commonly, two types of turbomachines are widely employed in every industry: radial and axial turbomachine. For the former, the relative motion of the fluid flow is perpendicular to the rotor's rotational axis, making the fluid to come either radially inwards or outwards. On the other hand, for an axial machine, the fluid flow is approximately parallel to the rotation axis.

Based on the direction of energy transfer, a work producing turbomachine is termed as a turbine, while a work absorbing turbomachine is referred to as either pump (if the fluid is incompressible, eg: liquids) or compressor (for compressible fluids, eg: gases). Both the turbine and compressor have a radial and axial variant, which are employed based on a particular application.

The following sections will deal with the selection criteria and preliminary design procedure of turbomachines.

Selection of turbomachinery

The procedure to select a particular turbomachine and further its preliminary design is based on the use of similitude theory [40]. This theory allows to project the properties and configuration of real world machine (reference model) to a lab-scale model in order to analyse the performance of the reference model. Dimensional analysis is used to execute the similitude theory, which involves defining a physical phenomenon using a set of dimensionless numbers.

Applying dimensional analysis to turbomachines, the efficiency, η , can be defined in terms of four dimensionless parameters [40]:

$$\eta = f(\Pi_1, \Pi_2, \Pi_3, \Pi_4), \quad (2.15)$$

$$\Pi_1 \equiv \Phi = \frac{V}{\omega \cdot D^3}, \quad (2.16)$$

$$\Pi_2 \equiv \Psi = \frac{W}{\omega^2 \cdot D^2}, \quad (2.17)$$

$$\Pi_3 \equiv Re = \frac{\rho \cdot u \cdot D}{\mu}, \quad (2.18)$$

$$\Pi_4 \equiv M_u = \frac{u}{c_s}. \quad (2.19)$$

where, $\Pi_1, \Pi_2, \Pi_3, \Pi_4$ is correlated to flow factor (Φ), work factor (Ψ), Reynolds number (Re), and Mach number (M_u), respectively. Further, V is the volumetric flow rate (m^3/s), ω is angular velocity (rad/s), D is the diameter of the blade (m), W is the reversible work transfer (J/kg), μ is the fluid viscosity ($Pa \cdot s$) and c_s is the velocity of light (m/s).

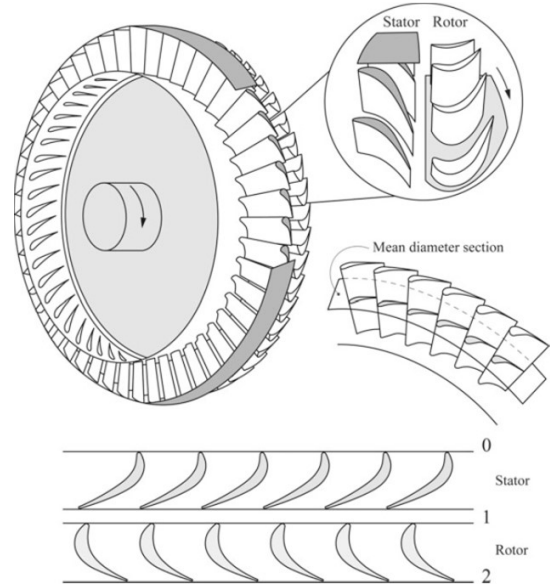


Figure 2.26: Schematic of a stage between stator and rotor of a typical axial turbine.

For a fluid with high Reynolds number ($Re > 10^6$), and Mach number sufficiently low ($M_u < 0.5$), the efficiency of the turbomachine is limited to a function of flow factor and work factor [40], which can be expressed as:

$$\eta = f(\Phi, \Psi). \quad (2.20)$$

A direct consequence of Equation (2.20) is that, two geometrically similar machines exhibit same efficiency if they have same Φ and Ψ factors, given that effects of Re and M_u are taken into consideration.

Dimensional analysis can be taken further to provide a preliminary design of different turbomachines. The design in this thesis has been carried out using the methodology developed by Balje [7, 8]. This method expresses the efficiency (η) of a turbomachine as a function of two other dimensionless parameters, specific speed (N_s), and specific diameter (D_s). Combining Equations (2.16) and (2.17) can lead to the following definitions of N_s and D_s ,

$$\eta = f(N_s, D_s), \quad (2.21)$$

$$N_s = \omega \cdot \frac{V^{0.5}}{W^{0.75}} = \frac{2\pi N}{60} \cdot \frac{(\dot{m}/\rho_{av})^{0.5}}{\Delta h_{is}^{0.75}}, \quad (2.22)$$

$$D_s = D \cdot \frac{W^{0.25}}{V^{0.5}} = D \cdot \frac{\Delta h_{is}^{0.25}}{(\dot{m}/\rho_{av})^{0.5}}. \quad (2.23)$$

where, \dot{m} is the mass flow (kg/s), ρ_{av} is the average density (kg/m^3) for inlet and outlet of each stage, and Δh_{is} is the enthalpy rise per stage (J/kg).

The importance of N_s can be realized by the fact that for a homologous series of turbomachinery, i.e. of a particular shape, have a particular value of N_s , for their maximum efficient operation. This means different families of turbomachinery will have different optimum range of N_s values. This is evident from the Figure 2.27 which gives an estimation of N_s values for different class of turbomachine and is adapted from the work of Lewis (1996) [72].

Centrifugal compressors are suited for low mass flow applications while working at highest efficiency for N_s values in the range of $0.4 < N_s < 1.8$. On the other hand, axial compressors are much efficient for high mass flow applications with an optimal N_s range of $1.5 < N_s < 10$. For radial turbines, N_s range for maximum efficiency of 90% is $0.5 < N_s < 0.6$ while axial turbines offer a wider range of N_s values, $0.5 < N_s < 0.9$, for efficiency values $> 90\%$. For radial pumps, the typical N_s values lies in the range of $0.5 < N_s < 1.3$ for high efficiency domain. These typical N_s range can be easily read from the Balje diagram, which is included in Chapter 4, where the preliminary analysis is done in detail. A quantitative comparison of axial and radial turbomachine characteristics is illustrated in Figure 2.28, where +++ signifies high, ++ medium, and + as low.

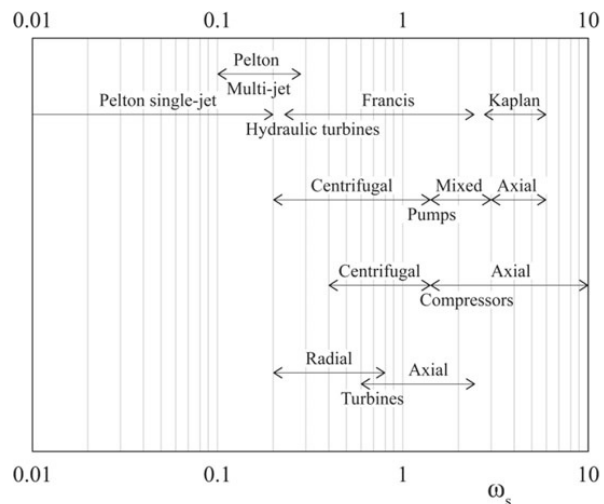


Figure 2.27: Turbomachines specific speed [40, 72]

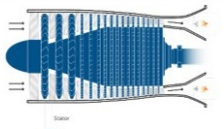
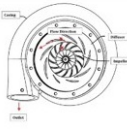
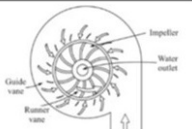
Compressor specifics	Axial flow	Radial flow	Turbine specifics	Axial flow	Radial flow
					
Pressure ratio per stage	Low	High	Pressure ratio per stage	Low	High
Overall pressure ratio	+++	+	Overall pressure ratio	+++	+
Maximum pressure ratio	High	Low	Maximum pressure ratio	High	Low
Airflow	High	Low	Airflow	High	Low
Size	+	+++	Size	+	+++
Simplicity	+	+++	Simplicity	+	+++
Investment costs	+	+++	Investment costs	+	+++
Efficiency range	High PR	Low PR	Efficiency range	>5 MW	<5 MW

Figure 2.28: Axial and radial compressor characteristics (left), Axial and radial turbine operating characteristics (right) [33]

Preliminary design procedure

The key to preliminary sizing of a turbomachinery is the Balje diagram as shown in Figure 4.6, 4.7. A detailed analysis for preliminary sizing is done in Chapter 4. The generalised steps of basic turbomachinery sizing are as follows:

1. Select the axial or radial turbomachinery based on the operating characteristics (power, pressure ratio, etc.).
2. Estimate optimum number of stages and angular velocity (N) from the N_s range for best efficiency.
3. Estimate the N_s value per stage
4. Read D_s value from the Balje diagram for best possible efficiency.
5. Evaluate the tip diameter (D) of the impeller per stage from the D_s equation.

2.7. Research Objectives, Scope and Goal

Following the detailed literature study on PTES systems, the waste heat integrated PTES based on Rankine system or Compressed Heat Energy Storage (CHEST) system is considered as the focus of this thesis. The main research objective can be formulated as follows:

Research Objective 1:

“To develop and optimize a steady-state thermodynamic model of a CHEST system based on a full sensible storage.”

Within this research objective, there are further research questions that needs to be answered, such as:

- What are the effects of the thermodynamic cycle parameters on the performance of the system and the energy storage density of the TES?
- What are the technological differences between a sub-critical and trans-critical CHEST system?
- How the optimised CHEST system can be integrated with a solar powered alkaline electrolyser unit to recover its waste heat?

In addition, the efficiency of the system is highly dependent on the thermodynamic performance of the system components, i.e. heat exchangers and turbomachines. The work of H. Jockenhöfer et al. (2018) provides an estimate of the exergy losses across each component [49] for a typical CHEST system. It focuses mainly on improving the performance of the heat exchangers and turbomachines. This leads to defining the second objective of this thesis:

Research Objective 2:

“To provide an estimate of the overall dimensions and performance characteristics of CHEST components (heat exchangers and turbomachines) by conducting a preliminary design.”

Within this research objective, the key aspects to be studied are as follows:

- Selection of the components based on their operating conditions.
- To analyse the results of the preliminary design, such as the effect of pressure drop across HEX and turbomachinery efficiency on the system performance.

Having defined the research objectives, the **Goal** of this thesis is to extend the existing sub-critical CHEST system by DLR [49] with latent TES to a solely sensible heat storage configuration. The findings of this research can be further used to discover specific combination of working fluid and storage medium, which provides minimum exergy losses. The target of this thesis is not restricted by steady state modelling, but can be extended to off-design modelling and dynamic simulations as a following research project.

Further, the **Scope** of this thesis is restricted to using pure fluids with steady-state thermodynamic modelling of the CHEST system. It also includes an optimization scheme to evaluate the operating conditions for the best performance. Finally, based on the optimised results, a preliminary design of the CHEST components are proposed.

2.8. Thesis Outline

This section summarises, in brief, the content of the next chapters and provides a flow of the thesis work.

Chapter 3 discusses the thermodynamic model development of a waste heat integrated PTES system. Further, a sensitivity analysis has been carried out on the model to look the effect of various thermodynamic parameters on the round trip efficiency of the system and performance of the storage. Finally, two optimised PTES configurations have been compared based on performance, and economical aspects.

Chapter 4 uses the optimised thermodynamic model from Chapter 3 to apply in a case study. The case study focuses on integrating waste heat from solar power alkaline electrolyzer into a PTES system. The output parameters from the case study are further used to provide a preliminary design of cycle components, i.e. heat exchangers and turbomachines.

Chapter 5, finally, concludes the results obtained and discuss the potential applicability of the proposed system. Further, recommendations for the improvement of the model and future work have been proposed.

Thermodynamic Design of CHEST

3.1. Introduction

The previous chapters have provided all the necessary literature required for designing a thermodynamic model of Pumped Thermal Energy Storage (PTES) system. This chapter will make use of this knowledge to carry out the analysis on a waste heat integrated Rankine PTES system or CHEST system. A computational model has been developed to design such system and observe the effect of various parameters on the efficiency of the system. A conceptual process flow diagram of the CHEST system is shown in Figure 3.1.

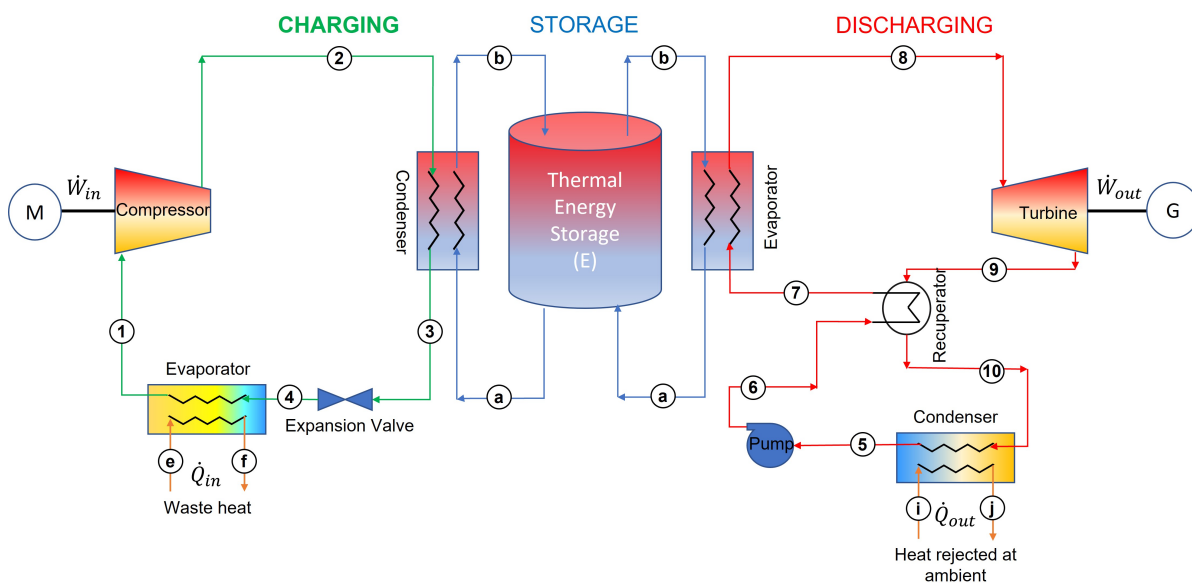


Figure 3.1: Conceptual process flow diagram of the CHEST system for the present work.

The working principle of the system, shown in Figure 3.1, has already been discussed in Chapter 2.3. In general, a low grade waste heat (\dot{Q}_{in}) can be used as a feed at the heat pump evaporator in the charging cycle. The rest of the cycle follows the standard refrigeration/heat pump cycle. The heat rejected in the condenser of heat pump (2-3) is stored in the thermal energy storage medium. This heat is further extracted by the working fluid during the discharge cycle (6-7), which follows a standard Rankine cycle, and produces work (\dot{W}_{out}) through a turbine.

Based on the conceptual PFD shown in Figure 3.1, the work carried out in this project will present a suitable combination of working fluid and storage medium. Further, possible design configurations of

the charging, discharging and storage cycles will be developed based on the PFD shown in Figure 3.1 and then optimised and compared to arrive on a promising design solution.

3.2. Thermodynamic Model Development

This section enlists the methodology followed for the development of the thermodynamic model and analyzing the thermodynamic cycle. The procedure is as follows:

1. Defining the model objectives.
2. Listing the model input and output parameters.
3. Formulation of design assumptions.
4. Creation of required sub-models.
5. Applying necessary conservation laws and writing simplified constitutive equations.
6. Performing sensitivity analysis for sub-models.
7. Implementation on different design configurations.
8. Optimization of the thermodynamic system to fulfill necessary requirements.

The following sub-sections discuss the steps from 1 to 3. Section 3.3 discuss the different sub-system models (step 4). Appendix D provides the details of step 5. Further, step 6 is discussed in section 3.4 and finally sections 3.5 & 3.6 look into the steps 7 & 8.

3.2.1. Model objectives

As a first step, it is paramount to define the fundamental purpose of the thermodynamic model, the kind of problem addressed by the model and key requirements of the model. For a typical CHEST system, the model shall provide the round trip efficiency of the system and design inputs for different components, which can be compared for various design configurations. The objectives of the thermodynamic model and its key requirements are summarised in Table 3.1.

Model Criteria	Definition
Purpose	The model will be developed to provide the thermodynamic performance (RTE) of the CHEST system and the design requirements of the individual components, at the operating conditions.
Problem	Steady-State model
Requirements	<ol style="list-style-type: none"> 1. The system model shall follow the lumped component model. 2. The model shall use a modular approach. 3. The model shall allow for analysing the effect of various design parameters on the sytem performance.

Table 3.1: Modelling criteria

3.2.2. Design input & output parameters

Table 3.2, lists out all the primary input parameters required to process the thermodynamic model of the CHEST system based on the PFD shown in Figure 3.1. Moreover, it also lists the required output parameters from the model.

Fixed Input Parameters		Optimised Output Parameters	
Waste heat input	\dot{Q}_{in}	Cycle temperature and pressure	T, P
Waste heat temperature	T_e	Performance of heat pump	COP
Evaporator temperature of heat pump	T_4	Thermal efficiency of heat engine	η_{th}
Maximum hp cycle temperature and pressure	T_2, P_2	Mass flow rate of working fluid	$\dot{m}_{hp}, \dot{m}_{he}$
Ambient temperature	T_i	Mass flow rate of storage medium	$\dot{m}_{storage}$
Condensation temperature of heat engine	T_5	Compressor work input	\dot{W}_{in}
Degree of superheat, (ΔT_{sup})	$T_1 - T_4$	Turbine work output	\dot{W}_{out}
Maximum and minimum storage temperature	T_b, T_a	Recuperator heat load	\dot{Q}_{rec}
Compressor efficiency	$\eta_{is, comp}$	Mass flow waste heat stream	\dot{m}_{waste}
Turbine efficiency	$\eta_{is, turb}$	Mass flow ambient stream	$\dot{m}_{ambient}$
Pump efficiency	$\eta_{is, pump}$	Storage size	V
Pinch across each heat exchanger	ΔT_{pinch}	Energy storage capacity	E
Charging-discharging duration	t_{ch}, t_{dch}	Round Trip Efficiency	η_{RTE}

Table 3.2: Input and output parameters of the thermodynamic model.

The choice of input values (eg: T, P) will be based on the sensitivity analysis, which is carried out to analyse their effect on the system performance.

3.2.3. Design Assumptions

The model has been developed based on a steady-state computation and specific assumptions have been made to simplify the model. The assumptions have been specifically applied to different system components, which have been mentioned in Appendix D. The overall assumptions made are as follows:

- The effects of the variation of potential energy, and kinetic energy across each component is considered to be negligible.
- All the component systems have been considered to be thermally insulated from the surroundings, thereby applying an adiabatic model across each component.
- The heat exchangers have been modelled considering a zero pressure drop, thereby using a constant pressure model across each heat exchanger.
- Further, frictional pressure drop in the connecting conduits/lines have been assumed negligible.

3.3. Subsystem Models

The complete CHEST thermodynamic model has been divided into four different subsystem models, where each module has its own set of conservation and constitutive equations. The advantage of the modular approach is that, each subsystem model can be changed independently pertaining to the system configuration required. The following subsections discuss each of the subsystem model.

3.3.1. Working fluid model

From Figure 2.21, the three fluids compared were R1233zD, Butane and Butene. The latter two fluids shared similar thermophysical properties. It was seen that R1233zD was dominant in terms of molecular weight while Butane & Butene held twice the latent heat of vaporization as compared to R1233zD. This leads to a similar energy per unit volume ($\rho_V * \Delta h_{LV}$) of the vapor for all the three fluids, which doesn't have a significant difference in the compactness of the cycle components. Further, R1233zD has been reported to be inflammable while Butane and Butene are highly flammable.

Considering from safety point of view, R1233zD outperforms rest of the fluids compared. Moreover, it has a lower critical pressure ($\sim 35 \text{ bar}$) and an appropriate critical temperature as required for a CHEST system. So, R1233zD has been selected as the working fluid for the CHEST system developed in this work. The thermophysical properties of this fluid had been listed in Table 2.3.

In the operating thermodynamic cycles, the working fluid properties at individual state points have been evaluated using the CoolProp package in Python [11]. Further REFPROP has been chosen as the backend property evaluator for CoolProp. REFPROP uses the Helmholtz Equation Of State (HEOS) of Mondejar et al. (2015) to evaluate the properties of R1233zD(E) [63]. The advantage of using HEOS is that it allows to develop an EOS explicit in Helmholtz energy and all other thermodynamic properties can be estimated using the partial derivatives of Helmholtz energy [92]. The HEOS for pure fluids can be represented in dimensionless form as given in [57, 92]:

$$\frac{A}{RT} = \alpha(\tau, \delta) = \alpha^0(\tau, \delta) + \alpha^r(\tau, \delta), \quad (3.1)$$

$$A = U - TS$$

where, A , & R represents the molar Helmholtz energy, and universal gas constant respectively. The Equation (3.1) consists of two non-dimensional parts, (i) ideal Helmholtz energy denoted by α^0 , and (ii) the residual Helmholtz energy denoted by α^r . These are a function of two independent dimensionless parameters, (i) inverse reduced temperature, $\tau = T_c/T$, and (ii) reduced density, $\delta = \rho/\rho_c = V_c/V$.

Unlike the ideal fluid conditions, some of the properties extensively estimated at every state point, such as specific enthalpy (h), sepcific entropy (s), etc. are a function of both temperature and pressure in single phase regions, given by:

$$h = h(T, P); s = s(T, P).$$

In the two-phase region, these properties are a function of a single independent variable, either temperature or pressure.

3.3.2. Heat pump model

The heat pump has been modelled based on a single stage configuration of reverse Rankine cycle as shown in Figure 3.1 as a charging cycle.

Thermal heat input and mass flow of working fluid in heat pump

As indicative from Figure 3.1, the waste heat has been coupled with the heat pump evaporator. For preliminary analysis, 1 MW of waste heat has been considered to feed the heat pump. A constant pressure model has been used for heat pump evaporator and is only a function of evaporator temperature, i.e. $P_{evap} = P_{sat}(T_{evap})$. Using Equation (D.5), the mass flow rate of the working fluid of heat pump (\dot{m}_{hp}) can be evaluated from the energy balance across evaporator. A Q-T diagram for the waste heat source and evaporator is shown in Figure 3.2.

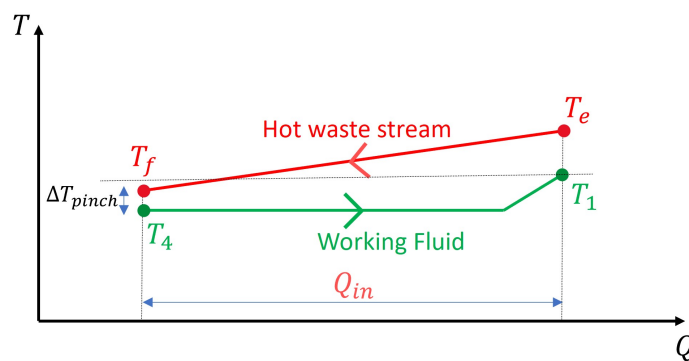


Figure 3.2: QT diagram for HP evaporator

A minimum pinch (ΔT_{pinch}) is set at the evaporator inlet (T_4) to limit the maximum temperature change in hot waste stream. Moreover, a pinch at the evaporator inlet provides a flexibility for the amount of superheat that can be provided towards evaporator outlet (1). For the fixed waste heat inlet temperature (T_e) and ΔT_{pinch} , a higher temperature change in the waste heat stream will lower the heat pump evaporator operating temperature, which will reduce the performance of the heat pump, as can be inferred from Equation (3.3). The outlet waste stream temperature (T_f) needs to be limited and is dependent on the source of waste heat. This choice of waste heat outlet temperature (T_f) will be made during the analysis carried out for the case study in Chapter 4. Following this, the mass flow rate of the waste heat stream required can be similarly calculated using the energy balance equation across the evaporator:

Total energy transferred from heat pump to TES

A constant pressure model has been used for the cooling/condensation of high pressure, high temperature working fluid (gaseous state) from the compressor outlet. The heat released during cooling/condensation has been stored in the High Temperature-TES (HT-TES). A charging duration (t_{ch}) of 8 hours is assumed, which leads to the total energy transferred by heat pump equivalent to:

$$E_{stor} = \dot{m}_{hp} (h_2 - h_3) t_{ch}. \quad (3.2)$$

An Energy-Temperature (E-T) plot, as shown in Figure 3.3, provides a demonstration of the energy transfer between heat pump and storage medium. Figure 3.3a depicts the energy transfer to a combination of latent and sensible storage, whereas, Figure 3.3b depicts energy transfer to a sole sensible storage.

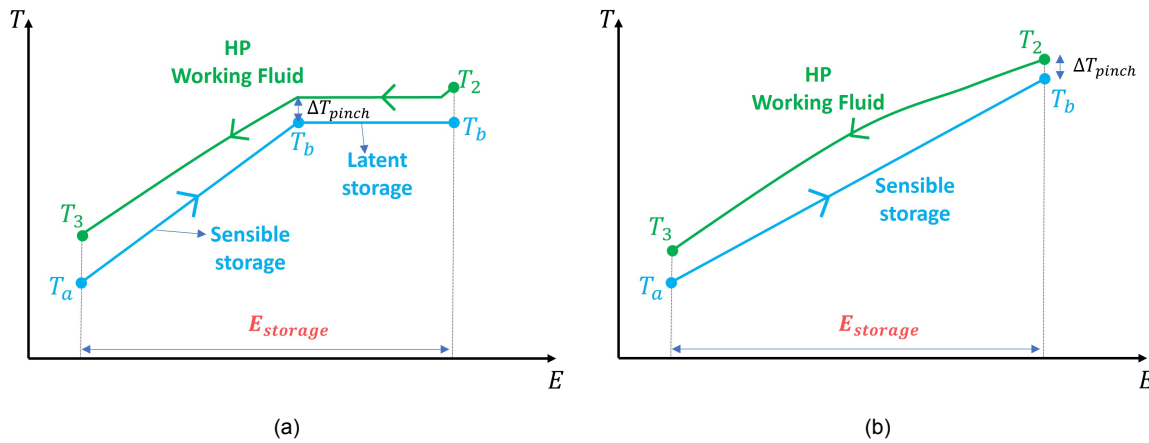


Figure 3.3: E-T diagram depicting energy transfer between heat pump and storage during charging cycle for (a) latent storage, and (b) sensible storage configuration.

For the configuration shown in Figure 3.3a, the storage medium can have a pinch only at the inlet of latent storage or outlet of sensible storage. While for the configuration in Figure 3.3b, a minimum pinch is set at the outlet of the sensible storage. This allows to limit the maximum storage temperature T_b and simultaneously gives flexibility for a choice of low storage temperature (T_a). A high temperature difference for storage medium ($T_b - T_a$) implies a less volume of storage needed for same amount of energy stored.

COP of heat pump

For ideal conditions, Coefficient of Performance (COP) of a heat pump is dependent on the thermodynamic mean temperature of heat source ($T_{m,source}$) and heat storage ($T_{m,storage}$), which is given by the following relation:

$$COP_{ideal} = \frac{T_{m,storage}}{T_{m,storage} - T_{m,source}}. \quad (3.3)$$

However, COP of the heat pump in this system is defined as the ratio of total energy stored in the TES to the total work input in the compressor. It has been calculated using the following relation:

$$COP = \frac{E_{stor}/t_{ch}}{\dot{W}_{comp}} = \frac{(h_2 - h_3)}{(h_2 - h_1)}. \quad (3.4)$$

The pressure ratio of a compressor has a direct impact on the COP. A higher pressure ratio will lead to high compressor outlet temperature, which will eventually increase the enthalpy (h_2) at the outlet. As such requiring more electric work and thus, lowering the COP. Therefore, for the same condenser pressure, a higher evaporator pressure will result in a lower input work and an improved COP.

3.3.3. Heat engine model

The heat engine has been modelled based on a single stage configuration of an organic Rankine cycle as shown in Figure 3.1 as a discharging cycle.

Heat input and mass flow of working fluid in heat engine

The stored energy from HT-TES is fed to the heat engine evaporator, which has also been modelled based on a constant pressure model, i.e. $P_{evap} = P_{sat}(T_{evap})$. An initial discharge duration (t_{dch}) of 8 hours is assumed. Using Equation (D.5), the mass flow rate of the working fluid can be evaluated as follows:

$$\dot{m}_{he} = \frac{E_{stor}/t_{dch}}{(h_8 - h_7)} = \frac{\dot{m}_{hp} (h_2 - h_3) (t_{ch}/t_{dch})}{(h_8 - h_7)}. \quad (3.5)$$

where, h_8 and h_7 is the specific enthalpy (kJ/kg) of the working fluid at the outlet and inlet of the heat engine evaporator respectively in Figure 3.1. The Energy-Temperature (E-T) plot shown in Figure 3.4 provides a demonstration of the energy transfer between storage medium and heat engine. Figure 3.4a depicts the energy transfer from a combination of latent and sensible storage, whereas, Figure 3.4b depicts energy transfer from a sole sensible storage.

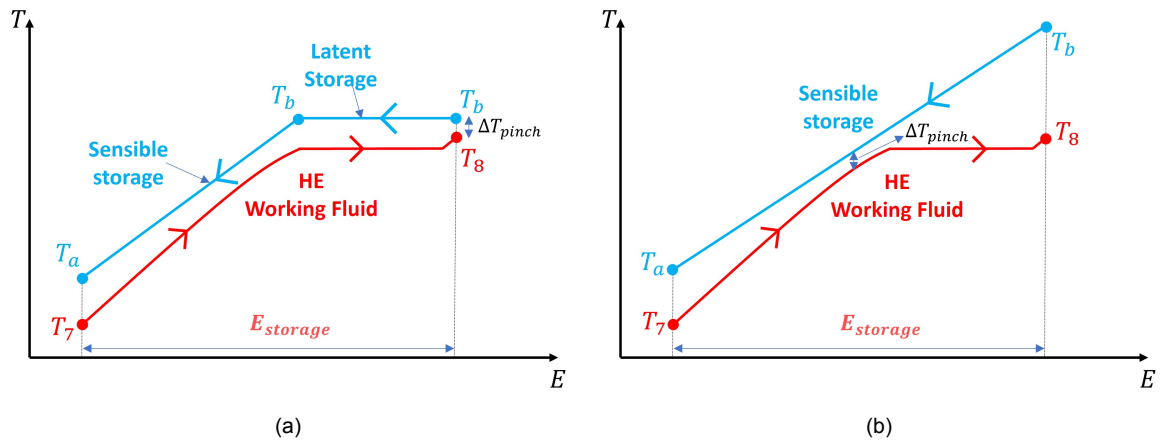


Figure 3.4: E-T diagram depicting energy transfer between storage and heat engine during dis-charging cycle for (a) latent storage, and (b) sensible storage.

For the configuration shown in Figure 3.4a, the storage medium can have a pinch only at the outlet of the heat engine evaporator (T_8). While for the configuration shown in Figure 3.4b, a minimum pinch is observed somewhere in the sensible heat transfer region. This is primarily due to the curvature of isobar of the working fluid. This limits the minimum storage temperature T_a , which must be high enough as compared to T_7 in order to operate within the desired range of heat source and heat sink temperatures.

Thermal efficiency of heat engine

The thermal efficiency (η_{th}) of the heat engine is defined as the ratio of total work obtained from the turbine to the total energy received from the TES. It has been calculated using equations 3.5 and D.8, and is formulated as follows:

$$\eta_{th} = \frac{\dot{W}_{turb}}{E_{stor}/t_{dch}} = \frac{(h_8 - h_9)}{(h_8 - h_7)}. \quad (3.6)$$

The pressure ratio of a turbine has a direct impact on the thermal efficiency of heat engine. A higher pressure ratio will lead to low turbine outlet temperature, which will increase the enthalpy difference between the inlet and outlet of the turbine. As a result, it will increase the power output from the turbine as evident from Equation (D.8). Therefore, for a fixed turbine inlet conditions, a lower condensation pressure will increase the work output from a turbine and thereby boost the thermal efficiency of the heat engine cycle.

Heat sink and heat engine condenser

The operating pressure of heat engine condenser is crucial in producing work output from the heat engine. The effect of condenser pressure on heat engine performance is explained in the above subsection. A lower condensation pressure is thus favourable. A Q-T plot, as shown in Figure 3.5, exhibits the heat transfer between heat engine working fluid and ambient in a condenser.

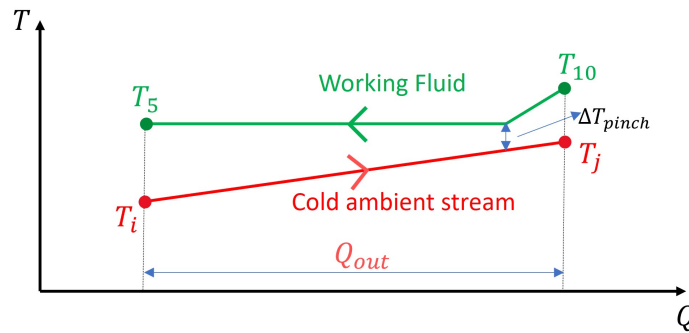


Figure 3.5: QT diagram for heat engine condenser based on the PFD shown in Figure 3.1.

Since, the ambient fluid stream has fixed inlet conditions, the outlet is determined by the mass flow of the ambient fluid stream. A higher temperature difference ($T_j - T_i$) resulting from lower mass flow rates of the ambient stream will lead to increased saturation pressure of the condenser, in order to satisfy the fixed pinch conditions. An increase in condenser pressure is undesirable due to reduced heat engine efficiency. The temperature difference of the cold ambient stream is limited and chosen according to the conditions mentioned in the case study in Chapter 4. Following this the mass flow rate of ambient stream is calculated based on the energy balance across the condenser.

3.3.4. Thermal energy storage model

Sensible storage medium

Referring to Figure 2.13, for an ideal CHEST system, the variation in the performance of the system, beyond a storage temperature of 200°C , is less significant. For any given waste heat source temperature and pinch, the RTE is observed to be merely constant after this temperature. From section 2.5.3, thermal oils could be used as a sensible storage medium pertaining to the maximum storage temperature limit of 200°C , since oils usually have a smoke point above 200°C and are quite thermally stable below this temperature. Moreover thermal oils could be easily stored at ambient pressure, thus eliminating the need of pressurised storage tanks (eg: in case of hot water storage).

As can be inferred from the Figures 2.22a and 2.22b, sunflower (SF) oil demonstrates a high specific heat capacity as compared to other thermal oils, while the viscosity is roughly similar for every oil in the

temperature range of 80–200°C. In addition to high specific heat capacity, and good thermal stability, SF oil is readily and cheaply available, which makes it a cost-competitive thermal energy storage medium. As a result, sunflower oil has been selected as the sensible storage medium for the CHEST system developed in this work.

The SF oil has been considered as an ideal and Newtonian fluid. This implies that the ideal fluid conditions can be applied on SF oil. For example, the enthalpy will only be a function of temperature, i.e. $h = h(T)$. Similarly, all other relevant properties such as specific heat, density, viscosity, thermal conductivity, etc. are also purely dependent on temperature.

Further, the specific enthalpy (h) can be expressed in terms of temperature by the following relation:

$$\Delta h = \int_0^T c_p(T) dT \quad (3.7)$$

where, $c_p(T)$ is the specific heat (J/kg-K) of the storage medium and is dependent on temperature. Ashmore et al. (2014) provides a correlation depicting the specific heat dependence of sunflower oil on temperature and is given as follows [60]:

$$c_p(T) = 2115.0 + 3.13T, \quad (3.8)$$

where, T is the temperature in degree celcius.

Latent storage medium

A list of inorganic phase change materials can be found in the Figure D.6. Of these, the potential PCM's are listed in the following table:

PCM	Phase change temperature [°C]	Phase change enthalpy [kJ/kg]
$KNO_3 - NaNO_2 - NaNO_3$ (eu)	142	80
$KNO_3 - LiNO_3$ (eu)	133	170
$LiNO_3 - NaNO_3$ (eu)	194	265

Table 3.3: Thermophysical properties of selected PCM's

For R1233zD(E) as the working fluid, a suitable PCM must have a melting temperature sufficiently below the critical temperature $T_c = 165^\circ C$ of the working fluid. However, a very low melting temperature will lead to low maximum heat engine temperature (T_8), which will reduce the thermal efficiency of the heat engine. The PCM should also possess a high phase change enthalpy (Δh_m). A higher Δh_m implies a lower storage volume. Comparing the PCM's listed in Table 3.3, all of them lack one or the other necessary conditions mentioned above.

In this thermodynamic model, a hypothetical PCM is considered with a melting temperature of $T_m = 150^\circ C$, and phase change enthalpy, $\Delta h_m = 200 \text{ kJ/kg}$.

Energy storage and mass flow rate

The total energy storage ($E_{storage}$) in the storage medium corresponds to the energy rejected by the heat pump in the charging cycle during an assumed charging duration (t_{ch}) and is given by the Equation (3.2). The same energy is discharged during the heat engine cycle within the desired discharge duration (t_{dch}). A different charging and discharging duration leads to different mass flow rates of storage medium during the charging (m_{ch}) and discharging (m_{dch}) cycle, which is given by:

$$\dot{m}_{ch} = \frac{E_{sen,stor}/t_{ch}}{h_b - h_a} \quad (3.9)$$

$$\dot{m}_{dch} = \frac{E_{sen,stor}/t_{dch}}{h_b - h_a}. \quad (3.10)$$

where, h_b & h_a correspond to the enthalpy of storage medium at maximum and minimum storage temperature respectively. A pinch of 2K is provided between the storage and charging-discharging temperature profiles to account for continuous heat transfer.

For latent heat storage, the amount of mass required is constant during charging and discharging cycles and is calculated using:

$$m_{lat}(kg) = \frac{E_{lat,stor}}{\Delta h_m} = \frac{\dot{Q}_{ch,lat} * t_{ch}}{\Delta h_m} = \frac{\dot{Q}_{dch,lat} * t_{dch}}{\Delta h_m}. \quad (3.11)$$

Storage volume

For a liquid sensible heat storage medium, the variation in the density with temperature is not much significant. This leads to using a constant density for the sensible storage medium. Following the mass flow rate equations 3.9 and 3.10, the total storage volume required has been calculated as follows:

$$V_{sen}(m^3) = \frac{\dot{m}_{ch} * t_{ch} * 3600}{\rho} = \frac{\dot{m}_{dch} * t_{dch} * 3600}{\rho}. \quad (3.12)$$

For the latent storage medium, the density remains to be constant. The volume required for a latent storage is calculated using the following relation:

$$V_{lat}(m^3) = \frac{m_{lat}}{\rho}. \quad (3.13)$$

3.4. Sensitivity Analysis

This section will look into the effects of the operating conditions, as mentioned in Table 3.2, on the round trip efficiency and storage size of the thermally integrated PTES system. The analysis has been carried out on a basic T-S diagram as shown in Figure 3.6.

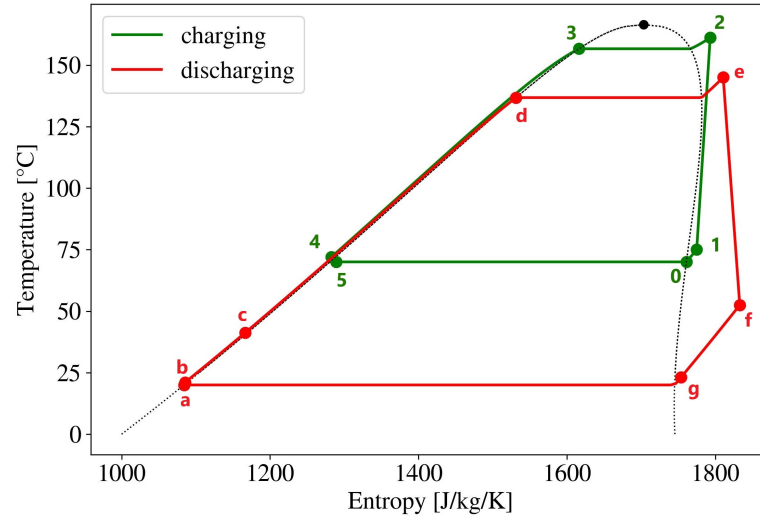


Figure 3.6: A basic T-S diagram showing the cycle integration.

3.4.1. Storage Temperature

The maximum heat pump cycle temperature and pressure plays a critical role in deciding the maximum temperature of the TES and optimizing the performance of the system. However, no optimization will be carried out in this section and will be performed later in this chapter. As a first analysis, the effect of pressure ratio of the charging cycle and maximum discharge cycle temperature will be seen on the round trip efficiency (RTE) of the system and TES storage size.

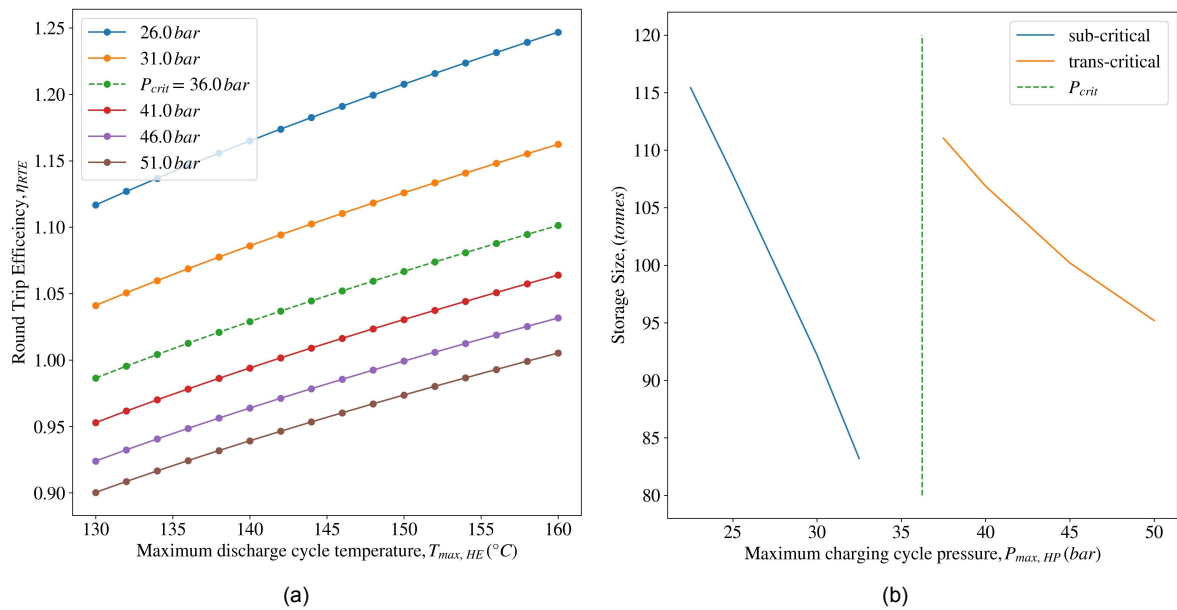


Figure 3.7: Effect of maximum heat engine cycle temperature and heat pump pressure ratio on (a) RTE, (b) storage size (tonnes) computed for a charging duration of 8 hrs and a waste heat load of 1 MW.

The plots shown in Figure 3.7 have been developed for a waste heat load of 1 MW, which is fed at heat pump evaporator (5-0) in Figure 3.6. To analyse the effect of the heat pump pressure ratio (P_2/P_1) and maximum heat engine cycle temperature (T_e), a constant degree of superheat (ΔT_{sup}) before compressor inlet ($T_1 - T_0$) and a constant discharge cycle pressure ratio (P_e/P_f) have been assumed. As can be inferred from Figure 3.6, a minimum (ΔT_{sup}) is essential to ensure the vapor compression doesn't occur in the two-phase region. For Figure 3.7b, storage size is compared for both sub-critical and trans-critical cycle. A combination of latent and sensible storage is used for sub-critical case and represents the total storage size. On the contrary, only sensible storage is considered for trans-critical case, and it represents sensible storage size.

From Figure 3.7a, it can be observed that increasing the maximum discharge cycle temperature (T_e) augments the performance of the system. However, the RTE decreases with increasing charging cycle pressure ratio. Increasing pressure ratio has a direct implication on increasing the temperature lift of heat pump, which tends to decrease the performance of the system. Whereas, the higher the difference in the temperature levels ($T_e - T_f$) in the heat engine cycle, higher would be the thermal efficiency of the cycle.

From Figure 3.7b, it can be deduced that storage size reduces for both sub-critical and trans-critical case with increasing pressure ratio. As discussed previously, increasing the heat pump pressure ratio, raises the maximum charging cycle temperature. This proportionately impacts the hot storage temperature. With increase in maximum cycle temperature, hot storage temperature also increases. A large ΔT between low temperature and hot temperature side of the storage will require a less mass to store an equal amount of heat. Similarly for the sub-critical case, higher the pressure ratio, higher is the condensation temperature (T_3). A high condensation temperature implies a lower available latent heat. This further points out that a lower latent storage would be required for a higher pressure ratio.

Effect of superheating on system performance with a superheater before compressor inlet

From the previous analysis, superheating was kept constant and effect of PR was observed on RTE and storage size. For this case, a PR of 9 in charging cycle is considered and the superheating before the compressor inlet is varied using a superheater. This superheater provides heat to the fluid stream inlet to the compressor, from the fluid stream discharging heat to the storage. From Figure 3.6, a superheater can be ideally placed between (3-4 and 1-0).

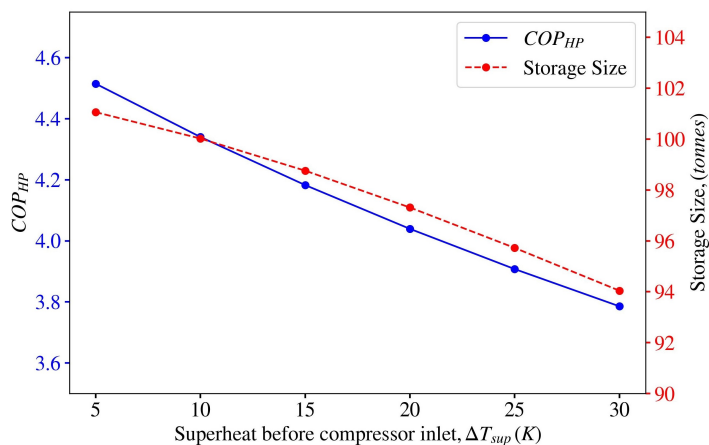


Figure 3.8: Effect of superheating before the inlet of compressor, with the help of a superheater, on RTE and storage size of the system.

From figure 3.8, it can be observed that using a superheater can lead to lower performance values of a heat pump. This is because, for the same pressure ratio (P_2/P_1) in the charging cycle, increasing the superheating also elevates the maximum cycle temperature (T_2), which can be inferred from Figure 3.9. A higher temperature lift requires additional input electrical work. Moreover, a part of the heat discharged to the storage is used for this superheating, which minimizes the positive effect of increased energy storage by increasing T_2 .

Further, the storage size can also be seen to decrease with a high degree of superheat. Again, this is attributed to the elevation in maximum heat pump cycle temperature (T_2), which leads to a higher hot storage temperature.

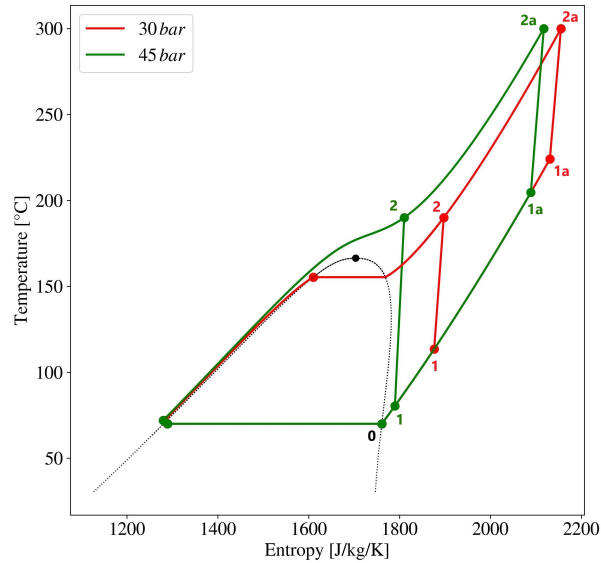


Figure 3.9: A T-S representation to demonstrate the effect of maximum temperature & pressure on superheating before compressor inlet.

Effect of maximum temperature & pressure on superheating before compressor inlet

Taking reference from Figure 3.9, it is certain that with an increase in maximum cycle temperature, the amount of superheating before compressor inlet increases, i.e. $\Delta T_{sup}(1a - 0) > \Delta T_{sup}(1 - 0)$. On the other hand, an increase in maximum cycle pressure tends to reduce the amount of superheating at the compressor inlet. From Figure 3.8, a higher degree of superheat leads to lower performance values. However, a lower value of superheating can lead to two phase compression. So a trade-off has to be set between the maximum operating temperature and pressure for charging cycle, such that, lowest possible superheating is favoured without entering into the two phase region, which can be assisted with the help of the plot shown in Figure 3.10.

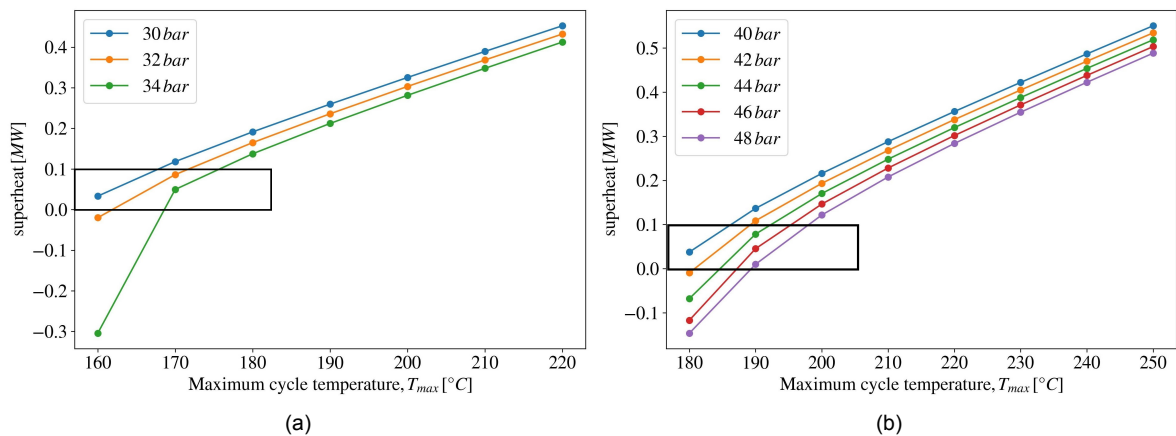


Figure 3.10: Effect of maximum hp cycle temperature & pressure on amount of superheat needed before the inlet of compressor for (a) sub-critical mode, and (b) trans-critical mode.

The choice of maximum temperature and pressure is different for heat pump operating in sub-critical and trans-critical mode. The choice can be made for both sub-critical and trans-critical operating

modes from Figure 3.10a and 3.10b respectively. For sub-critical mode, maximum temperatures less than 170°C will keep the amount of superheating within 10% of heat load at evaporator. But, the pressure value has to be chosen carefully. A higher pressure at low maximum temperature will result in two-phase compression, which must be avoided. Similarly, for trans-critical mode a maximum temperature less than 200°C could be taken into consideration. Moreover a pressure value providing the best performance from Figure 3.7 could be selected.

3.4.2. Waste heat temperature

Low grade waste heat, in general, is available at temperatures in the range of $50 - 100^{\circ}\text{C}$ [52]. The quality of waste heat is determined by the temperature at which it is available. Higher the temperature, higher is the grade of waste heat. This section will analyse the effect of waste heat temperature on the RTE of the CHEST system. For this, the other operating conditions such as cycle maximum temperature & pressure have been fixed. The waste heat load is kept constant at a value of 1 MW and the thermal efficiency of the discharge cycle is assumed to be 20%.

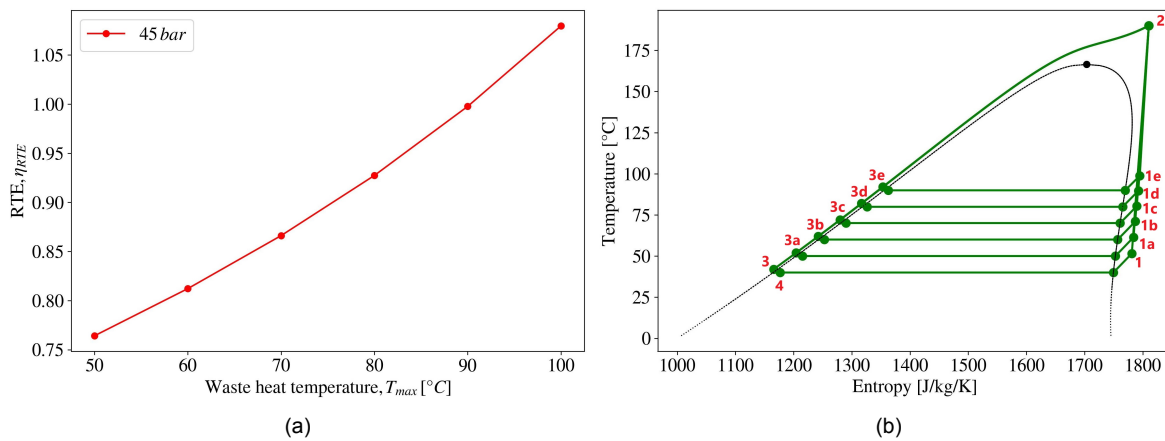


Figure 3.11: (a) Effect of waste heat temperature on the RTE (η_{RTE}) of the CHEST system, (b) T-S representation of varying heat pump evaporator temperature as a result of varying waste heat temperature. The RTE values correspond to a heat pump discharge pressure of 45 bar.

Figure 3.11a exhibits the effect of waste heat temperature on the performance of the CHEST system, while Figure 3.11b depicts the variation in T-S configuration due to change in waste heat temperature. A given waste heat temperature decides the evaporator temperature based on the pinch provided, which is required for continuous heat transfer between the source stream and the working fluid.

As can be observed from Figure 3.11a, the availability of waste heat at higher temperatures improves the performance of the system. This can be explained using the fact that the COP of a heat pump is inversely proportional to the temperature lift backed by Equation (3.3). Lower the temperature lift, higher is the COP (Figure 2.13). As can be seen from Figure 3.11b, an increase in waste heat temperature and thus an increase in evaporator temperature, the heat delivered to energy storage reduces ($2-3e < 2-3d$, $2-3c$ etc). Although energy storage reduces with increasing waste heat temperature, the performance increases, which points out the fact that the increasing waste heat temperature reduces the compressor power more significantly than energy storage.

3.5. Case-I: CHEST with High Temperature Latent Storage

This case will look upon a sub-critical CHEST system with latent heat storage as a hot TES medium while a sensible storage medium used to store the remaining heat available. The scenario is depicted in the process flow diagram as shown in Figure 3.12.

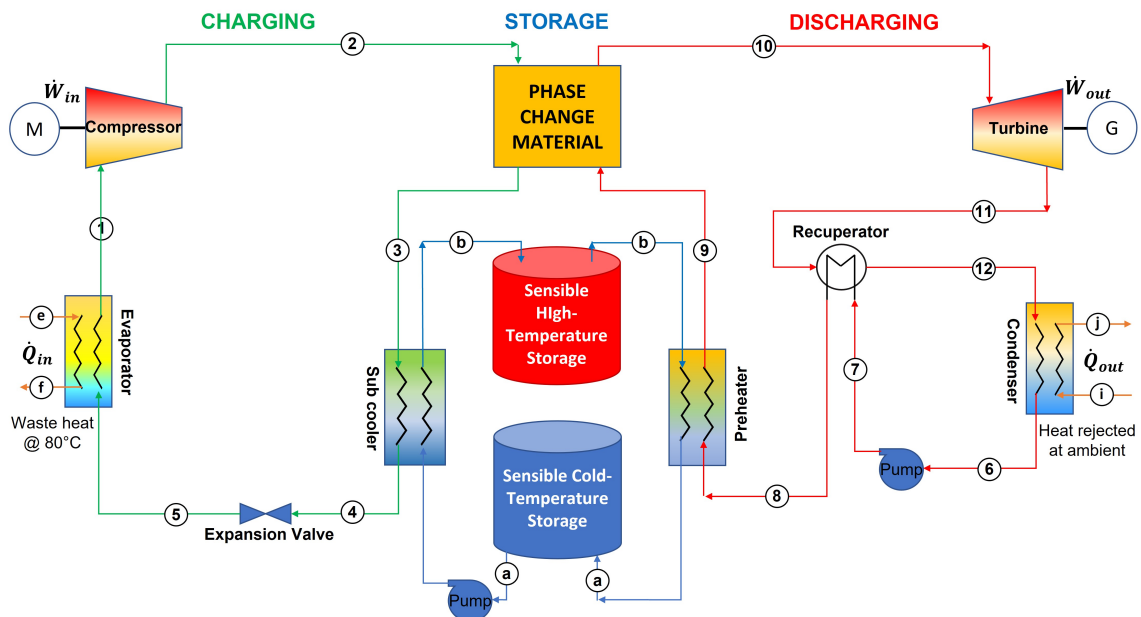


Figure 3.12: Process flow diagram of CHEST system with a combination of latent and sensible heat storage.

The design configuration of the CHEST system shown in Figure 3.12 is similar to the one discussed in the literature case-I (Figure 2.14). The key difference being the working fluid and storage medium used. In this case, R1233zD(E) is used as the primary working fluid, and sunflower oil is used as the sensible storage medium while a hypothetical PCM, as mentioned in earlier sections, is used as the latent storage medium.

Heat balancing of charging and discharging cycles

Presence of multiple storages (latent + sensible) may lead to uneven charging and discharging of the CHEST system. In order to counter this imbalance, ratio of latent heat to sensible heat is kept constant during charging and discharging cycle. The heat ratio equivalence relation is provided as follows:

$$\left| \frac{Q_{latent}}{Q_{sensible}} \right|_{charging} = \left| \frac{Q_{latent}}{Q_{sensible}} \right|_{dis-charging} \quad (3.14)$$

The constant heat ratio ensures both mass and energy balance of sensible heat storage.

3.5.1. Input parameters

The various inputs required to build a thermodynamic design, presented in this case, are listed in Table 3.4.

As mentioned in the previous section, a hypothetical PCM is considered with a melting temperature $T_m = 150^\circ\text{C}$. This value is sufficiently below the critical temperature of R1233zD(E) ($T_{cr} = 165^\circ\text{C}$). This is necessary in order to maximise the use of latent heat of condensation of the working fluid in the heat pump for the storage.

A pinch of $2K$ is fixed between the latent storage and the working fluid of heat pump and heat engine. This further defines the condensation temperature in heat pump condenser equivalent to the sum of

Fixed Input Parameters			
Waste heat input	\dot{Q}_{in}	1	MW _{th}
Waste heat temperature	T_e	80	°C
Evaporator temperature of heat pump	T_5	70	°C
Condensation temperature of heat pump	T_3	152	°C
Condensation temperature of heat engine	T_6	20	°C
Degree of superheat, ΔT_{sup}	$T_1 - T_5$	5	K
Melting temperature of latent storage medium	T_m	150	°C
Maximum sensible storage temperature	T_b	150	°C
Minimum storage temperature	T_a	60	°C
Compressor efficiency	$\eta_{is,comp}$	80	%
Turbine efficiency	$\eta_{is,turb}$	88	%
Pump efficiency	$\eta_{is,pump}$	80	%
Pinch across each heat exchanger	ΔT_{pinch}	2	K
Charging-discharging duration	t_{ch}, t_{dch}	8	hrs

Table 3.4: Input parameters for the latent storage case shown in Figure 3.12.

storage temperature and minimum pinch. Further same pinch is set between sensible storage medium and the heat pump working fluid. This leads to fixing the maximum sensible storage temperature, $T_b = 150^\circ\text{C}$. Moreover, the minimum sensible storage temperature is fixed at $T_a = 60^\circ\text{C}$ which needs to be at sufficiently high temperature as compared to the heat engine sink temperature. Due to the curvature of the isobar with red contour line, as shown in Figure 3.4, the pinch lies somewhere in between the sensible temperature profile. So, a sufficiently high, cold side storage temperature will ensure heat transfer above pinch in the sensible heat exchange zone.

The waste heat is considered to be available at 80°C . Assuming a minimum approach temperature of 2K , the evaporator temperature is set to 70°C , with a degree of superheat (ΔT_{sup}) equal to 5K within the evaporator. This is done to avoid using an additional component for providing high degree of superheating before the inlet of the compressor. Moreover, ΔT_{sup} is provided to ensure that the compression of working fluid doesn't occur in the two-phase region.

The condensation temperature of heat engine cycle (T_6) is kept at 20°C to allow for heat exchange with the ambient. This value shall be kept as low as possible to have a higher degree of expansion from the turbine and thereby generate more power. In this case, heat is being rejected to the ambient and thus it poses a lower limit for the condensation temperature. Finally, for the isentropic efficiencies of the turbomachines, the values ($\eta_{is,comp} = 0.8$, $\eta_{is,pump} = 0.8$, $\eta_{is,turb} = 0.88$) have been taken based on the state of the art for a similar CHEST system [49].

3.5.2. Results

Based on the input parameters given in Table 3.4, the Temperature-Entropy (T-S) and Heat duty-Temperature (Q-T) curves have been modelled as shown in Figure 3.13, and 3.14 respectively.

Temperature-Entropy (T-S) diagram

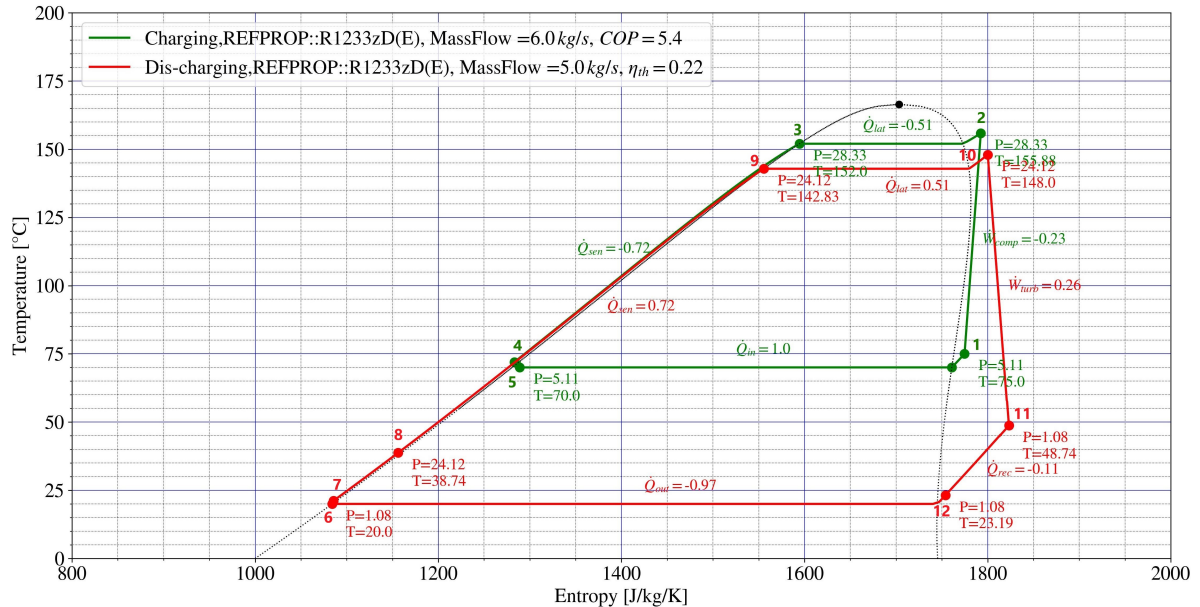


Figure 3.13: T-S plot for the given input conditions corresponding to the PFD shown in Figure 3.12

Heat load-Temperature (Q-T) diagram

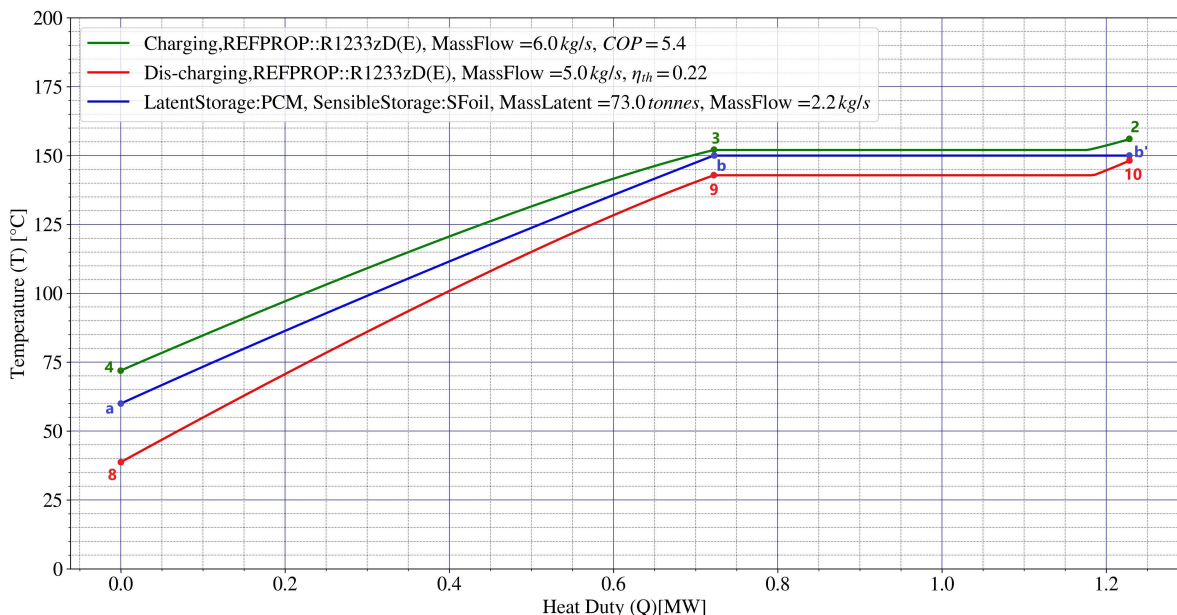


Figure 3.14: Q-T plot representing the total heat exchange between heat pump, storage and heat engine.

In Figure 3.13, the charging or heat pump cycle is outlined in green while discharging or heat engine cycle in red color. Both the cycles thermally balance each other completely as the heat exchange

across sensible storage and latent storage is same. This results out to a same charging and discharging duration.

The Q-T diagram shown in figure 3.14 reflects the total heat exchange between the charging, storage and discharging cycles. During charging cycle, the heat is first stored in the latent storage (2–3 to $b-b'$) until R1233zD reaches saturated liquid condition (3) and further, the heat released during sub-cooling (3–4) is sensibly stored in the sunflower oil ($a-b$). During discharging, R1233zD is preheated (8–9) using the heat from sensible storage tank to saturated liquid condition (9) and further evaporated to superheated condition (10) using the latent heat from the energy stored in PCM. As can be observed, a minimum pinch appears between 3– b in the charging cycle while between 10– b' in the discharging cycle.

The final operating and performance parameters of the CHEST cycle are included in Figure 3.15 and Table 3.5. A high heat pump COP is achieved due to a lower temperature lift (1–2) and simultaneously a high thermal efficiency due to expansion through larger temperature levels (10–11). This resulted in a thermal round trip efficiency $\eta_{RTE,th}$ of $\sim 118\%$.

These results are based on the choice of a hypothetical PCM used for latent storage, which requires a mass of ~ 73 tonnes to store an energy equal to $4.1 MW_{th}$ for a period of 8 hrs.

Output operating conditions

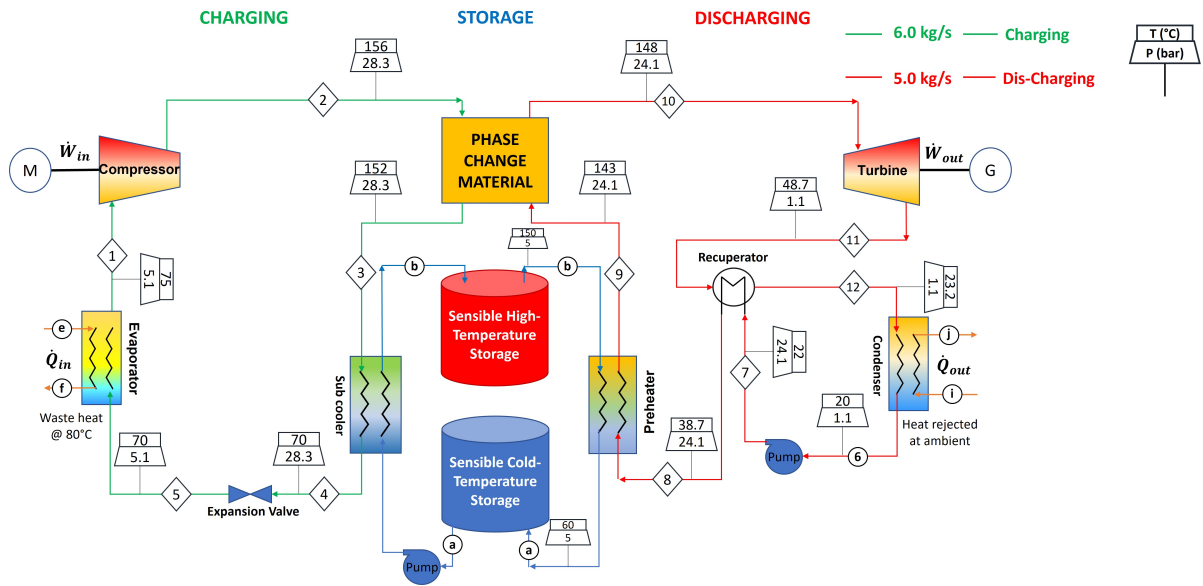


Figure 3.15: Output process flow diagram of CHEST system with a combination of latent and sensible heat storage.

Output Quantities			
Mass flow R1233zD(E) heat pump	\dot{m}_{hp}	6.0	kg/s
Mass flow R1233zD(E) heat engine	\dot{m}_{he}	5.0	kg/s
Mass flow SF oil storage	\dot{m}_{stor}	2.2	kg/s
Mass of PCM required	$m_{lat, stor}$	73	tonnes
Performance of heat pump	COP	540	%
Thermal efficiency of heat engine	η_{th}	22	%
Compressor work input	\dot{W}_{in}	0.23	MW
Turbine work output	\dot{W}_{out}	0.26	MW
Latent storage heat load	\dot{Q}_{lat}	0.51	MW_{th}
Sensible storage heat load	\dot{Q}_{sen}	0.72	MW_{th}
Recuperator heat load	\dot{Q}_{rec}	0.11	MW_{th}
Heat engine condenser duty	\dot{Q}_{out}	0.97	MW_{th}
Latent energy storage capacity	E_{lat}	4.1	MWh
Sensible energy storage capacity	E_{sen}	5.76	MWh
Latent heat storage size	V_{lat}	38	m^3
Sensible heat storage size	V_{sen}	75	m^3
Latent heat storage energy density	U_{lat}	0.11	MWh/m^3
Sensible heat storage energy density	U_{sen}	0.07	MWh/m^3
Round trip efficiency	η_{RTE}	118	%

Table 3.5: Operating conditions for the design configuration shown in Figure 3.12.

3.6. Case-II: CHEST with High Temperature Sensible Storage

In this case, the heat pump is considered to operate in a trans-critical mode, while the heat engine in a sub-critical mode. This is done to facilitate the use of a single sensible storage with a dual storage tank system, instead of multiple storage mediums or reservoirs. A process flow diagram exhibiting the scenario is shown in Figure 3.16.

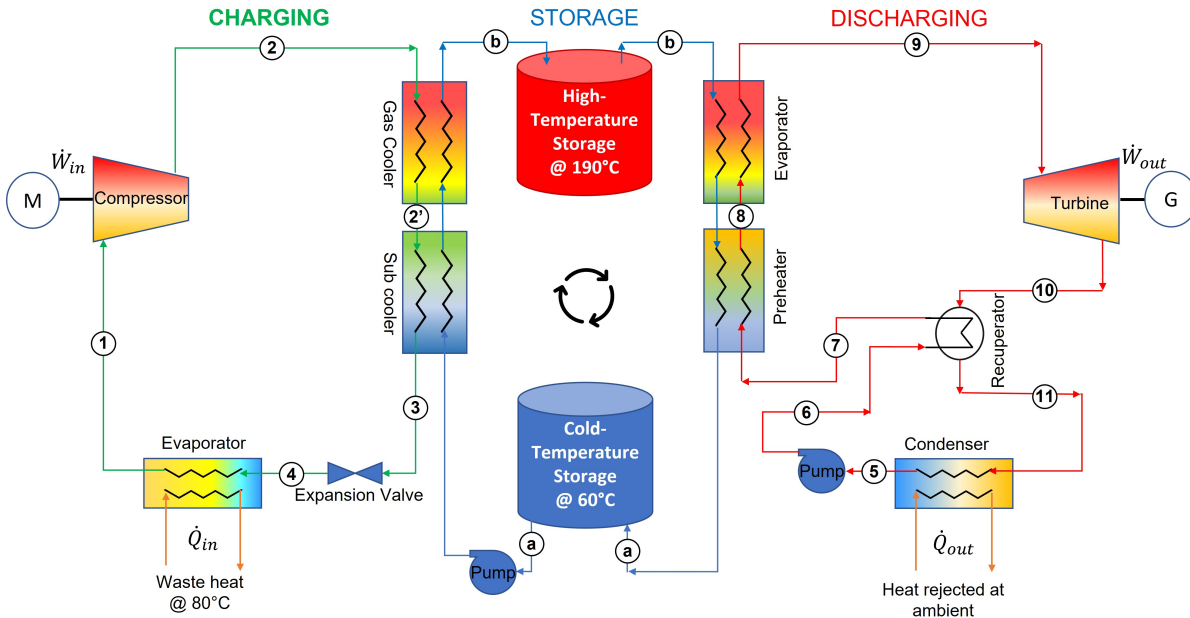


Figure 3.16: Process flow diagram of the base case with single sensible heat storage.

The working principle of the process shown in Figure 3.16 remains identical to the one explained earlier. However, the difference arises out of the fact that a sensible storage medium has been used with just two storage tanks i.e. one cold and one hot storage tank. In the charging cycle, the gas cooler is used to cool the supercritical working fluid to a liquid state (2-2'). This is followed by another heat exchanger, termed as sub cooler, which is used to transfer heat between the liquid working fluid and storage medium from (2' to 3). Meanwhile, the heat rejected from the supercritical working fluid is stored in the hot storage tank (a-b). On the other hand, in the discharging cycle, the pumped working fluid is first preheated (6-7) by the hot fluid from the turbine outlet (10) followed by the storage medium in the preheater (7-8). The working fluid further discharges heat from the storage medium to get evaporated and superheated in the evaporator before entering the turbine (9), while the storage medium gets cooled down (b-a) and is stored back in the cold storage tank.

3.6.1. Input Parameters

The various inputs required to build a design, presented in this case, are listed in Table 3.6.

The maximum storage temperature has been chosen to be 190°C . Since sunflower oil has been selected as the storage medium, the maximum storage temperature value has been motivated by the fact that the smoke point of the oil is in the range of $230 - 250^{\circ}\text{C}$ depending upon the grade of the oil [10, 42, 45]. The selected value is a conservative choice with an attempt to always keep the high temperature below the smoke point.

The waste heat is considered to be available at 80°C . Assuming a minimum approach temperature of 2K , the evaporator temperature is set to 70°C , with a degree of superheat of 5K within the evaporator. This is done to avoid using an additional component for providing high degree of superheating before the inlet of the compressor. A maximum cycle pressure of 50 bar has been chosen to allow for a minimum approach temperature of 2K at the inlet of the gas cooler.

Fixed Input Parameters			
Waste heat input	\dot{Q}_{in}	1	MW _{th}
Waste heat temperature	T_e	80	°C
Evaporator temperature of heat pump	T_4	70	°C
Maximum heat pump cycle Pressure	P_2	50	bar
Ambient temperature	$T_{ambient}$	15	°C
Condensation temperature of heat engine	T_5	20	°C
Degree of superheat, (ΔT_{sup})	$T_1 - T_4$	5	K
Maximum storage temperature	T_b	190	°C
Minimum storage temperature	T_a	60	°C
Compressor efficiency	$\eta_{is,comp}$	80	%
Turbine efficiency	$\eta_{is,turb}$	88	%
Pump efficiency	$\eta_{is,pump}$	80	%
Pinch across each heat exchanger	ΔT_{pinch}	2	K
Charging-discharging duration	t_{ch}, t_{dch}	8	hrs

Table 3.6: Input parameters for the base case shown in Figure 3.16.

The condensing temperature of heat engine cycle is kept at 20°C to allow for heat exchange with the ambient. This value shall be kept as low as possible to have a higher degree of expansion from the turbine and thereby generate more power. In this case, heat is being rejected to the ambient and thus it poses a lower limit for the condensation temperature.

A same charging and discharging duration of 8 hrs has been considered. For the isentropic efficiencies of the turbomachines, the values ($\eta_{is,comp} = 0.8, \eta_{is,pump} = 0.8, \eta_{is,turb} = 0.88$) have been taken based on the values motivated from the literature.[49].

3.6.2. Results

Based on the input parameters, the Temperature-Entropy (T-S) and Energy-Temperature (E-T) curves have been modelled as shown in Figure 3.17, and 3.18 respectively.

Temperature-Entropy (T-S) diagram

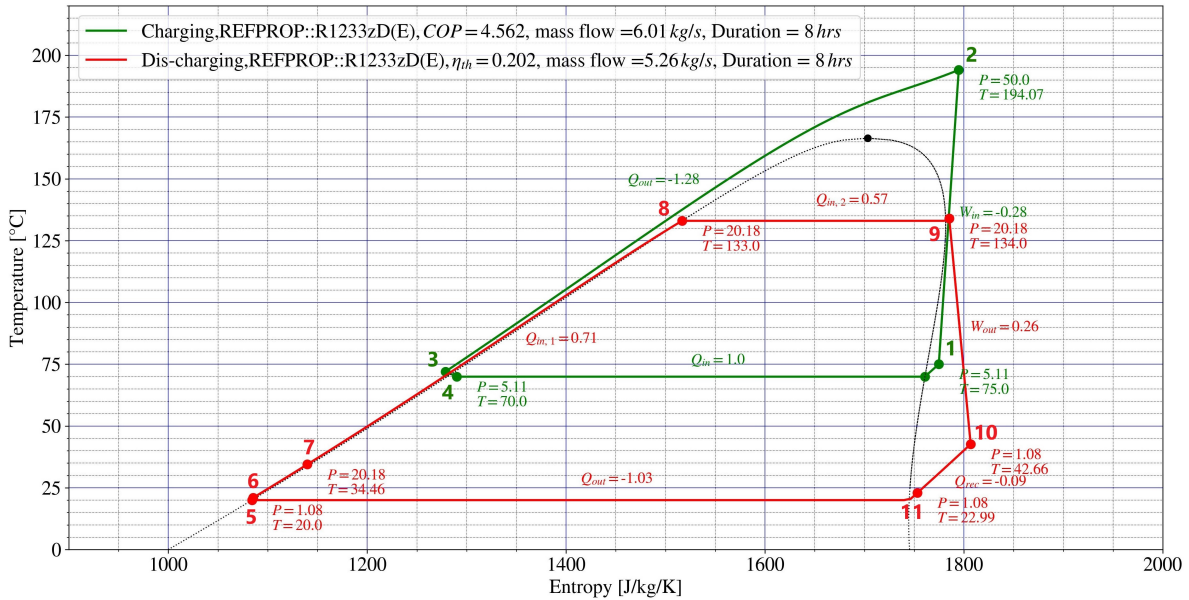


Figure 3.17: T-S plot for the given input conditions corresponding to the PFD shown in Figure 3.16

Energy-Temperature (E-T) diagram

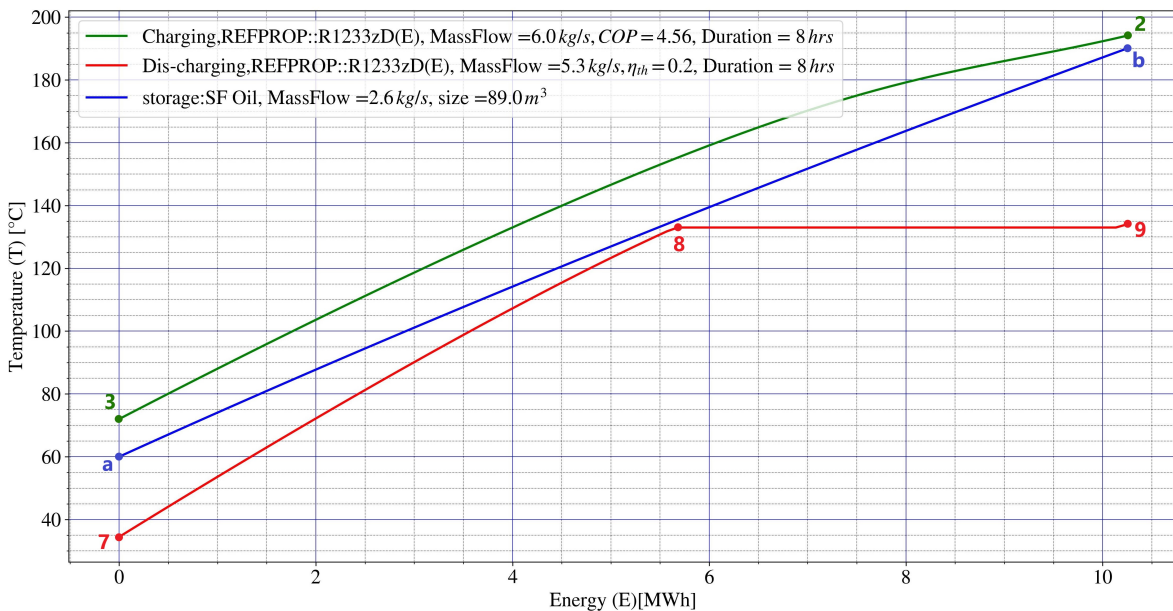


Figure 3.18: E-T plot representing the total energy exchange between heat pump, storage and heat engine.

From the T-S diagram, Figure 3.17, the closed cycle in green color represents the charging or heat pump cycle, while the discharge or Rankine cycle is outlined in red color. The working fluid (R1233zD(E))

is allowed to evaporate and get superheated (4-1) using the waste heat, $Q_{in} = 1 MW$. It is further compressed to supercritical conditions (1-2) with the aid of external electric work W_{in} . The working fluid is then allowed to cool in a gas cooler (2-2'-3) and reject heat to the storage medium (a-b). This can be effectively seen in the E-T diagram shown in Figure 3.18. The blue curve represents the temperature profile of sunflower oil during charging and discharging cycles. During the charging cycle, the heat is sensibly stored in the sunflower oil while heating from 60–190°C (a-b) and the storage cycle is reversed during the discharging phase (b-a).

The heat balance within charging and discharging cycles is subjected to a constant energy transferred from heat pump to storage to heat engine cycle. Since the charging and discharging duration remains same, the amount of heat (thermal) exchanged tends to be equal, i.e. $Q_{out,ch} = Q_{in,1} + Q_{in,2}$, as evident from Figure 3.18.

The corresponding mass flow rates, COP, η_{th} , storage volume have been summarised in Table 3.7.

Output operating conditions

Output Quantities			
Mass flow R1233zD(E) heat pump	\dot{m}_{hp}	6	kg/s
Mass flow R1233zD(E) heat engine	\dot{m}_{he}	5.3	kg/s
Mass flow SF oil storage	\dot{m}_{stor}	2.6	kg/s
Performance of heat pump	COP	456	%
Thermal efficiency of heat engine	η_{th}	20	%
Compressor work input	\dot{W}_{in}	0.28	MW
Turbine work output	\dot{W}_{out}	0.26	MW
Recuperator heat load	\dot{Q}_{rec}	0.1	MW _{th}
Heat engine condenser duty	\dot{Q}_{out}	1.03	MW _{th}
Energy storage capacity	E	10.24	MWh
Storage size	V	89	m ³
Energy storage density	U	0.115	MWh/m ³
Round trip efficiency	η_{RTE}	91	%

Table 3.7: Operating conditions for the design configuration shown in Figure 3.16.

3.6.3. Optimization

The results of the previous section were based on the assumed values of certain cycle input parameters. These values were taken from the desired range, which was based on the sensitivity analysis done in section 3.4. This section will provide an optimised value of all the state points of the charging and discharging cycle for a particular optimization case.

Same heat exchanger for charging and discharging cycles

The operating period for the the heat pump and heat engine cycle considered in this work are different. Using the advantage of this fact, using same components for both the cycles can lead to a significant reduction in overall system costs (CAPEX). This optimised case will only consider using a same heat exchanger between the working fluid (R1233zD(E)) and the storage medium for both the cycles, limited to a part of the total energy exchange. This scenario has been depicted in the process flow diagram below, Figure 3.19.

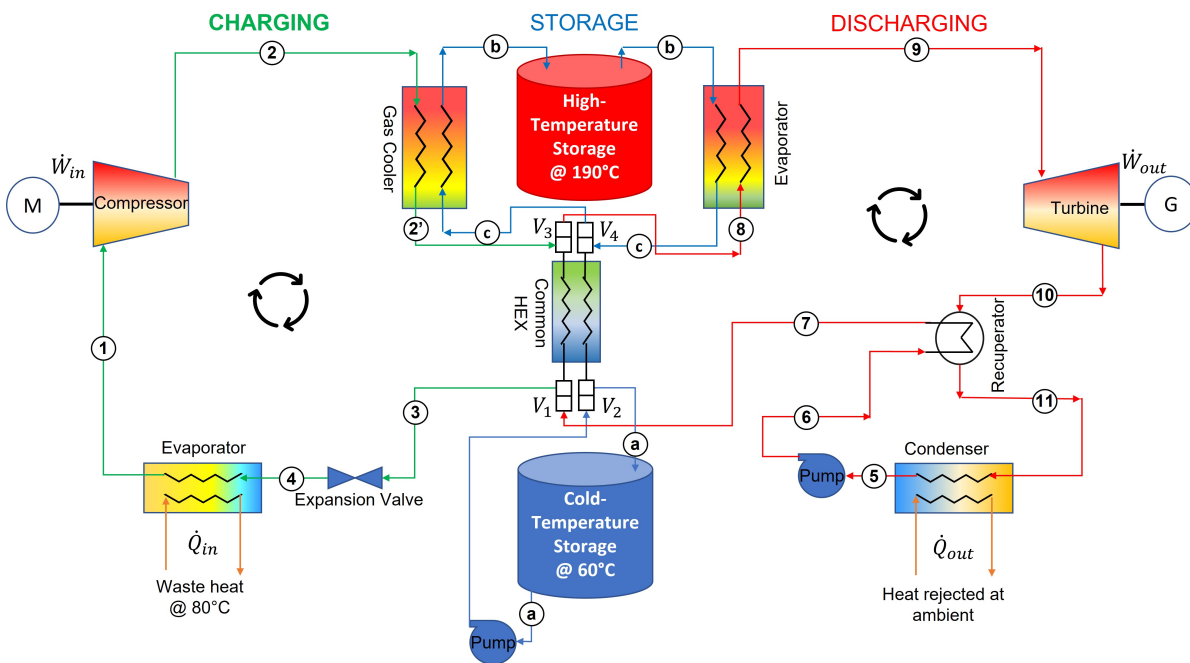


Figure 3.19: Process flow diagram for the optimised case with a common HEX between storage medium and charging-discharging cycles.

The charging and discharging cycles, shown in Figure 3.19, operate similarly to the cycles shown in the non-optimised case in figure 2.17. A key difference is the use of a 'Common HEX' in Figure 3.19, which seems to replace the sub-cooler & preheater in Figure 2.17. So during the charging cycle the working fluid enters the 'Common HEX' in compressible liquid form (2') and rejects heat to the storage medium (a-c), while the direction of the working fluid is reversed during the discharging cycle to absorb heat from the storage medium (c-a) and reach saturated liquid conditions (8). The direction of the flow of working fluid and the storage medium through the 'Common HEX' is controlled and operated by valves V_1 , & V_2 on the lower temperature side and V_3 , & V_4 on the higher temperature side. During the charging cycle, valve V_1 and V_3 are open to streams 3 and 2' respectively, while valve V_2 and V_4 are open to storage medium flowing from cold storage tank to hot storage tank. Conversely, during the discharging cycle, valve V_1 and V_3 are open to streams 7 and 8 respectively, while valve V_2 and V_4 are open to storage medium flowing from hot storage tank to cold storage tank.

The 'Common HEX' has been preferably placed between the gas cooler of the charging cycle and the recuperator of the discharging cycle. As can be observed from Figure 3.18, the temperature profiles of charging, discharging, and storage medium are quite linear, until the working fluid enters the evaporator in the discharging cycle. Moreover, the working fluids in this region are in same liquid

state and share similar thermophysical properties. The solution to this optimization requires matching the heat exchanger area (A_{HEX}) for both the charging and discharging case. The area can be calculated using the overall heat transfer equation as follows:

$$A_{HEX} = \left(\frac{\dot{Q}_{HEX}}{U_0 \cdot LMTD} \right)_{ch} = \left(\frac{\dot{Q}_{HEX}}{U_0 \cdot LMTD} \right)_{dch}, \quad (3.15)$$

where, \dot{Q}_{HEX} , and $LMTD$ represent the heat load and the log mean temperature difference of the heat exchanger and are dependent on the process streams inlet and exit state points. The term ' U ' represent the overall heat transfer coefficient and is a component specific property, which also depends on other factors such as nature of heat transfer, thermal properties of the HEX material across which heat transfer takes place, geometry, etc.

In the present work, the 'Common HEX' inlet & outlet state points have been optimized considering same " UA " value for charging and discharging cycle. Since, operating conditions, nature of heat transfer, thermophysical properties of working fluid in charging and discharging cycle in the specified region are similar, the overall heat transfer coefficient results to be similar for both the cycles. This further leads to a similar heat exchange area for both the cycles and the geometry giving the higher area could be selected. So Equation (3.15) can be re-written as:

$$(U_0A)_{HEX} = \left(\frac{\dot{Q}_{HEX}}{LMTD} \right)_{ch} = \left(\frac{\dot{Q}_{HEX}}{LMTD} \right)_{dch}. \quad (3.16)$$

As mentioned previously, the heat balance of the CHEST system, in this work, is subjected to constant energy transfer from heat pump to TES to heat engine. In an attempt to modulate the state point parameters to achieve a constant " U_0A " value for both the cycles, the heat load for both the cycles may vary, which is mainly dependent on charging (t_{ch}) and discharging (t_{dch}) times through the following relation:

$$E_{stor} = \dot{Q}_{ch} \cdot t_{ch} = \dot{Q}_{dch} \cdot t_{dch}. \quad (3.17)$$

A different charging and discharging time for the storage medium can be controlled by varying the mass flow rate of storage medium (\dot{m}_s) for both the cycles, such that volume flow remains constant:

$$\dot{m}_{s,ch} \cdot t_{ch} = \dot{m}_{s,dch} \cdot t_{dch}. \quad (3.18)$$

A preliminary design of this HEX has been done in Chapter 4.

Optimizing scheme

The optimization procedure followed in this work is limited to evaluating the cycle state parameters and performance related parameters and thus, no optimization on sizing of the components have been performed in this work. A single-objective and multi-variable optimization has been carried out on the steady-state model of the CHEST system discussed in Figure 3.19. It is based on the Sequential Least Squares Programming (SLSQP) algorithm, which performs the user defined action on the objective function in a sequential manner, i.e. begins from a fixed point (input from the user) and performs the mass and energy balance across each component in the direction of flow while being subjected to certain required boundary conditions in the form of constraints and bounds (upper and lower limit).

The optimizer is characterised mainly by an objective function, $f(x)$, subject to a set of constraints (linear or non-linear) which defines the conditions to be satisfied to reach the desired outcome. Further, it is bounded with the upper and lower limits of the decision variables. A general constrained optimization problem can be formulated as follows:

$$\begin{aligned} & \min_x \left(f(x) + \sum_i Pen_i(x) \right) \\ & \text{subject to: } b_j \leq g_j(x) \leq c_j \quad \forall_j = 1, \dots, n_{constr} \\ & \quad \quad \quad l_b \leq x \leq u_b \\ & \quad \quad \quad x_k \in \mathbb{R} \quad x_l \in \mathbb{Z} \end{aligned} \quad (3.19)$$

where, x is the set of decision variables, for which the optimization problem will minimize the objective function $f(x)$. A set of constraints $g_j(x)$ have been applied, where 'j' goes from 1 to number of constraints. The choice of decision variables ' x ' can be either real numbers (x_k) or integers (x_l), however within the lower (l_b) and upper (u_b) bound. Moreover, penalties $Pen(x)$ could be introduced along with the objective function, to convert the constrained problem into an un-constrained problem. A penalty proportional to the extent of violation of the constraints is added to the objective function in order to guide the optimizer towards more feasible solutions.

In this work, no such use of penalties have been made, instead, constraints have been applied to direct the feasibility of the optimized solution. The inverse of round trip efficiency (RTE) of the system has been chosen as the objective function which needs to be minimised to get the maximum RTE. Further, the maximum cycle temperature and pressure values for both the cycles along with the discharge duration have been taken as decision variables. The constraints have been applied to the following: (i) the extent of superheating before compression in the heat pump cycle, (ii) pinch between the storage medium and charging-discharging cycles, (iii) discharge duration, and (iv) the vapor quality of working fluid being compressed or expanded.

Table 3.8 enumerates all the fixed and variable quantities given as an input to the thermodynamic model to obtain the optimized solution.

Input Parameters				
Waste heat input	\dot{Q}_{in}	1	MW _{th}	Fixed
Waste heat temperature	T_e	80	°C	Fixed
Evaporator temperature of heat pump	T_4	70	°C	Fixed
Maximum heat pump cycle temperature	T_2	190 - 200	°C	Variable
Maximum heat pump cycle Pressure	P_2	40-50	bar	Variable
Maximum heat engine cycle temperature	T_9	120 - 170	°C	Variable
Maximum heat engine evaporator temperature	T_8	120 - 165	°C	Variable
Ambient temperature	$T_{ambient}$	15	°C	Fixed
Condensation temperature of heat engine	T_5	20	°C	Fixed
Degree of superheat, (ΔT_{sup})	$T_1 - T_4$	5-10	K	Variable
Maximum storage temperature	T_b	190	°C	Fixed
Minimum storage temperature	T_a	60	°C	Fixed
Compressor efficiency	$\eta_{is,comp}$	80	%	Fixed
Turbine efficiency	$\eta_{is,turb}$	88	%	Fixed
Pump efficiency	$\eta_{is,pump}$	80	%	Fixed
Pinch across each heat exchanger	ΔT_{pinch}	2	K	Fixed
Charging duration	t_{ch}	8	hrs	Fixed

Table 3.8: Fixed and variable input parameters for the optimized case shown in Figure 3.19.

3.6.4. Results

Based on the optimized decision variables given in Table 3.9, the Temperature-Entropy (T-S) and Energy-Temperature (E-T) plot for the optimized system have been modelled and exhibited in Figure 3.20, and 3.21 respectively.

Temperature-Entropy (T-S) diagram

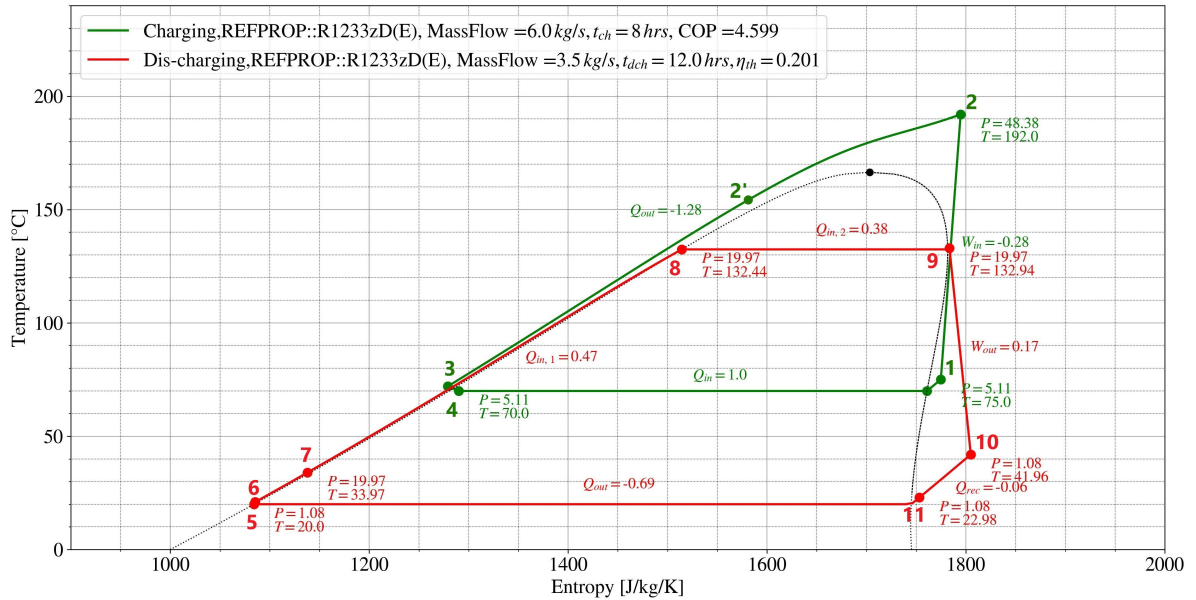


Figure 3.20: T-S plot for the optimized conditions corresponding to the PFD shown in Figure 3.19.

Energy-Temperature (E-T) diagram

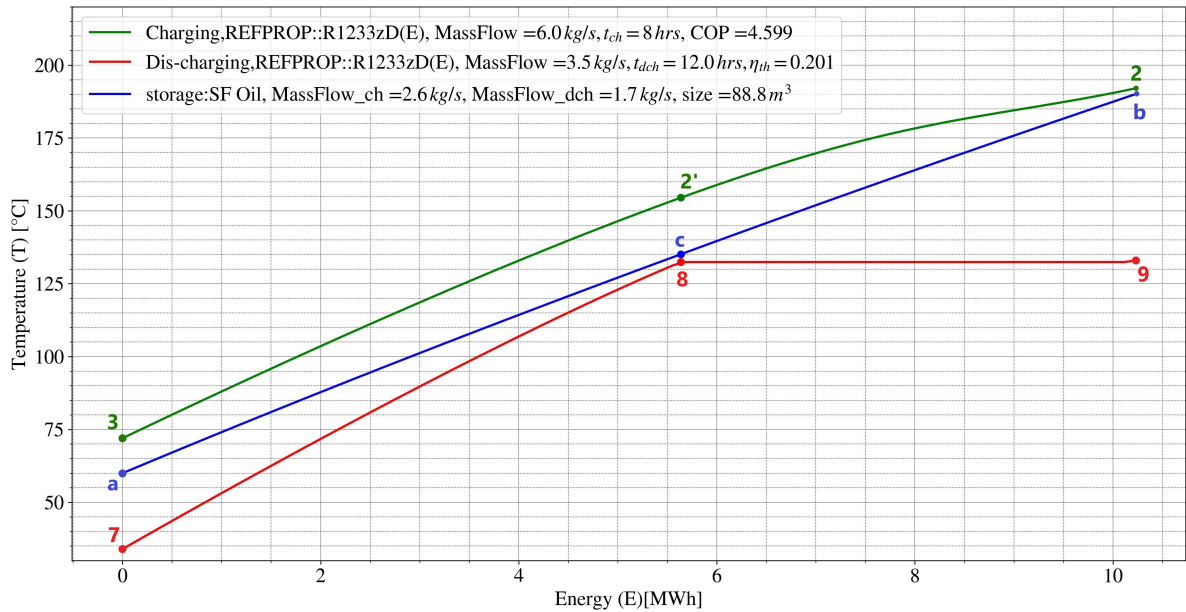


Figure 3.21: E-T plot depicting the energy transfer between heat pump, storage and heat engine cycles.

Optimized operating conditions

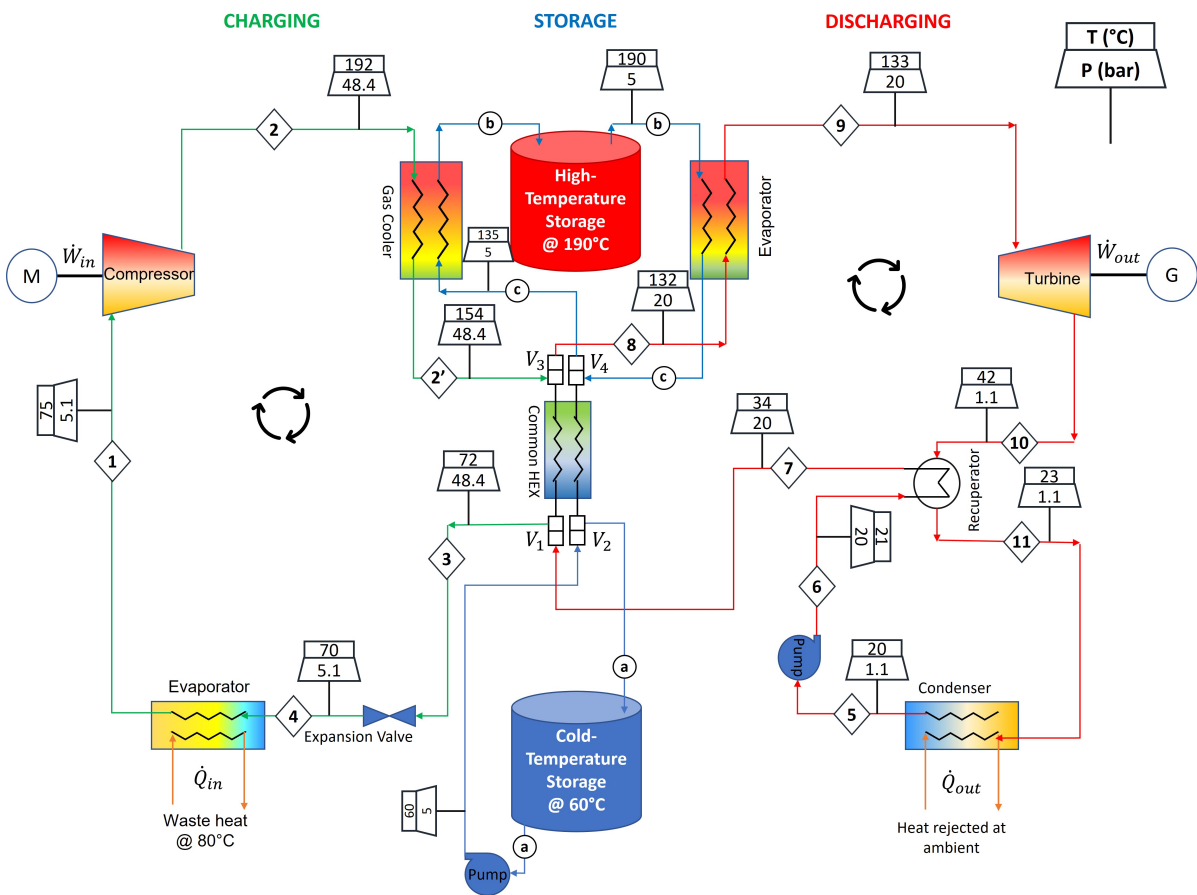


Figure 3.22: Output Process flow diagram for the optimised case with a common HEX between storage medium and charging-discharging cycle.

Cycle state points	Temperature (°C)	Pressure (bar)
1	75	5.1
2	192	48.4
2'	154.5	48.4
3	72	48.4
4	70	5.1
5	20	1.1
6	21	20
7	34.0	20
8	132.4	20
9	133	20
10	42	1.1
11	23	1.1
c	135.1	5.0

Table 3.9: Heat pump and heat engine cycle optimized state points based on the input parameters given in Table 3.8 for the design configuration shown in Figure 3.19.

Output Quantities			
Mass flow R1233zD(E) heat pump	\dot{m}_{hp}	6	kg/s
Mass flow R1233zD(E) heat engine	\dot{m}_{he}	3.5	kg/s
Mass flow SF oil storage during charging	$\dot{m}_{stor,ch}$	2.6	kg/s
Mass flow SF oil storage during discharging	$\dot{m}_{stor,dch}$	1.7	kg/s
Performance of heat pump	COP	460	%
Thermal efficiency of heat engine	η_{th}	20	%
Compressor work input	\dot{W}_{in}	0.28	MW
Turbine work output	\dot{W}_{out}	0.17	MW
Common HEX duty during charging	$\dot{Q}_{2'-3}$	0.7	MW_{th}
Common HEX duty during discharging	\dot{Q}_{8-7}	0.47	MW_{th}
Recuperator heat load	\dot{Q}_{rec}	0.06	MW_{th}
Heat engine condenser duty	\dot{Q}_{out}	0.7	MW_{th}
Discharge duration	t_{dch}	12.0	hrs
Energy storage capacity	E	10.24	MWh
Storage size	V	89	m^3
Energy storage density	U	0.115	MWh/m^3
Round trip efficiency	η_{RTE}	92	%

Table 3.10: Optimized operating conditions for the design configuration shown in Figure 3.19.

Discussion

From Figure 3.20, the optimization has resulted in a better COP of heat pump, eventually to a higher RTE of the system as compared to the non-optimised case, Figure 3.17, by $\sim 1\%$. Although the increase in RTE isn't significant, using a common HEX reduces a component from the system, which is a huge benefit in lowering the total CAPEX of the system. Moreover, employing a same HEX between charging, storage and discharging cycles ($2' - 3, c - a, 8 - 7$) has led to a different heat exchange duty of the common HEX for charging and discharging cycles. This results into different charging and discharging times for the system as can be explained by Equation (3.17). This system will be a good solution for storing energy during the day time ($\sim 8 hrs$) and further having sufficient time during the night ($\sim 12 hrs$) to get discharged and generate power.

3.7. Design Comparison

In the previous sections two main design configurations were exhibited, namely, CHEST with high temperature latent storage and CHEST with single sensible storage, as shown in Figure 3.12 and 3.19 respectively. The key differences in the design and performance of the two configurations has been listed in Table 3.11.

CHEST	CASE-I: CHEST with High Temperature Latent Storage	CASE-II: CHEST with Full Sensible Storage
Working Fluid	R1233zD	R1233zD
Operating Phase	Heat Pump: Sub-critical mode Heat Engine: Sub-critical mode	Heat Pump: Trans-critical mode Heat Engine: Sub-critical mode
Coefficient of Performance	5.4	4.6
Heat Engine thermal efficiency	0.22	0.2
Storage Medium	Latent storage: Hypothetical PCM Sensible storage: Sunflower oil	Sensible storage: Sunflower oil
Storage Temperature	Latent storage: $T_m = 150^\circ\text{C}$ Sensible storage: $T_{max} = 150^\circ\text{C}$ $T_{min} = 60^\circ\text{C}$	$T_{max} = 190^\circ\text{C}$ $T_{min} = 60^\circ\text{C}$
Storage Volume	Latent storage: 38 m^3 Sensible storage: 75 m^3	89 m^3
Total Energy Storage Density*	Latent storage: 0.11 MWh/m^3 Sensible storage: 0.07 MWh/m^3	0.115 MWh/m^3
Round Trip Efficiency	1.18	0.92
number of heat exchangers	7	6

Table 3.11: Comparison of design configuration and performance parameters of the CHEST system corresponding to Figure 3.12 & 3.19.

* Total energy storage density corresponds to a charging duration of 8 hrs.

From Table 3.11, for the same amount of waste heat available, the total energy storage capacity obtained in Case-II is more than that obtained in Case-I, however, the difference is meagre. However, the storage volume obtained with single sensible heat storage is significantly less than the combined storage volume of CASE-1. The low storage volume results in higher energy density of single sensible heat storage configuration.

In terms of the thermodynamic performance, Case-I is much efficient than Case-II with RTE $\eta_{RTE,th}$ more than 25%. Nevertheless, use of single sensible heat storage has allowed to reduce the number of cycle components by using same HEX for charging and discharging cycles in the sensible heat transfer region. This has the potential to considerably reduce the CAPEX of the plant.

As already mentioned, the latent storage assumed is a hypothetical PCM. The less availability and high operational costs of PCM along with complex heat transfer modelling makes PCM a weaker choice as compared to using sunflower oil. Moreover, PCM needs to be exposed to same pressure as that of working fluid. On the other hand, oil as the TES medium can be stored at ambient pressure conditions. In addition, the high availability and low cost of sunflower oil could compensate more than the reduction of the round trip efficiency. As a result, CHEST with fully sensible storage, and sunflower oil as the energy storage medium will be used to carry out the further analysis of the case study described in the following chapter.

4

Equipment Design

4.1. Introduction

In this chapter, the thermodynamic model developed in Chapter 3 for the CHEST system with waste single sensible heat storage is applied in a case study. The main purpose of this chapter is to provide a preliminary design of the heat exchangers and a basic sizing of the turbomachinery used in the present CHEST system.

4.2. CHEST Unit Coupled With Solar Powered Alkaline Electrolyzer

This section provides a result of the thermodynamic analysis of a scaled-up CHEST system, which is combined with a solar-based alkaline electrolyzer as shown in the plant layout in the Figure 4.1.

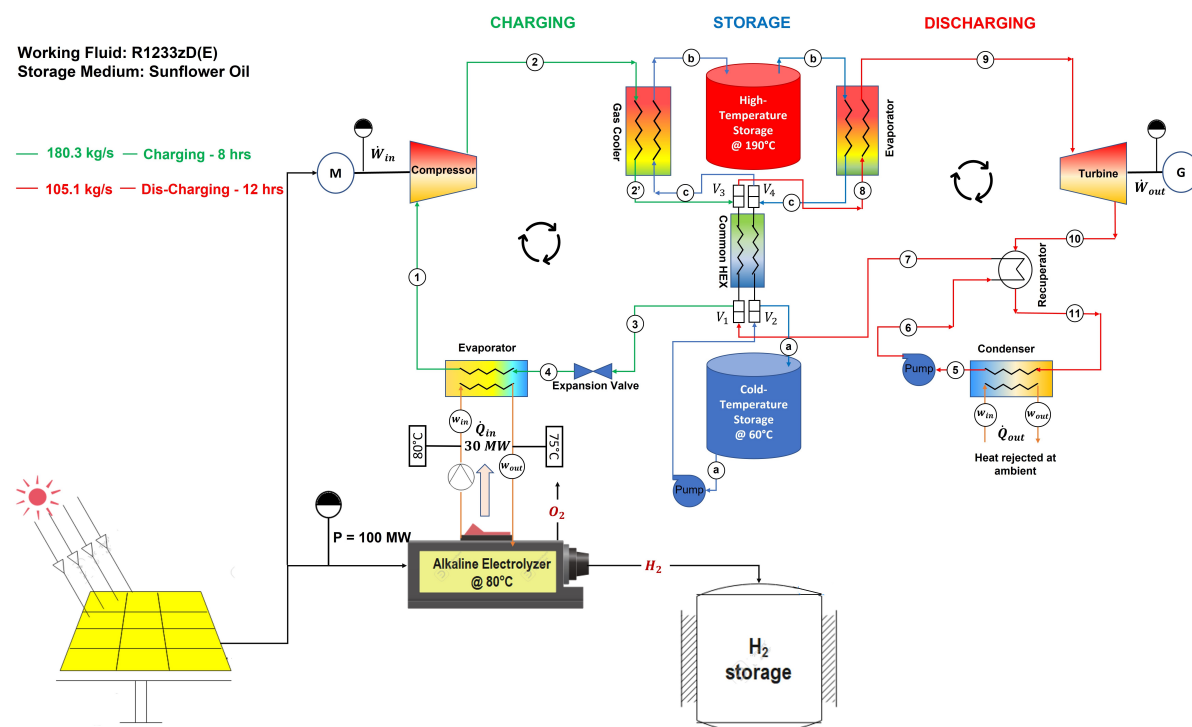


Figure 4.1: Plant layout of the CHEST system coupled with solar powered alkaline electrolyzer unit.

From Figure 4.1, a solar field is used to power a 100 MW alkaline electrolyser, which is operated to produce green hydrogen (H_2). This leads to storing electricity in the form of chemical energy possessed by H_2 . Water electrolysis is a non-spontaneous electro-chemical reaction based on standard redox reactions. Ideally, an energy equivalent to the change in Gibb's free energy of the electro-chemical cell reaction needs to be provided to make the electrolysis process occur. However, an additional energy is required to overcome the losses and resistance in the electro-chemical cell, which is termed as "overpotential" and is equivalent to the difference between actual and theoretical cell voltage.

Working of an electrolyser requires an optimum operating temperature of around $80^\circ C$ [50, 55]. Although electrolysis is an endothermic reaction, there is a significant heat generation within the system due to the overpotential applied to the electro-chemical cell. This heat production is equivalent to around 30% of the power input to the electrolyser [50, 55], which poses an adverse effect on the thermal efficiency of the electrolysis process. As such, a heat recovery system is required to cool down the electrolyser and maintain its optimum working temperature of $80^\circ C$.

From Figure 4.1, a CHEST system is integrated with the alkaline electrolyser unit. The waste heat from the electrolyser ($\sim 30MW_{th}$) is fed to the heat pump. The heat pump uses an electricity input from the solar field to drive the compressor and upgrade the waste heat. The high grade heat is further stored in a TES medium during the charging operation i.e. until the electrolyser operates and hence only during the day time. Further during the night, the heat stored in TES is discharged back to operate an ORC and produce electricity, which could potentially be used to help maintain the plant auxiliaries operation.

Water has been used as the primary fluid for the cooling of electrolyser and the condenser of the heat engine. Since electrolyser needs to be maintained at $80^\circ C$, the outlet of cooling water is too considered around $\sim 78 - 80^\circ C$. This is the temperature of the waste heat at which it is fed to the evaporator of the heat pump. Further, a $8K$ temperature change is considered in the water stream to maintain the necessary pinch ($2K$) with the heat pump evaporator. Similarly, on the heat engine condenser side, the working fluid needs to be condensed at $20^\circ C$. The water inlet is at $10^\circ C$ and a temperature rise of $10K$ is assumed for the water stream to cool the condenser. The input to the thermodynamic model for the present case study is given in Table 4.1.

Fixed Input Parameters			
Waste heat input	\dot{Q}_{in}	30	MW_{th}
Waste heat temperature	$T_{w,in, hp}$	80	$^\circ C$
Evaporator temperature of heat pump	T_4	70	$^\circ C$
Maximum heat pump cycle temperature	T_2	192	$^\circ C$
Maximum heat pump cycle Pressure	P_2	48.4	bar
Maximum heat engine cycle temperature	T_9	133	$^\circ C$
Maximum heat engine evaporator temperature	T_8	132.4	$^\circ C$
Water inlet temperature at HE condenser	$T_{w,in, cond}$	10	$^\circ C$
Condensation temperature of heat engine	T_5	20	$^\circ C$
Degree of superheat, (ΔT_{sup})	$T_1 - T_4$	5	K
Maximum storage temperature	T_b	190	$^\circ C$
Minimum storage temperature	T_a	60	$^\circ C$
Compressor efficiency	$\eta_{is, comp}$	80	%
Turbine efficiency	$\eta_{is, turb}$	88	%
Pump efficiency	$\eta_{is, pump}$	80	%
Pinch across each heat exchanger	ΔT_{pinch}	2	K
Charging duration	t_{ch}	8	hrs

Table 4.1: Input parameters for the plant layout shown in Figure 4.1.

4.2.1. Thermodynamic cycle results for CHEST system

Temperature-Entropy (T-S) diagram

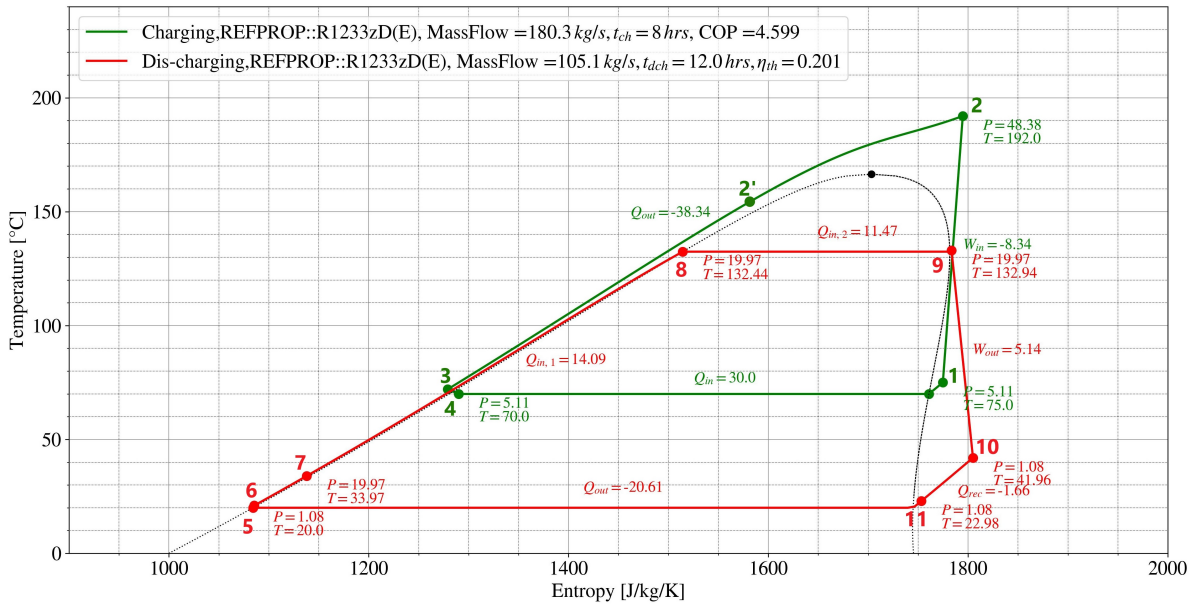


Figure 4.2: T-S plot for the optimized conditions corresponding to the plant layout shown in Figure 4.1.

Energy-Temperature (E-T) diagram

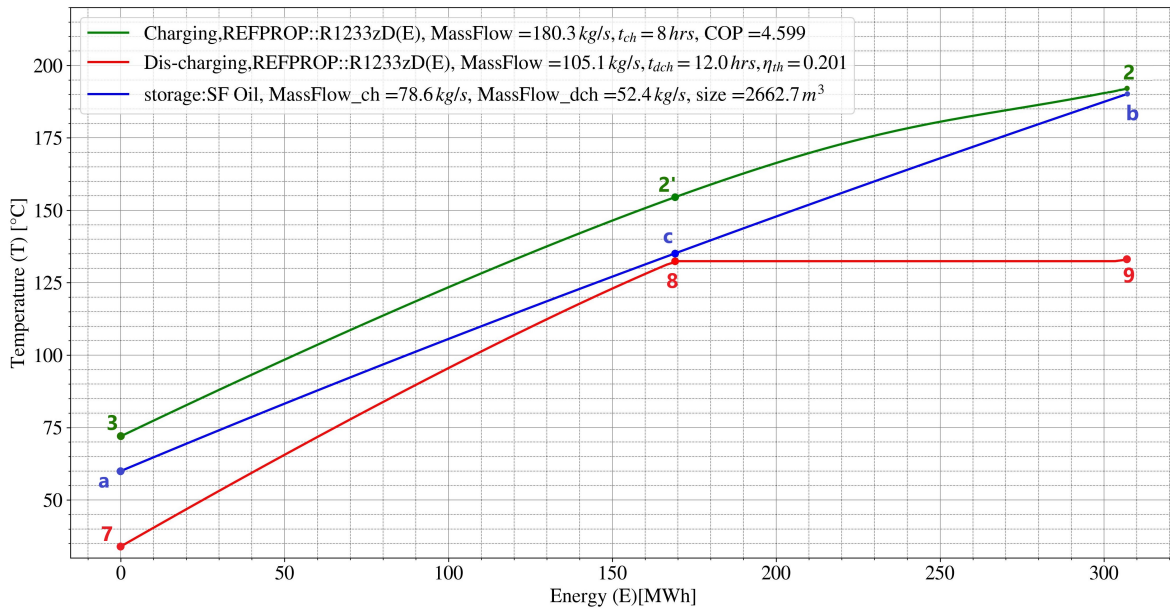
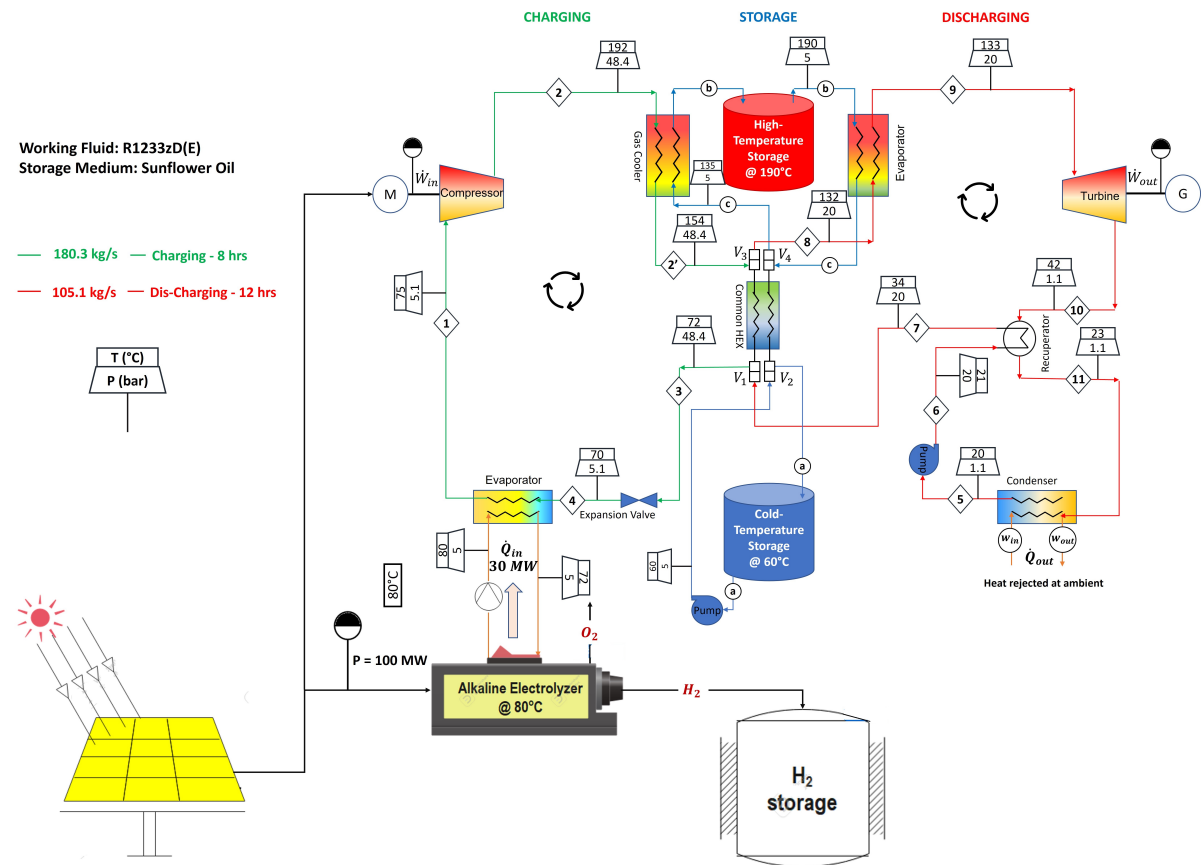


Figure 4.3: E-T plot depicting the energy transfer between heat pump, storage and heat engine cycles.

Operating Conditions



Output Quantities			
Mass flow R1233zD(E) heat pump	\dot{m}_{hp}	180.3	kg/s
Mass flow R1233zD(E) heat engine	\dot{m}_{he}	105.1	kg/s
Mass flow SF oil storage during charging	$\dot{m}_{stor, ch}$	78.6	kg/s
Mass flow SF oil storage during discharging	$\dot{m}_{stor, dch}$	52.4	kg/s
Mass flow water for cooling electrolyser	$\dot{m}_{w, evap}$	895	kg/s
Mass flow water for cooling condenser	$\dot{m}_{w, cond}$	493	kg/s
Performance of heat pump	COP	460	%
Thermal efficiency of heat engine	η_{th}	20.1	%
Compressor work input	\dot{W}_{in}	8.34	MW
Turbine work output	\dot{W}_{out}	5.14	MW
Common HEX duty during charging	$\dot{Q}_{2'-3}$	21.14	MW _{th}
Common HEX duty during discharging	\dot{Q}_{8-7}	14.1	MW _{th}
Recuperator heat load	\dot{Q}_{rec}	1.67	MW _{th}
Heat engine condenser duty	\dot{Q}_{out}	20.6	MW _{th}
Discharge duration	t_{dch}	12.0	hrs
Energy storage capacity	E	306.7	MWh
Storage size	V	2663	m ³
Energy storage density	U	0.115	MWh/m ³
Round trip efficiency	η_{RTE}	92	%

Table 4.2: Optimized operating conditions for the plant layout shown in Figure 4.1.

Figure 4.4 & Table 4.2 provides the operating conditions for the discussed case study in Figure 4.1. All necessary state points, mass flow rates, heat loads and performance values across individual component has been listed out. These values will serve as the input conditions for providing a design of the main components of the CHEST system such as heat exchangers and turbomachines.

4.3. Heat Exchanger Design

Section 2.6.1 discussed about the type and operating conditions of conventional heat exchangers and outlined a general design procedure. This section will deal with providing a preliminary design of the HEXs used in the present case study as shown in Figure 4.1. The various HEXs are: heat pump evaporator, gas cooler, common HEX, heat engine evaporator, recuperator, and a water-cooled condenser. The purpose of having a preliminary design is to get an idea of the overall heat transfer area required for the HEX. Moreover, it is also important to get an estimate of the pressure drop within a HEX, in order to include them within the model at a later stage. confine the pressure drop within the allowable pressure drop limit of the HEX.

The required input operating conditions of the HEX's in heat pump and heat engine are summarised in Table 4.3 and 4.4 respectively, which are used to decide the type of HEX to be selected for the design purposes.

Heat Exchanger		Evaporator		Gas Cooler		Common HEX	
		Hot side	Cold side	Hot side	Cold side	Hot side	Cold side
Fluid		Water	R1233zD	R1233zD	SFOil	R1233zD	SFOil
Temp. Inlet	°C	80	70	192	135.1	154.5	60
Temp. Outlet	°C	72	75	154.5	190	72	135.1
Pressure	bar	5	5.1	48.4	5	48.4	5
Heat Load	MW		30		17.2		21.14
mass flow rate	kg/s	895	180.3	180.3	78.6	180.3	78.6
LMTD	K		5		7.7		12.9

Table 4.3: Input design conditions of heat exchangers in heat pump cycle.

Heat Exchanger		Common HEX		Evaporator		Recuperator		Condenser	
		Hot side	Cold side	Hot side	Cold side	Hot side	Cold side	Hot side	Cold side
Fluid		SFOil	R1233zD	SFOil	R1233zD	R1233zD (gas)	R1233zD (liq)	R1233zD	Water
Temp. Inlet	°C	135.1	34	190	132.4	42	21	23	10
Temp. Outlet	°C	60	132.4	135.1	133	23	34	20	20
Pressure	bar	5	20	5	20	1.1	20	1.1	2
Heat Load	MW		14.1		11.47		1.66		20.61
mass flow rate	kg/s	52.4	105.1	52.4	105.1	105.1	105.1	105.1	490.7
LMTD	K		8.64		16.7		4.3		5.8

Table 4.4: Input design conditions of heat exchangers in heat engine cycle.

All the heat exchangers used in the CHEST system presented in this work are grouped within mainly two types, (i) Shell & Tube HEX, and (ii) Plate HEX, based on their operating temperature and pressure conditions. Both Shell & Tube and Plate HEXs offer a wide range of operating temperatures and pressures as mentioned in Table 2.7. However, plate HEX offer a limited operating pressures of upto 30 bar, while shell and tube HEX can be used for pressure values upto 200 bar [81]. Based on the operating pressures, 'Gas Cooler' and 'Common HEX' in heat pump cycle are designed using shell and tube configuration. The 'Common HEX' is same on both sides of charging and discharging cycles and follows a single design configuration. The heat pump evaporator, heat engine evaporator, recuperator and condenser are designed using plate type configuration. A plate HEX provides a compact, efficient and cost-effective solution compared to shell and tube HEXs.

4.3.1. Shell & Tube HEX

The overall design procedure of shell and tube HEX is same as listed in section 2.6.1. However, a detailed design procedure is included in the Appendix E. The design is based on the method proposed by Sinnott & Towler [81]. Unless and otherwise stated, the BEM type of shell and tube configuration, based on the TEMA standards, is used for the design of the shell and tube HEX. The single phase pressure drop and heat transfer correlations for shell side and tube side have been included in Appendix E. Further, the overall heat transfer coefficient is calculated using the relation given in Equation (E.5).

Gas Cooler

A gas cooler has been used in the heat pump cycle to cool the supercritical fluid. The input operating conditions of the gas cooler are provided in Table 4.3. The two fluids interacting in the gas cooler are the sunflower oil (storage medium) and R1233zD (working fluid). Considering the fluid allocation requirements mentioned in section 2.6.1, sunflower oil is allocated the shell side while R1233zD is allowed to pass through the tubes. The two main decisive reasons for this allocation are the operating pressure and viscosity. The input operating conditions are mentioned in Table 4.3. R1233zD operates at a very high pressure ~ 48 bar, which dictates its allocation on the tube side. Moreover, oil is highly viscous than the working fluid and viscous fluid on shell side improves heat transfer coefficient [81], which justifies its allocation on the shell side.

The heat transfer in the gas cooling process occurs in the super-critical region, where it is difficult to provide a distinction between a liquid and gas. However, "Widom" line is considered to divide the supercritical region into two zones. The fluid behaves like a liquid on one side of the Widom line while as a gas on the other side [76]. The Widom line is generally termed for the locus of the local maxima of the isobaric heat capacity at various pressure values in the vicinity of the critical point [93]. There is a sharp variation in thermo-physical properties, specifically for the isobaric heat capacity (c_p), across the Widom line which leads to the intricate phenomena in heat transfer. This sharp variation leads to dividing the super-critical region into two zones as mentioned earlier and can be visualised from the Figure E.5. The concept of the Widom line is further discussed in the Appendix E.

The preliminary design of the gas cooler developed in the present work considers a simplified situation. The super-critical region is divided into two zones, one with liquid properties and the other with gas properties. The general single phase correlations for pressure drop and heat transfer, as mentioned in Appendix E, are applied individually for the two zones considered. The total heat transfer area of the gas cooler is further calculated as the sum of heat transfer areas required in each zone.

The point distinguishing the two zones has been estimated by locating the temperature on the specific heat capacity (c_p) versus temperature (T) curve of R1233zD. The temperature corresponds to the maximum c_p value at the operating pressure. This has been illustrated in the Figure 4.5. The plot has been created using the REFPROP tool from NIST [56].

From Figure 4.5, the temperature corresponding to maximum C_p value at a pressure of 48.4 bar equals 185°C . The new design operating points of the gas cooler for individual zone have been summarised in Table 4.5.

Heat Exchanger		Gas Cooler Gas zone		Gas Cooler Liquid zone	
		Hot side	Cold side	Hot side	Cold side
Fluid		R1233zD	SFOil	R1233zD	SFOil
Temp. Inlet	$^\circ\text{C}$	192	177	185	135.1
Temp. Outlet	$^\circ\text{C}$	185	190	154.5	177
Pressure	bar	48.4	5	48.4	5
Heat Load	MW	4.26		12.94	
mass flow rate	kg/s	180.3	78.6	180.3	78.6
LMTD	K	4.3		12.9	

Table 4.5: Input design conditions of gas cooler for different zones.

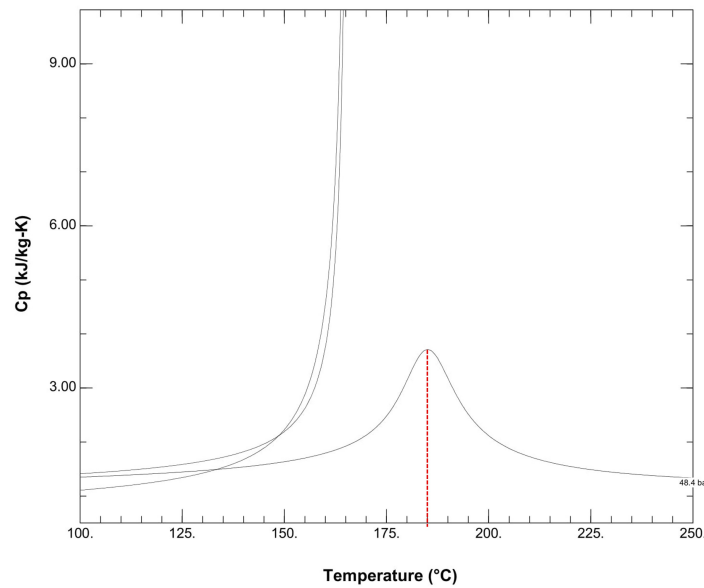


Figure 4.5: Isobaric specific heat capacity (C_p) versus temperature (T) plot for R1233zD at an operating pressure of 48.4 bar.

Common HEX

From Figure 4.1, it can be observed that the common HEX operates between gas-cooler and expansion valve during charging, while it operates between recuperator and evaporator during the discharging cycle. The valves switch the inlet and outlet ports to regulate the direction of flow of the working fluid during both the cycles. The two fluids interacting in the common HEX are the sunflower oil (storage medium) and R1233zD (working fluid). Similar to the fluid allocation in gas cooler, the sunflower oil is allocated the shell side and R1233zD on the tube side. Further, a square arrangement for tubes has been selected to facilitate easy cleaning on the outside of the tubes and also allows for easily replacing the tubes, in case of any damage [81].

From Table 4.4, it can be inferred that the approach temperature for common HEX during discharging cycle is $\sim 3K$, whereas it is more than $10K$ in the charging cycle. A low approach temperature for a HEX implies a large heat transfer area for a given heat load. Since the common HEX has to be used during the charging and discharging cycles, the heat transfer area should be same in both the cycles. The common HEX design is carried out considering the input parameters for the discharging cycle from Table 4.4. Further, the design parameters are verified for HEX operation during the charging cycle.

The pressure drop and heat transfer coefficients for shell and tube side are estimated using the correlations given in equations E.10, E.11, E.12, and E.13. The respective friction and heat transfer factors are derived from the Figures E.1, E.2, E.3, and E.4. Finally, the total heat transfer area is calculated based on the estimation of overall heat transfer coefficient for the discharge cycle case.

Results

Heat Exchanger		Gas Cooler Gas zone		Gas Cooler Liquid zone	
Heat Load	Q (MW)	4.26		12.94	
Overall HTC	$U_0 (W/m^2K)$	400		325	
Total Heat Transfer Area	A (m^2)	2930		3680	
LMTD	$\Delta T_m (K)$	4.3		12.9	
Corrected LMTD	$F\Delta T_m (K)$	3.6		10.8	
Tube Length	$L_{tube} (m)$	4.88		6.1	
Tube Outer diameter	$\phi_{OD} (mm)$	19		19	
Tube Thickness	$t_{tube} (mm)$	2.8		2.8	
Number of Tubes	$N_{tubes} (-)$	10^4		10^4	
		Shell side	Tube side	Shell side	Tube side
Fluid		oil	R1233zD	oil	R1233zD
No. of Pass		1	6	1	6
Mass Flow Rate	(kg/s)	78.6	180.3	78.6	180.3
Heat Transfer Coefficient	$\alpha (W/m^2K)$	690	4100	700	2380
Pressure Drop	$\Delta P (bar)$	0.35	0.14	0.43	0.08

Table 4.6: Shell and Tube design specifications for the Gas Cooler.

Heat Exchanger		Heat Pump				Heat Engine	
		Gas Cooler		Common HEX		Common HEX	
Heat Load	Q (MW)	17.2		21.14		14.09	
Overall HTC	$U_0 (W/m^2K)$	180		300		300	
Heat Transfer Area	A (m^2)	6600		5445		5435	
LMTD	$\Delta T_m (K)$	7.7		15.4		10.3	
Corrected LMTD	$F\Delta T_m (K)$	6.5		12.9		8.64	
Tube Length	$L_{tube} (m)$	11		7.32		7.32	
Tube Outer diameter	$\phi_{OD} (mm)$	19		19		19	
Tube thickness	$t_{tube} (mm)$	2.8		2.8		2.8	
Number of tubes	$N_{tubes} (-)$	10^4		12463		12463	
Volume	V (m^3)	43.2		35.4		35.4	
		Shell side	Tube side	Shell side	Tube side	Shell side	Tube side
Fluid		oil	R1233zD	oil	R1233zD	oil	R1233zD
No. of pass		1	6	1	6	1	6
Mass flow rate	(kg/s)	78.6	180.3	78.6	180.3	52.4	105.1
Heat Transfer Coefficient	$\alpha (W/m^2K)$	350	1500	690	1195	460	866
Pressure drop	$\Delta P (bar)$	0.78	0.22	0.43	0.05	0.2	0.02

Table 4.7: Shell and Tube design specifications for the Common HEX and Gas cooler.

4.3.2. Gasketed plate HEX

The overall design procedure of gasketed plate HEX is same as enumerated in section 2.6.1. However, a detailed design procedure is included in the Appendix E. Depending upon the flow conditions and nature of the heat transfer phenomena, the geometry, pressure drop and heat transfer correlations vary. The single phase correlations are, however, . The standard single phase pressure drop and heat transfer correlations have also been included in the Appendix E. Unless, and otherwise stated, a typical chevron plate is considered with a corrugation angle, $\beta = 35^\circ$. Carbon Steel is used as the material for plates, with a thermal conductivity of $\lambda_p = 55 \text{ W/m} - \text{K}$. The necessary fouling factors have also been included in the calculations. The overall heat transfer coefficient (U) of the plate heat exchanger is calculated using the relation given in Equation (E.6).

Heat pump evaporator design

The waste heat from the electrolyser is fed to the heat pump evaporator using water as the heat transfer medium as shown in Figure 4.1. The input data for designing the heat pump evaporator is given in Table 4.3. The pressure drop within the plate HEX is estimated using Equation (E.25). The two-phase pressure drop across the plates is dependent on the two-phase fanning friction factor (f_{TP}) through the following relation:

$$\Delta P_{TP} = 2f_{TP} \frac{G^2 L_p}{\rho d_e} \quad (4.1)$$

where, G is the mass flux through the plate channels. The two phase friction factor f_{TP} correlation used in this work is developed by Yan and Lin [90], which is formulated as follows:

$$f_{TP} = 31.21 Re_{eq}^{0.04557} Re^{-0.5}; \quad Re_{eq} \geq 6000 \quad (4.2)$$

Similarly, for evaporation heat transfer coefficient, the correlation defined by Yan and Lin (2007) is used since it provides the best approach for equivalent Reynolds number between 2000 and 10000. However, the original equation by Yan & Lin is multiplied by a factor of 10 to adjust with the experimental results [41] and is stated as:

$$\alpha_{TP} = 19.26 Re_{eq} Re_L^{-0.5} Pr_L^{1/3} Bo_{eq}^{0.3} \left(\frac{\lambda_L}{d_e} \right), \quad (4.3)$$

$$Re_{eq} = G_{eq} \frac{d_e}{\mu_L}, \quad (4.4)$$

$$Bo_{eq} = \frac{q_w''}{G_{eq} \Delta h_{fg}}, \quad (4.5)$$

$$G_{eq} = G \left[(1-x) + x \left(\frac{\rho_L}{\rho_g} \right)^{0.5} \right]. \quad (4.6)$$

where, Re_{eq} , Bo_{eq} , & G_{eq} represent the equivalent Reynolds number, boiling numbers, and mass flux respectively. The boiling number is the ratio of the wall heat flux (q_w'') to the product of equivalent mass flux through the plate channels and enthalpy of evaporation. The term 'x' represents the quality or vapor fraction in the two-phase region, which is generally assumed equal to 0.5 for obtaining average quantity.

The Q-T diagram depicting the evaporation at heat pump evaporator is shown in Figure 3.2. The equations from 4.1 to 4.6, are only valid in the two phase region, which are used to evaluate the heat transfer area required for evaporation. However, for the superheating at the end of the evaporator, single phase correlations have been used to estimate the sensible heat transfer area. The total heat transfer area of the evaporator is then approximated by the sum of the individual areas.

Heat engine evaporator

This evaporator operates in the discharging cycle, where hot sunflower oil is used to evaporate the working fluid of the organic Rankine cycle. The input data for designing the heat engine evaporator is provided in Table 4.4.

The single phase pressure drop correlation remains same as given in Equation (E.29) in Appendix E. However, the one phase correlation for heat transfer coefficient mentioned in Equation (E.23) cannot be used in this case because it is valid for purely turbulent flows. Since the fluid undergoing sensible heat transfer is a highly viscous oil, it operates in a laminar region. A single phase heat transfer correlation for laminar flow is developed by Winkelmann (2010) [89], and is formulated as below:

$$\alpha_{sp} = 0.6Re^{0.51}Pr^{1/3} \left(\frac{\lambda}{d_e} \right); \quad 10 < Re < 450 \quad (4.7)$$

where, α_{sp} denotes the heat transfer coefficient in the single phase.

For two phase pressure drop and heat transfer, correlations mentioned from Equation 4.1 to 4.6 has been effectively used. This evaporator too has a certain degree of superheat ($< 1K$), but is very insignificant compared to the evaporator heat load. The total heat transfer area has been calculated based on the heat load in two phase region.

Condenser

The heat engine condenser operates between condensing R1233zd and water at ambient conditions. The input data for the condenser design is provided in Table 4.4. For the single phase pressure drop and heat transfer coefficients, the correlations mentioned in Appendix E from equations E.29 to E.24 have been used.

For two phase pressure drop in a condenser, the correlations for friction factor developed by Infante Ferreira and Tao (2019) has been used, which is formulated as given in Equation (4.8). The correlations are based on the experimental database and is better compared to existing correlations [78].

$$f_{TP} = (4.207 - 2.67\beta^{-0.46}) (4200 - 5.41Bd^{1.2}) Re_{eq}^{-0.95} \left(\frac{P_{sat}}{P_{cr}} \right)^{0.3}, \quad (4.8)$$

$$Bd = \frac{(\rho_L - \rho_G)gd_e^2}{\sigma}. \quad (4.9)$$

where, Bd is the Bond number which represents the ratio of buoyancy force to surface tension, σ is the surface tension in N/m and g is the standard gravitational acceleration (m/s^2). Further, P_{sat} and P_{cr} indicates the saturation pressure corresponding to condensation temperature and critical pressure of the working fluid respectively.

Similarly, the two phase heat transfer correlation used is developed by Longo et al. (2015) which estimates the local heat transfer coefficient of saturated vapor based on projected area which includes the area enhancement factor (Φ) of plates [58]. This has been formulated as:

$$\alpha_{conv,sat} = 1.875\Phi Re_{eq}^{0.445} Pr_L^{1/3} \left(\frac{\lambda_L}{d_e} \right); \quad G \geq 20 \text{ kg/sm}^2 \quad (4.10)$$

where, $\alpha_{conv,sat}$ represents the local heat transfer coefficient for forced convection condensation of saturated vapor. Figure 3.5, represents the condensation at the heat engine condenser. As can be observed, the cooling of working fluid starts with vapor de-superheating followed by condensation of saturated vapor while Equation (4.10) is only valid in the two-phase region. In order to account for condensation of superheated vapor at the condenser inlet, Longo et al. (2015) presented a combined model coupled with the model developed by Webb [58, 87]. The combined local heat transfer coefficient is formulated as follows:

$$\alpha_{conv,sup} = \alpha_{conv,sat} + F \left[\alpha_{s-ph} + \frac{c_{p,G}q_{lat}}{\Delta h_{LG}} \right] \quad (4.11)$$

where, the terms $c_{p,G}$, q_{lat} , & Δh_{LG} corresponds to superheated vapor specific heat capacity, heat flux during phase change, and enthalpy of condensation. The factor F is corresponding to the ratio between degree of superheat and driving temperature difference. The term α_{s-ph} indicates the local heat transfer

coefficient for the single phase.

$$F = \left(\frac{T_{sup} - T_{sat}}{T_{sat} - T_{wall}} \right), \quad (4.12)$$

$$\alpha_{s-ph} = 0.2267 Re_G^{0.631} Pr_G^{1/3} \left(\frac{\lambda_G}{d_e} \right) \quad (4.13)$$

The total heat transfer area has been estimated based on the overall heat transfer coefficient calculated using Equation (4.11).

Recuperator

As can be inferred from Figure 4.1, & 4.2, a recuperator has been placed in the heat engine cycle following the turbine to facilitate internal heat recovery. The recuperator works with the fluids in single phase region. One side of recuperator has a cold liquid and other side has a hot gas. The input data for recuperator design is provided in Table 4.4.

For this particular case, a smooth longitudinal flow is considered through the channels of the plate HEX, which implies a corrugation angle $\beta = 0^\circ$. This is done in order to restrict the high pressure drop on the gas side. Further the pressure drop across the plate is estimated based on the friction factor (ξ_0) developed for smooth longitudinal flows, as given in Equation (E.30), and (E.31).

For heat transfer coefficient, correlations for single phase has been used as mentioned in Appendix E from equations E.23 and E.24 based on the Reynolds number for the cold and hot fluid. Further, the total heat transfer area is estimated based on the overall heat transfer coefficient calculated from the single phase correlations as mentioned above.

Results

Heat Exchanger		Heat Pump		Heat Engine					
		Evaporator		Evaporator		Recuperator		Condenser	
Heat Load	Q (MW)	30		11.47		1.66		20.61	
Overall HTC	U_0 (W/m^2K)	2000		600		600		2000	
Heat Transfer Area	A (m^2)	3100		1140		695		1828	
LMTD	ΔT_m (K)	4.9		17.9		4.3		5.8	
Corrected LMTD	$F\Delta T_m$ (K)	4.8		16.7		4		5.6	
Plate Dimensions	$L_p \times W_p$ (m^2)	1.8×0.9		1.8×0.9		2.8×1.4		1.8×0.9	
HEX Length	L_{HEX} (m)	6.3		2.4		0.8		4.2	
Volume	V (m^3)	10.2		3.9		3.14		6.8	
		Cold side	Hot side	Cold side	Hot side	Cold side	Hot side	Cold side	Hot side
Fluid		R1233zD	water	R1233zD	oil	R1233zD	R1233zD	water	R1233zD
Mass flow rate	\dot{m} (kg/s)	180.3	895	105.1	52.4	105.1	105.1	493	105.1
Heat Transfer Coef.	α (W/m^2K)	4670	13680	3655	755	2140	1035	12100	4430
Pressure drop	ΔP (bar)	0.5	1.9	0.37	0.02	0.13	0.32	0.82	0.58

Table 4.8: Plate HEX design specifications for evaporator, recuperator and condenser.

4.4. Turbomachinery Sizing

The Chapter 2.6.2 discussed the operating principle and a basic geometry of the turbomachines. It also included a brief categorisation of turbomachines based on the direction of relative motion of fluid across the turbomachine and based on the nature of energy transfer. From the latter, turbomachines can be classified into a pump/compressor or a turbine, with an axial or radial configuration.

In the present case study, the CHEST system discussed in Figure 4.1 consists of two main turbomachines: (i) a compressor in the heat pump cycle, and (ii) a turbine in the heat engine cycle. The preliminary design of these turbomachines are carried out using the methodology developed by Balje [7, 8], which has been outlined in Chapter 2.6.2. Further, the necessary selection criteria and preliminary design parameters of a turbomachine have been provided in Chapter 2.6.2 using a dimensional analysis. The direct result of the dimensional analysis is to express the turbomachine efficiency (η) in terms of two dimensionless parameters, specific speed (N_s), and specific diameter (D_s), which are again stated in Equation (4.14) and (4.15).

$$N_s = \frac{2\pi N}{60} \cdot \frac{(\dot{m}/\rho_{av})^{0.5}}{\Delta h_{is}^{0.75}}, \quad (4.14)$$

$$D_s = D \cdot \frac{\Delta h_{is}^{0.25}}{(\dot{m}/\rho_{av})^{0.5}}. \quad (4.15)$$

where, \dot{m} is the mass flow (kg/s), ρ_{av} is the average density (kg/m^3) of inlet and outlet for each stage, Δh_{is} is the enthalpy rise per stage (J/kg), N is the rotational speed (rpm), and D is the impeller or blade tip diameter (m).

The input data required for a preliminary design of the turbomachines in the present CHEST system is given in Table 4.9.

Turbomachine		Compressor	Turbine
Work	\dot{W} (MW)	8.34	5.14
Mass flow	\dot{m} (kg/s)	180.3	105.1
Inlet Volumetric flow	\dot{V} (m^3/s)	9.6	0.878
Outlet Volumetric flow	\dot{V} (m^3/s)	0.47	18.86
Inlet pressure	P_{in} (bar)	5.1	20
Outlet pressure	P_{out} (bar)	48.4	1.1
Pressure ratio	PR (-)	9.5	18.5

Table 4.9: Input specifications of the turbomachines of the CHEST system shown in Figure 4.1.

Step-1: Select the type of turbomachinery based on mass flow, and overall pressure ratio

Considering the key differences and operating conditions of axial and radial flow machines shown in Figure 2.28, a preliminary choice between radial and axial machine is done for compressor, and turbine. From Table 4.9, the compressor requires a power input of 8.34 MW to achieve a pressure ratio ~ 9.5 . Axial compressors offer very low pressure ratio per stage $\sim 1 - 1.2$, which requires a large number of stages [14]. Moreover, axial compressors are quite complex to design than its radial counterpart. When considering the inlet volumetric flow rate of compressor ($\sim 9.6 m^3/s$), it lies within the radial flow regime, which can accept flow rates upto 500 thousand m^3/hr [54].

Similar to compressors, the axial turbine provides a lower expansion ratio per stage as compared to the centrifugal turbine [22]. Where a centrifugal turbine can allow an expansion ratio of upto 9:1, an axial turbine can allow an expansion ratio of upto 2-3:1. However, axial turbines provide much higher efficiency at higher power outputs and are suitable for higher mass flow rates [85].

So, a preliminary design is carried out on a radial compressor and an axial turbine.

Step-2: Determine optimum range of N_s from Balje diagram

Figures 4.6, 4.7 exhibits the Baljé diagram for single stage compressors and turbines respectively. Baljé diagrams are an extension to the Cordier diagram given by Lewis (1996) [72], and maps out the turbomachinery efficiency for different sets of N_s and D_s values. From the figures below, it can be observed that operating range of N_s values for centrifugal compressors lies between $0.1 < N_s < 0.8$, while for axial turbines, the N_s values are between $0.1 < N_s < 8$. However, for maximum efficiency, the optimum N_s values for radial compressor are between $0.5 < N_s < 0.7$, which provides a maximum efficiency $\sim 80-85\%$. For axial turbines, the range is wider for highest efficiency $\sim 90\%$ and is between $0.5 < N_s < 0.95$.

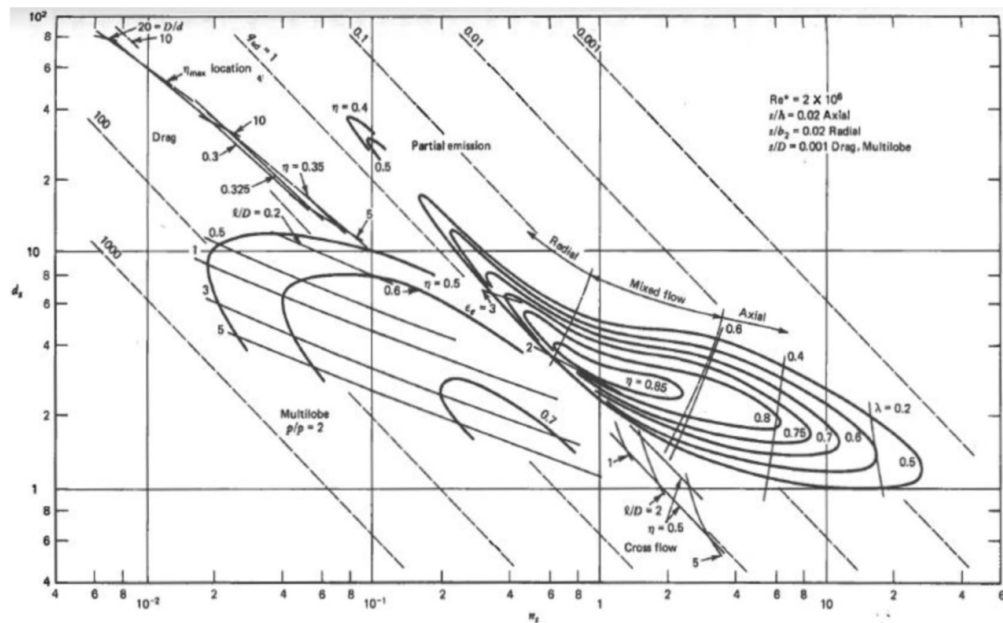


Figure 4.6: Baljé diagram for single stage compressors [7, 8].

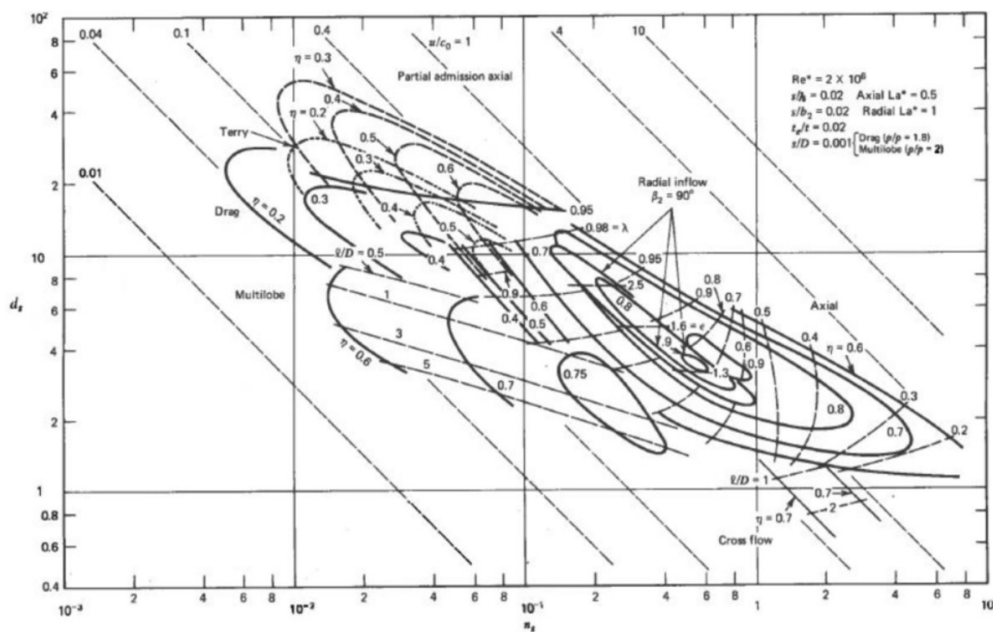


Figure 4.7: Baljé diagram for single stage turbines [7, 8].

Step-3: Determine optimum number of stages and shaft speed

The number of stages for a turbomachine is estimated from the overall pressure ratio specified for the turbomachine and maximum pressure ratio that can be obtained from the turbomachine in one stage. Further, the shaft speed (N) is estimated from Equation (4.14) for the range of N_s values mentioned in the step-2. Prior to determining the shaft speed, the volumetric flow rate per stage is estimated considering an average density between the inlet and outlet of the turbomachinery stage. Additionally, the reversible work of the turbomachine is equally divided between the individual stages $\Delta h_{is}/z$, where z is the number of stages.

• Centrifugal compressor:

From Table 4.9, the overall PR for the compressor is 9.5 while, a maximum pressure ratio of 5-7 is achievable per stage of the centrifugal compressor [54]. As a result, a radial compressor with two stages having the stage PR of 3.08 has been selected.

Further, to estimate an optimum shaft speed for the centrifugal compressor, a correlation has been developed between the N_s values and the shaft speed (N), which is shown in Figure 4.8 for a two-stage centrifugal compressor.

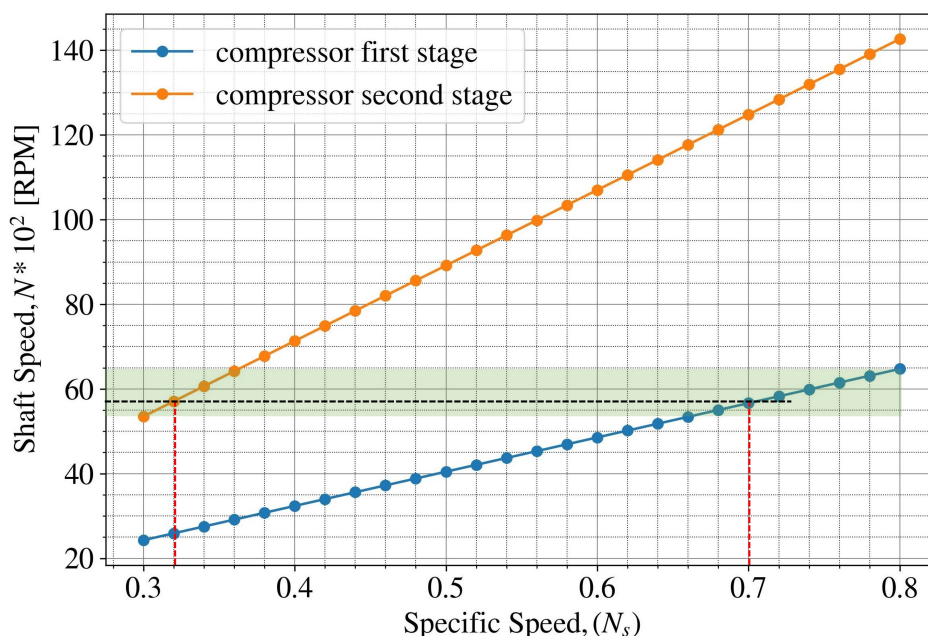


Figure 4.8: Shaft speed vs Specific speed correlation for a two-stage centrifugal compressor with an overall PR of 9.5.

As stated in step-2, the optimum N_s value range, for a centrifugal compressor, to attain maximum efficiency is $0.5 < N_s < 0.7$. From Figure 4.8, the highlighted region provides the range of shaft speed (N) for which the N_s values per stage lies within the operating range. An optimum $N = 5700 \text{ rpm}$ has been selected as shown by the black dashed line, which corresponds to $N_s = 0.7$ & 0.32 for first and second compressor stage respectively. From the Baljé diagram for the compressor shown in Figure 4.6, these N_s values corresponds to an efficiency of 70% & 80% for first and second stage respectively.

• Axial turbine:

From Table 4.9, the overall PR for the turbine is 18.5, while a maximum expansion ratio of 2-4 is achievable per stage of the axial turbine. A higher PR more than 4 results in a considerable efficiency loss [5]. As a result, an axial turbine with three stages having the stage compression ratio of 2.64 has been selected.

Similar to the compressor, a correlation has been developed between the N_s values and the shaft speed (N), to estimate an optimum shaft speed for the axial turbine, which is shown in Figure 4.9 for a three-stage axial turbine.

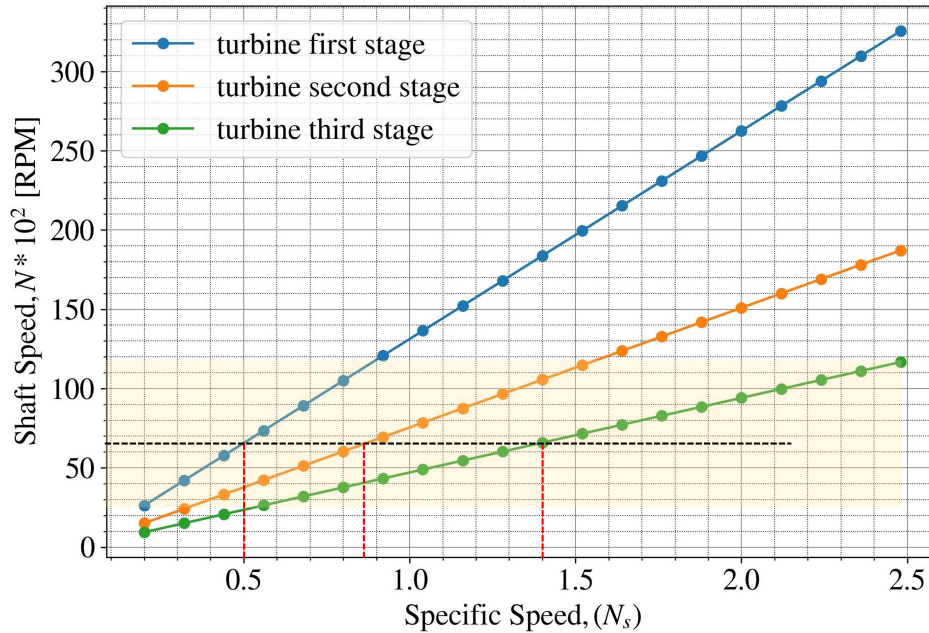


Figure 4.9: Shaft speed vs Specific speed correlation for a three-stage axial turbine with an overall PR of 18.5.

As stated in step-2, the optimum N_s value range, for a axial turbine, to attain maximum efficiency is $0.5 < N_s < 0.95$. From Figure 4.9, the highlighted region provides the range of shaft speed (N) for which the N_s values per stage lies within the operating range. An optimum $N = 6500 \text{ rpm}$ has been selected as shown by the black dashed line, which corresponds to $N_s = 0.5, 0.85$ & 1.4 for first, second, and third turbine stage respectively. From the Baljé diagram for the turbine shown in Figure 4.7, these N_s values corresponds to an efficiency of 90%, 90%, & 85% for first, second and third stage respectively.

Step-4: Determine the tip diameter

From the N_s values obtained in step-3, the corresponding specific diameter D_s values is read from the Baljé diagram from Figure 4.6 & 4.7 for compressor and turbine respectively. Further, the tip diameter is evaluated using Equation (4.15) for each individual stage.

4.4.1. Results

Turbomachine		Radial Compressor		Axial Turbine		
Stage		First	Second	First	Second	Third
Shaft Power	$P_{shaft} (MW)$	4.17	4.76	1.75	1.75	1.66
Pressure ratio	PR (-)	2.67	3.54	2.74	2.57	2.62
Isentropic Enthalpy	$\Delta h_{is} (kJ/kg)$	18.5	18.5	18.54	18.54	18.54
Volumetric flow rate	$\dot{V} (m^3/s)$	3.5	0.72	1.33	4.04	10.4
Specific speed	$N_s (-)$	0.7	0.32	0.5	0.85	1.4
Shaft speed	$N (rpm)$	5700	5700	6500	6500	6500
Specific diameter	$D_s (-)$	4.4	8	3.8	3.6	2.6
Tip diameter	$d_t (m)$	0.71	0.58	0.376	0.62	0.72
Balje Efficiency	$\eta_{Balje} (%)$	80	70	90	90	85
Overall Efficiency	$\eta_{overall} (%)$		75		88.3	

Table 4.10: Preliminary design specifications of the compressor and turbine used in the CHEST system shown in Figure 4.1.

4.5. CHEST components overall design

From the turbomachine preliminary design results as summarised in Table 4.10, the overall isentropic efficiency of compressor and turbine evaluated is 75%, and 88.3% respectively. However, when compared with the assumed values as given in Table 4.1, the compressor efficiency evaluated is lower than the assumed value (80%). For turbine, the isentropic efficiency is similar as assumed (88%). This implies an extra work input is needed to drive the compressor, which would reduce the performance of the system.

From the heat exchangers result, as given in Table 4.7 and 4.8, the total pressure drop estimated on the heat pump side is 0.7 bar , whereas, a pressure drop of 1.1 bar is estimated on heat engine side. The pressure drop values are significantly less when compared with the operating pressures of the heat pump (48.4 bar) and heat engine (20 bar). However, to verify the effect of pressure drop on system performance, the calculated pressure drop can be added to the compressor and pump work.

The updated T-S and E-T plot for the CHEST system, considering the calculated turbomachinery efficiencies and heat exchanger pressure drops is shown in Figure 4.10 and 4.11. The optimised state parameters have been changed as a consequence of updated turbomachinery efficiency values and pressure drop values. As a result, the overall RTE of the system has come down to $\sim 89.3\%$ as compared to 92% for the initial system.

It is the compressor efficiency and the pressure drop in heat pump which has impacted the RTE of the system. An excess pressure drop on heat pump side has to be compensated by the extra compressor work. Whereas an excess pressure drop on heat engine side is compensated by some extra pump work, which is significantly less as compared to compressor work. Therefore, in order to achieve high round trip efficiencies, a compressor with high isentropic efficiency is required.

Temperature-Entropy (T-S) diagram

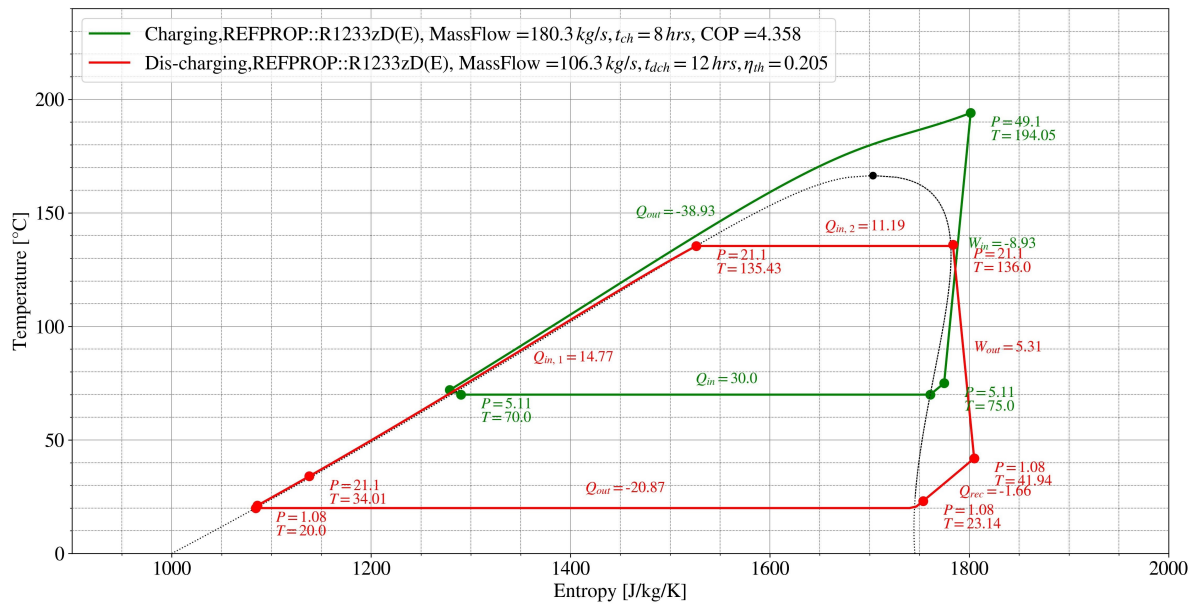


Figure 4.10: T-S plot with updated isentropic efficiency.

Energy-Temperature (E-T) diagram

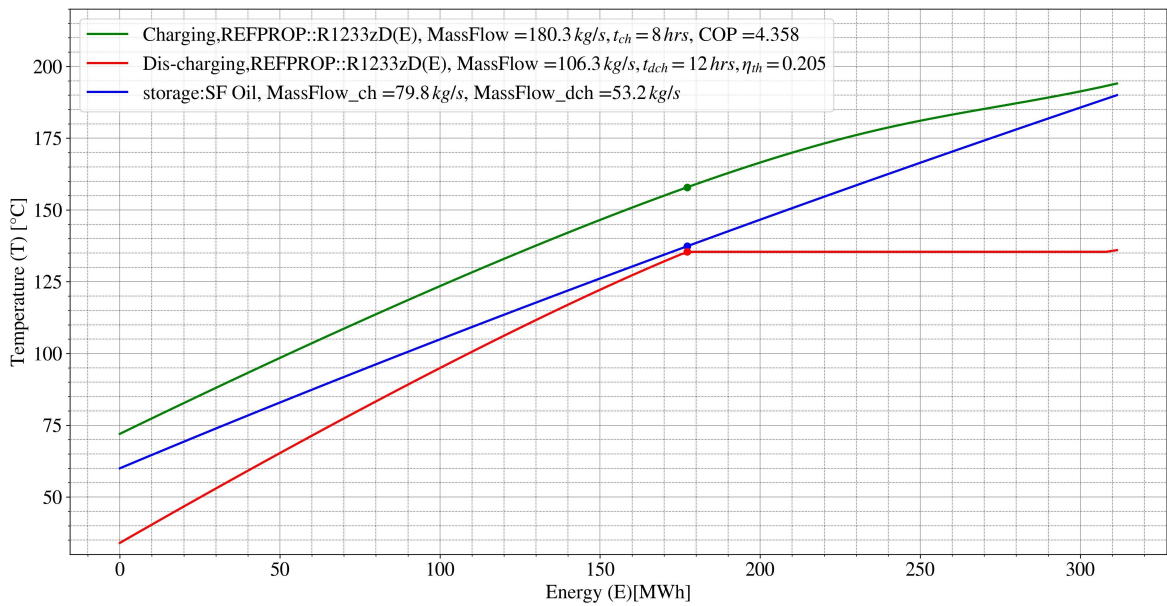


Figure 4.11: E-T plot depicting the energy transfer between heat pump, storage and heat engine cycles.

5

Summary, Conclusions & Future Work

In this thesis, a conceptual design and model of a waste heat integrated Pumped Thermal Energy Storage (PTES) / Compressed Heat Energy Storage (CHEST) system is developed. This included the following:

- An in-depth literature study of PTES systems is conducted. From the study, it is found that the standard PTES systems operating between cold and hot storage could provide a Round Trip Efficiency (RTE) upto $\sim 60 - 65\%$. Whereas, a waste heat integrated PTES system could result in RTE of more than 100% . However, the latter requires a continuous availability of waste heat in sufficient quantities for its efficient performance.
- A detailed study on the potential working fluid and storage medium for CHEST system is carried out. R1233zD is selected as the working fluid because of its low ODP, GWP values and inflammable nature. Also, it has an isentropic T-S vapor saturation curve, a high molecular weight, and sufficient critical temperature and pressure as required by the CHEST systems.
- Steady state thermodynamic models for two different configurations of CHEST system is developed, by making specific assumptions to simplify the problem.
- **CHEST with latent heat storage:** An existing configuration of sub-critical CHEST system with a combination of latent and sensible hot storage is re-developed, however, with a different working fluid and storage medium. A hypothetical PCM is considered as the latent storage medium due to the unavailability of an efficient PCM that could be coupled with R1233zD. With this model, performance characteristics of the system is analysed. A RTE of 118% and a storage density of $0.11\text{MWh}/\text{m}^3$ for latent storage and $0.07\text{MWh}/\text{m}^3$ for sensible storage is evaluated.
- **CHEST with full sensible heat storage:** A novel combination of a trans-critical heat pump, sensible heat storage, and sub-critical heat engine is proposed. Sunflower oil as the sensible storage medium is selected for this application due to its wide and cheap availability and easy to store at ambient pressure conditions. A single objective multi-variable optimization scheme is applied to the system for achieving high RTE. A RTE of 92% and a storage density of $0.115\text{MWh}/\text{m}^3$ for sensible storage is determined.
- Finally, a comparison is performed between the two configurations with respect to the overall system performance, storage size, and economic viability.
- The optimized model of CHEST with sensible heat storage is integrated with a 100MW_e solar powered alkaline electrolyzer to utilize the waste heat $\sim 30\text{MW}_{th}$ produced during the electrolysis process.
- Finally, a preliminary design of CHEST components, i.e. heat exchangers and turbomachines are presented. This is included in order to have a rough estimation of the overall dimensions and type of equipment required.

The key conclusions of this research are summarised as follows:

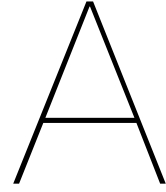
1. The PTES system with low grade waste heat integration is suitable for maximum storage temperatures upto 200°C . Beyond that, significantly less variation is observed in the performance values. However, a higher waste heat source temperature has shown to improve the overall performance of the system.
2. In terms of performance, CHEST with latent heat storage is $\sim 25\%$ more efficient than CHEST with sensible heat storage. In terms of TES energy density (MWh/m^3), a high value is found for fully sensible storage configuration due to lower storage volume as compared to the combined storage volumes in latent storage configuration.
3. The latent heat storage requires an intricate heat transfer modelling along with pressurised storage conditions. In contrast, Sunflower oil as the TES medium can be stored at ambient conditions and can easily be modelled as any other liquid. Moreover, the high availability, and low costs of using sunflower oil makes it a promising hot storage medium over latent storage for Rankine PTES system.
4. The total pressure drop in heat pump and compressor efficiency, estimated from the preliminary design of the components, had a greater impact on the overall performance of the system as compared to pressure drop in heat engine. The pressure drop for heat engine was compensated by additional pump work. This is significantly less as compared to the additional work input of a compressor for a similar pressure drop. A high efficiency compressor is necessary for high RTE of the CHEST system.

5.1. Future work

Although the CHEST system with sensible heat storage is less efficient from its latent heat storage counterpart, the former seems to be a promising solution to bring down the overall costs of energy storage. This configuration with single sensible heat storage can be further improved to have high RTE. Some future recommendations to improve the system are as follows:

1. **Pressure drop:** A constant pressure model was considered across individual components and connecting lines in the PTES system. This could lead to over representation of the performance values. A pressure drop across each component can be included for further improvement of the model.
2. **Model problem:** In the present thesis, a steady-state model has been developed. Further, a dynamic model can be developed considering the effects of variation of input power and source heat. Also, off design conditions for the system could be modelled.
3. **Working fluid:** In the present model, use of a pure fluid doesn't allow for best matching with storage medium during discharge cycle due to constant temperature heat absorption, which leads to significant exergy losses. Use of a mixture refrigerant (eg: CO_2 blends) could have a better matching with storage medium by allowing temperature glide during isobaric heat absorption.
4. **Sensible heat storage medium:** A potential storage medium with a varying specific heat such that it closely matches the thermal profile of the working fluid in the super-critical region would be an effective solution to reduce the exergy losses, thereby, increasing the performance of CHEST system with sensible heat storage.
5. **Components:** In the present work, a preliminary design of each component has been carried out. Further, a rigorous design of individual components could be carried out to best match with the performance of the system.

Finally, a techno-economic study of this system is necessary to set a trade-off between the performance of the system and costs of the components. Further, an experimental test set-up for the modelled system will be an essential step to determine the feasibility of integration of the CHEST system with industrial low grade waste heat sources.



Temperature–Entropy (T-S) vapor saturation curve

The optimum selection of the working fluid considering the nature of shape of the T-S vapor saturation requires a more generic physics-based model. Alejandro Rivera-Alvarez et al.(2020) presents such a model which accurately determines the shape of the T-S vapor saturation curve for any fluid [74].

The work of Alejandro Rivera-Alvarez et al.(2020) follows the Lee–Kesler’s version of the Principle of Corresponding States (PCS). PCS was originally introduced by Van der Waals and is called as two-parameter PCS, which states that: “Substances behave alike at the same reduced states. Substances at same reduced states are at corresponding states” [3]. This suggests that if assessed at the same reduced states (eg: reduced temperature, reduced pressure), the departure from ideal gas behavior for all fluids is identical. This can be illustrated with the help of a simple relation, as shown in Equation (A.1), which is the reduced form of the Van der Waals Equation of state,

$$\left(P_r \frac{3}{v_r^2} \right) \cdot (3\bar{v}_r - 1) = 8 \cdot T_r. \quad (\text{A.1})$$

where, $P_r = P/P_c$, $T_r = T/T_c$, $v_r = v/v_c$ are, respectively, the reduced temperature, pressure and volume at the thermodynamic state (T, P, v) of interest (with T_c , P_c , and v_c the critical temperature, pressure, and volume of the substance). From Equation (A.1), it is certain that irrespective of the nature, the fluids at same reduced states will behave alike. However, Pitzer established a deviation from standard PCS and introduced a three-parameter PCS, which states that: “Substances behave alike at the same reduced states (reduced temperature, reduced pressure) and same acentric factor (ω)”. Pitzer’s version of three-parameter PCS assumes a linear dependency of compressibility factor (Z) on the acentric factor (ω) as shown in Equation (A.2),

$$Z(T_r, P_r, \omega) = \frac{Pv}{R_g T} = Z^{(0)}(T_r, P_r) + \omega Z^{(1)}(T_r, P_r). \quad (\text{A.2})$$

where, $Z^{(0)}(T_r, P_r)$ is the compressibility factor of a fluid with complete spherical symmetry of the molecular force field ($\omega = 0$), and $Z^{(1)}(T_r, P_r)$ is a correction function that modifies the compressibility factor to account for the difference between sphericity or non-sphericity ($\omega \neq 0$) of molecules.

The Lee–Kesler’s model follows upon Pitzer’s correlation for compressibility factor, Equation (A.2), and provides an approximation for the functions $Z^{(0)}$ and $Z^{(1)}$. The governing Equations used in the model is provided in the work of Alejandro Rivera-Alvarez et al.(2020) . This model used precisely locates the isentropic points on the T-S vapor saturation curve and correctly distinguishes between dry, wet, and isentropic fluids [74]. The proposed method involves only three input variables: acentric factor (ω), k_c , and m , which can be defined here as follows,

- **Acentric Factor (ω)** : It is a measure to quantify how far a substance's thermodynamic characteristics deviate from what the two-parameter PCS predicts. It correlates the deviation in the thermodynamic properties of the fluids containing non-spherical molecules with the spherical counterparts.
- k_c : It gives the ideal-gas ratio of specific heats at the critical temperature.
- m : It is the exponent of the ideal-gas ratio of specific heats vs temperature power relationship as per the following relationship: $k = k_c T_r^m$ [74].

The governing Equations of the model can be used to define the shape of the liquid vapor co-existence region for any fluid in the Temperature-Entropy (T-S) plot. The shape of the saturation curves in the T-S plot is an essential factor in narrowing down the suitable range of working fluids for the proposed system. The slope of the T-S vapor saturation curve and the dome of the T-S plot constitutes two major factors in deciding the optimum working fluid for a given application.

Parameters Affecting the Dome

The governing Equations can be further used to develop the reduced temperature versus dimensionless entropy ($T_r - \bar{s}$) saturation dome for a given fluid. As stated earlier, it depends on only three parameters: ω , k_c , and m . This type of plot allows for a direct comparison of the dome shape for various substances based on the principle of corresponding states; it places the critical point for each substance at the same coordinates ($\bar{s} = 0$, $T_r = 1$), as shown in Figure 2.20.

A fluid with lower values of acentric factor ($\omega < 0.35$) will ensure a narrow peak of the saturation dome which facilitates less latent heat storage. A k_c value close to 1.1 maintains an isentropic vapor saturation curve, which allows for less superheating at the turbine inlet and simultaneously limited need of recuperation before the condenser of the Rankine cycle. Finally, $m \sim -0.03$ will maintain the isentropic nature of the vapor saturation curve at the lower side of the saturation dome.

Alejandro Rivera-Alvarez et al.(2020) lists the different parameters (ω , k_c , m , T_c , etc) for 120 fluids based on the Lee-Kesler model [74].

B

Optimised Parameters for Literature Case

For the base case Topology with super-heating before HP compression, the following intensive decision variables were considered with their respective lower and upper boundaries in square brackets:

- The HP low pressure p_1 ($\equiv p_4$), [17:33] bar.
- The degree of superheating before the HP compression ΔT_{SPH} , [5:50]°C.
- The HP high pressure p_2 ($\equiv p_3$), [100:200] bar.
- The HP condenser end-temperature T_3 , [274:300] K.
- The TE low pressure p_5 ($\equiv p_8$), [20:37] bar.
- The TE high pressure p_6 ($\equiv p_7$), [100:200] bar.
- The TE evaporator end-temperature T_7 , [373:450] K.
- The pressure at the evaporator of the ammonia cycle $p_{\text{NH}_3}^{\text{low}}$ [1.5:3] bar.
- The pressure at the condenser of the ammonia cycle $p_{\text{NH}_3}^{\text{high}}$ [12:15] bar.

Figure B.1: Range of parameters for optimisation

- HP parameters: $p_1 = 17.9$ bar; $\Delta T_{\text{SPH}} = 32.8$ °C; $p_2 = 122.1$ bar; $T_3 = 279$ K (5.6 °C).
- TE parameters: $p_5 = 20.7$ bar; $p_6 = 143.9$ bar; $T_7 = 449$ K (175.8 °C).

(a) ABB base case with superheating

- HP parameters: $p_1 = 18.1$ bar; $\Delta T_{12-13} = 0$ °C; $p_2 = 197.1$ bar; $T_3 = 279.8$ K.
- TE parameters: $p_5 = 21.6$ bar; $p_6 = 165.9$ bar; $\Delta T_{71-72} = -46.9$ °C; $T_{71} = 50$ bar; $T_7 = 450$ K.

(b) ABB case-1 with intercooling

Figure B.2: Optimum Parameters

Sample Calculation to estimate required Air-cooling

The required air-cooling can be estimated by employing a thermal energy balance for the system. In this case, we balance the Thermal Engine requirement on the cold storage side. The calculations are given as follows:

Assuming required Energy output = 50 MJ for a discharge time of 50s. Mass Flow rate of discharging cycle,

$$\dot{m}_{TE} = \frac{W_{out}}{dh_{out}} = \frac{1e3 kW}{99.39 kJ/kg} = 10.1 kg/s.$$

Heat rejected in cold storage in discharging cycle, $\dot{Q}_{D-5} = 294.09 * 10.1 = 2970.3 kW$.

Mass flow required for charging cycle to balance the rejected heat,

$$\dot{m}_{HP} = \frac{\dot{Q}_{D-5}}{dh_{4-H}} = \frac{2970.3}{240.81} = 12.33 kg/s.$$

Heat stored in the hot storage (charging),

$$\dot{Q}_{2-C} = \dot{m}_{HP} * dh_{2-C} = 12.33 * 360.35 = 4443.1 kW.$$

Heat rejected from the hot storage (discharging),

$$\dot{Q}_{E-7} = \dot{m}_{HE} * dh_{E-7} = 10.1 * 379.48 = 3832.748 kW.$$

Excess heat within the system,

$$\dot{Q}_{excess} = \dot{Q}_{2-C} - \dot{Q}_{E-7} = 4443.1 - 3832.748 = 610.37 kW \quad (\text{cold utility}).$$

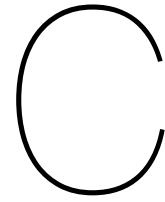
Specific enthalpy to be removed,

$$dh_{cooling} = \frac{\dot{Q}_{excess}}{\dot{m}_{HP}} = \frac{610.37}{12.33} = 49.5 kJ/kg.$$

This heat is specifically removed from the charging cycle in between the supercritical CO₂ cooling process.

Now the Round Trip Efficiency (RTE) of the cycle can be calculated for same charging and discharging time as follows:

$$\text{RTE, } \eta_{RT} = \frac{W_{TE} * \tau_D}{W_{HP} * \tau_C} = \frac{1000}{12.33 * 130.61} = \mathbf{62.3\%}.$$



CO₂ Blends

CO₂ Blends as a working fluid

CO₂-Blends are typically a mixture of a selective dopant and CO₂. These mixtures can be used to address the problems encountered due to low critical temperature of pure CO₂. For example, in sCO₂-based CSP plants, high ambient temperatures (~40°C) prevent compression near the critical point (31°C). This prevents from making use of the benefit of a low compressibility factor in the vicinity of the critical point. G. Di Marcoberardino et al. have proposed to use a CO₂-blend, which raises the critical point of the pure CO₂ [27], as shown in Figure C.1. The sCO₂ Brayton cycle can be converted to a trans-critical CO₂ Rankine cycle, allowing condensation in the two-phase region and also replacing the compressor with a pump, thus reducing power input. It is also possible to appreciate the reduction in compression power observed for same compressor inlet temperature and pressure ratio, Figure C.1.

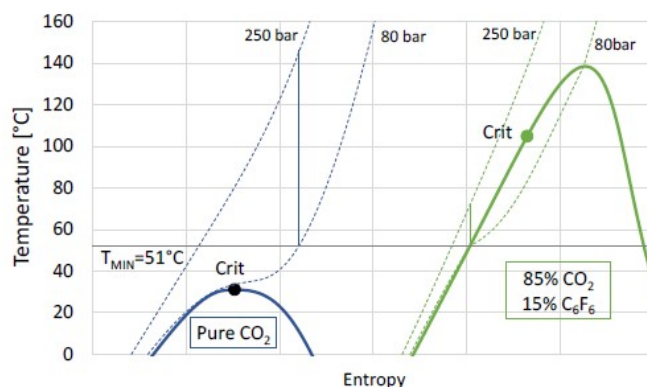


Figure C.1: Effect of dopant on the critical point [28].

The dopants are characterised by a good solubility into CO₂, good molecular complexity, low-toxicity and low-flammability. Also, they should be thermally stable and chemically inert at higher temperatures. The work of G. Di Marcoberardino et al. compares different dopants (eg: C₆F₆, TiCl₄, and SF₆) that could be used with CO₂. Higher performance gain of hexa-fluoro benzene (C₆F₆) over titanium tetra-chloride (TiCl₄) was reported for the precompression layout [27].

G. Di Marcoberardino et al. carried out the thermal stability checks for the proposed dopant, CO₂+C₆F₆, and reported a temperature limit of 600°C [26]. A performance investigation of the mixture was further carried out for a CSP plant at a maximum cycle temperature of $T_{max}=550^{\circ}\text{C}$ [28]. A simple recuperative CO₂ trans-critical Rankine cycle with a CO₂ molar content of 84% was found to deliver the maximum efficiency of 41.9% compared to the lower efficiencies of steam Rankine cycle and simple recuperative sCO₂ Brayton cycle, as evident from Figure C.2.

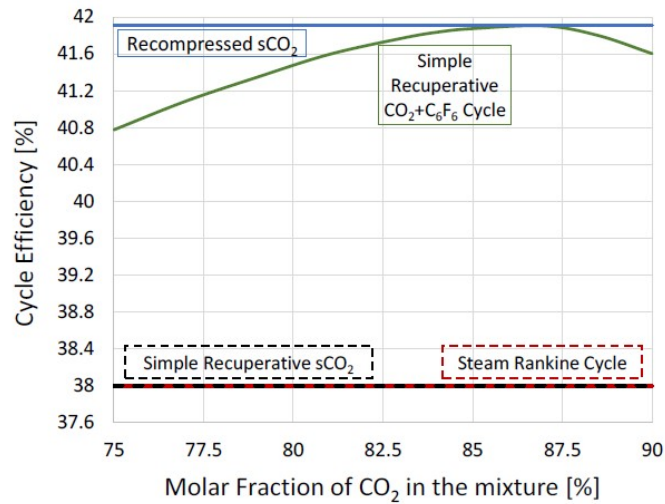


Figure C.2: Gross cycle efficiency CSP applications [28].

Finally, Figure C.3a & Figure C.3b represent the phase diagram of CO₂+C₆F₆ and a T-S plot corresponding to a simple recuperated trans-critical Rankine cycle for a typical CSP plant using trans-critical CO₂+C₆F₆ mixture with 84% CO₂ molar content.

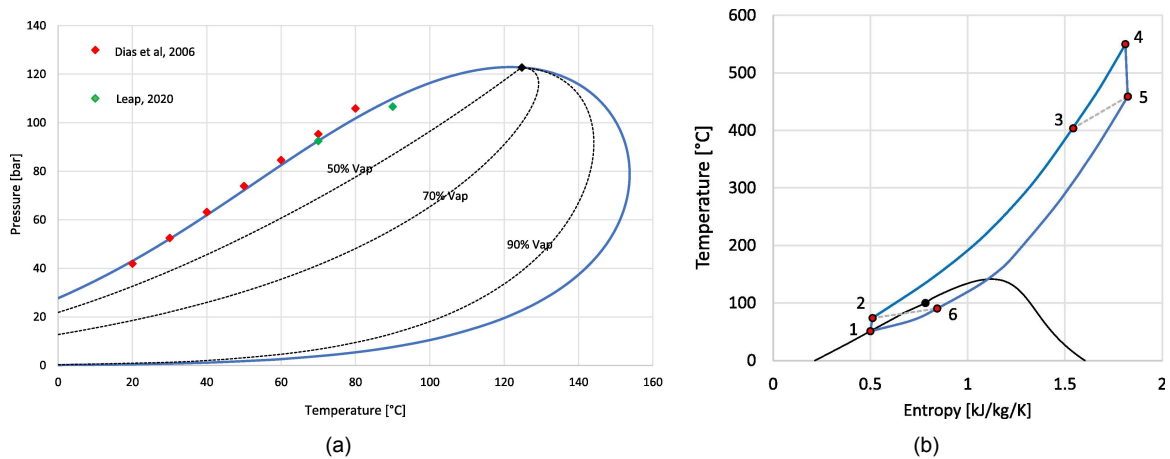
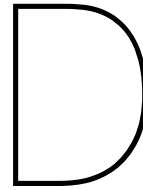


Figure C.3: (a) P-T diagram of (C₆F₆) with standard Peng-Robinson EoS [26], (b) T-S diagrams of simple recuperative condensing supercritical cycle for the mixture with 84% CO₂ molar content [26].

CO₂ blends offers a very nice solution for integrating waste heat with CO₂ cycles. Based on the previous findings, CO₂ + C₆F₆ tends to be an efficient mixture.



Computational Model Description

Python is an open source software used as a high level, general-purpose programming language. It is compatible with a wide range of programming paradigms, including structured (especially procedural), object-oriented, and functional programming. Moreover, it contains the Python Package Index (PyPI), which hosts thousands of third party modules for python [82]. Of these modules/packages, the ones extensively used in the present work are CoolProp, Matplotlib, and SciPy. These packages need to be installed on the system and imported within the Python environment. The functions of these packages are as follows:

1. **CoolProp:** This package is a database of nearly 122 pure and pseudo-pure fluids, which contains all the thermodynamic and transport properties of these components [11].
2. **Matplotlib:** It is a complete Python toolkit for producing static, animated, and interactive visualizations in Python [48].
3. **SciPy:** SciPy is a Python package collection for mathematics, science, and engineering numerical computations [83].

The complete model had been divided into four classes: ThermoState, Heat Pump, Heat Engine, Storage, as shown in Figure D.1.

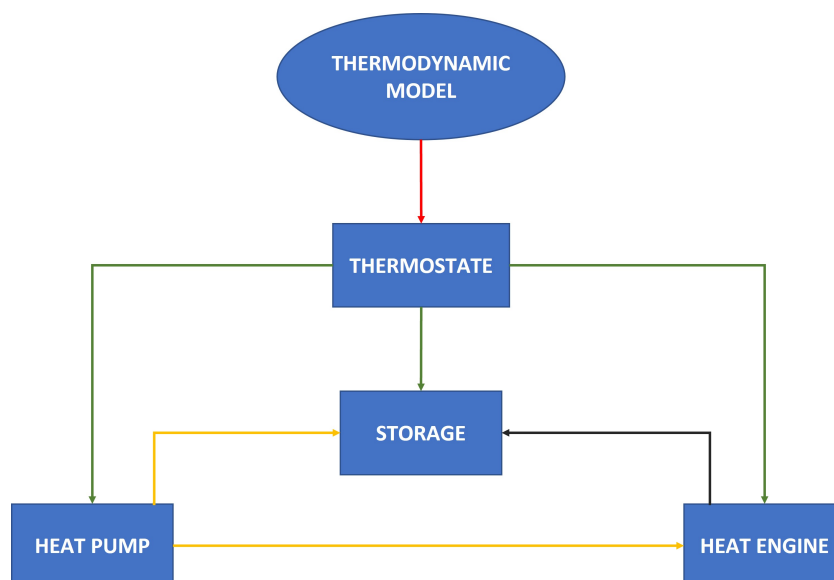


Figure D.1: Different Python class defined in thermodynamic model

The “THERMOSTATE” class is at the top of the thermodynamic model, which is responsible to evaluate all the properties of a state point for any given pair of state variables (eg: temperature, pressure, specific entropy, specific enthalpy, etc.). It is called every time, a function in another class try to define state points.

The “HEAT PUMP” class is responsible to define all the state points of the heat pump cycle. It also calculates performance related (eg: COP) and flow related (eg: mass flow rate) parameters. Moreover, it also generates temperature vs entropy (T-S) and heat load vs temperature (Q-T) plots for heat pump cycle.

Similarly, the “HEAT ENGINE” class is responsible to define all the state points of the Rankine cycle. Additionally, it takes input from the “HEAT PUMP” class to define certain state parameters. This is shown through the yellow line in Figure D.1. Further, it calculates performance related (eg: thermal efficiency) and flow related (eg: mass flow rate) parameters. It also generates temperature vs entropy (T-S) and heat load vs temperature (Q-T) plots for the Rankine cycle.

Finally, the “STORAGE” class defines the state properties at the initial and end state point. It takes input from both the “HEAT PUMP” and “HEAT ENGINE” class to evaluate certain parameters. This is shown via the yellow and black line in Figure D.1.

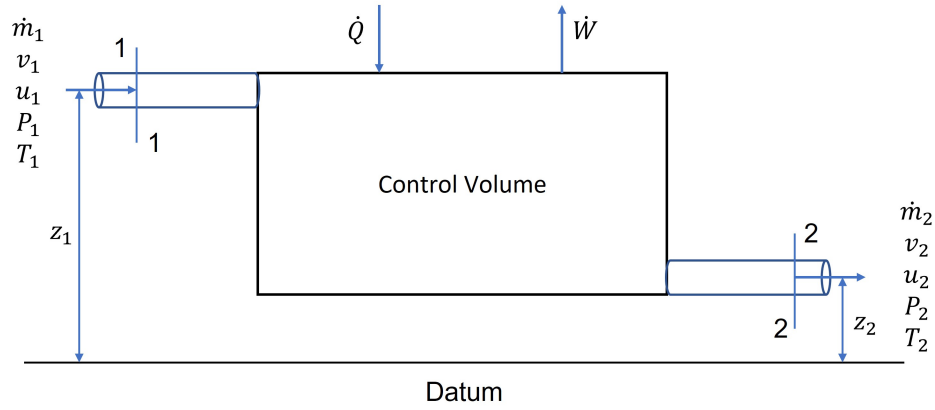


Figure D.2: Steady flow energy process

where, 1, 2 represents the inlet and outlet of the control volume. From the thermodynamic sign conventions, heat given to the system and work obtained from the system are taken to be positive and vice versa. A total mass and energy balance for such a control volume, shown in Figure D.2, is as follows:

$$\dot{m}_1 - \dot{m}_2 = \frac{dm}{dt}, \quad (\text{D.1})$$

$$\dot{E}_1 + \dot{Q} - \dot{E}_2 - \dot{W} = \frac{dE}{dt}, \quad (\text{D.2})$$

where, \dot{m} and \dot{E} represents the mass flow rate and energy rate respectively. The term “E” is a combination of all the major energy sources carried by the fluid such as internal energy (U), flow work (pV), kinetic energy (K.E), and potential energy (P.E) and can be written as:

$$E = U + pV + 0.5mv^2 + mgz, \\ e = E/m = u + pv + v^2/2 + gz. \quad (\text{D.3})$$

where, e, u, v represents specific total energy, specific internal energy, and specific volume of the fluid in consideration. While v, g, z represent the velocity, gravitational acceleration and potential elevation from the reference line. Substituting Equation D.3 in D.1 and D.2, and for a steady state, the above

mass and energy balance Equations reduces to,

$$\begin{aligned} \dot{m}_1 &= \dot{m}_2 = \dot{m}, \\ \dot{E}_1 - \dot{E}_2 &= \dot{W} - \dot{Q}, \\ \dot{m} \left((h_1 - h_2) + \frac{1}{2}(v_1^2 - v_2^2) + g(z_1 - z_2) \right) &= \dot{W} - \dot{Q}. \end{aligned} \quad (\text{D.4})$$

where, $h = u + pv$, represents the specific enthalpy of the fluid. This defines the steady-state mass and energy balance for a control volume of a two component system and can be extended to a multi-component system as well.

Equation D.4 forms the basis of the main thermodynamic calculations carried out for individual components in the PTES system. The main elements of a PTES system, as can be referred from Figure 3.1, are : (i) heat exchangers, (ii) turbomachinery, and (iii) expansion valve.

1. Heat Exchangers:

Consider the heat exchanger block as shown in Figure D.3.

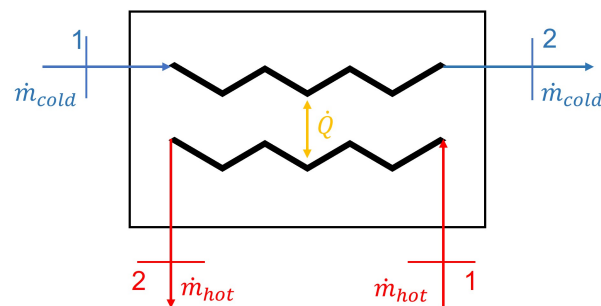


Figure D.3: Heat exchanger block diagram

A heat exchanger has been categorised as a purely heat interacting device, so no work transfer is considered across a HEX. Now applying the steady state mass and energy Equation D.4 across the HEX block, and ignoring the K.E and P.E effects, it gives:

$$\dot{m}_{cold} (h_2 - h_1) = \dot{Q}, \quad \text{system gaining heat} \quad (\text{D.5})$$

$$\dot{m}_{hot} (h_1 - h_2) = \dot{Q}, \quad \text{system rejecting heat.} \quad (\text{D.6})$$

2. Turbomachines:

Consider a turbomachine block as shown in Figure D.4.

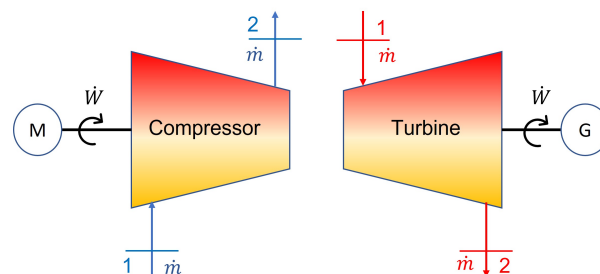


Figure D.4: Compressor and turbine block diagram

A turbomachine has been characterised as a purely work interacting device and thus an adiabatic model will be applied to a turbomachine. So, applying the steady state mass and energy Equation

(D.4) across the turbomachine block, and ignoring the K.E and P.E effects, it gives:

$$\dot{m} (h_2 - h_1) = \dot{W}, \quad \text{system absorbing work: compressor, pump} \quad (\text{D.7})$$

$$\dot{m} (h_1 - h_2) = \dot{W}, \quad \text{system producing work: turbine.} \quad (\text{D.8})$$

Further, turbomachines have been subjected to isentropic efficiencies to account for the irreversible nature of compression or expansion:

$$\eta_{is,comp} = \frac{\dot{W}_{is}}{\dot{W}} = \frac{h_{2,is} - h_1}{h_2 - h_1}, \quad (\text{D.9})$$

$$\eta_{is,turb} = \frac{\dot{W}}{\dot{W}_{is}} = \frac{h_1 - h_2}{h_1 - h_{2,is}}. \quad (\text{D.10})$$

3. Expansion Valve:

Consider the diagram of an expansion valve as shown in Figure D.5.

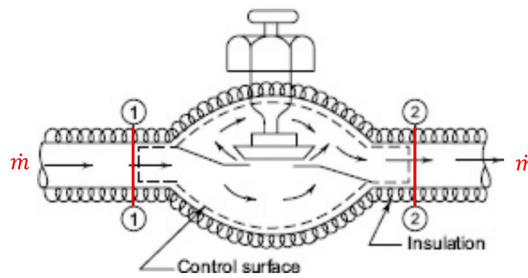


Figure D.5: Flow through an expansion valve

The expansion valve has been categorised as an adiabatic device with no work interaction with the surrounding, so no work and heat transfer is considered across an expansion valve. This leads the steady flow energy Equation D.4 to the following relation, while neglecting the changes in K.E and P.E,

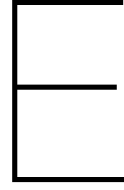
$$h_1 = h_2 \quad (\text{D.11})$$

which is termed as an isenthalpic process.

PCMs	T_m	Δh_m	λ_a	λ_l	$C_{p,s}$	$C_{p,l}$	ρ_l	$\Delta V/V_s$
	(°C)	(J·g ⁻¹)	(W·m ⁻¹ ·K ⁻¹)		(J·g ⁻¹ ·K ⁻¹)		(g·cm ⁻³)	(%)
Ice and salt hydrates								
H ₂ O	0	334	2.3	0.56	2.10	4.22	1.00	-8.3
KF 4H ₂ O	19	230	n/a*	n/a	1.8	2.4	1.46	n/a
CaCl ₂ 6H ₂ O	30	180	1.1	0.5	1.4	2.1-2.3	1.56	13
Na ₂ SO ₄ 10H ₂ O	32	250	0.5	n/a	1.9	3.3	1.41	4
Na ₂ HPO ₄ 12H ₂ O	35	280	0.5	0.5	1.5-1.7	2.0-3.2	1.44	5
Na(CH ₃ COO) 3H ₂ O	58	250	0.7	0.4	2.1	3.0	1.28	13
Pure metals								
Na	98	113	122	87	1.36	1.38	0.93	2.8
Zn	419	112	100	50	0.45	0.48	6.76	1.9
Al	660	397	211	91	1.18	1.18	2.38	7.5
Anhydrous salts and their mixtures (composition in wt. %)								
KNO ₃ -LiNO ₃ (67-33)	133	170	n/a	n/a	n/a	n/a	1.9	14
KNO ₃ -NaNO ₂ -NaNO ₃ (53-40-7)	142	80	0.5	0.5	1.3	1.6	1.98	4
LiNO ₃ -NaNO ₃ (49-51)	194	265	n/a	0.5	n/a	n/a	1.9	13
KNO ₃ -NaNO ₃ (54-46)	222	100	n/a	0.5	1.4	1.5	1.95	5
LiNO ₃	254	360	1.4	0.6	1.8	1.6-2.0	1.78	22
NaNO ₂	270	180	0.7-1.3	0.5-0.7	n/a	1.6-1.8	1.81	17
NaNO ₃	306	175	0.6	0.51	1.66	1.66	1.91	11
NaOH	322	210	0.9	0.8	2.0	2.1	2.13	16
KNO ₃	337	100	n/a	0.4-0.5	1.4	1.3-1.4	1.87-1.89	3
NaCl-KCl-MgCl ₂ (24.5-20.5-55)	393	240	1.0	n.a	1.0	1.0	1.8	n/a
K ₂ CO ₃ -Li ₂ CO ₃ -Na ₂ CO ₃ (35-32-33)	397	275	n/a	n/a	1.7	1.6	1.90	17
K ₂ CO ₃ -Li ₂ CO ₃ (65-35)	505	345	n/a	n/a	1.3-1.8	1.8-2.3	1.96	10

* n/a = not available.

Figure D.6: Thermophysical properties of phase change materials



Heat Exchanger Design

The general heat exchanger design procedure for heat exchangers is discussed as follows:

Step 1: Specification and Duty

The first step begins with defining the HEX duty/heat load, process streams inlet-outlet conditions, mass flow rates and specific heat capacity of individual streams. This also includes evaluating any unknown process condition, which can be estimated from Equation (E.1).

$$Q = \dot{m}c_p (T_{hot,in} - T_{hot,out}) = \dot{m}c_p (T_{cold,out} - T_{cold,in}). \quad (E.1)$$

Step 2: Collection of physical properties

The subsequent step involves gathering all pertinent physical characteristics of the streams at appropriate pressures and temperatures. It is necessary to determine properties such as the specific heat, thermal conductivity, density, and viscosity at both the inlet and outlet conditions. The REFPROP tool has been used to evaluate all the thermo-physical properties of the process streams [56].

Step 3: Assume an overall heat transfer coefficient U_0

Next, an overall heat transfer coefficient U_0 is assumed. The assumption is based on the properties of the process streams and the type of heat exchanger used. The typical values can be found from standard heat exchanger books such as Sinnott and Towler, & Kern [81, 37].

Step 4: Calculate the logarithmic mean temperature difference ΔT_m

The Log Mean Temperature Difference (ΔT_m) gives an estimate of the effective driving force in a heat exchanger and can be calculated from Equation (E.2). The subscripts correspond to Figure 2.25.

$$\Delta T_m = \frac{(T_{h,in} - T_{c,out}) - (T_{h,out} - T_{c,in})}{\ln\left(\frac{T_{h,in} - T_{c,out}}{T_{h,out} - T_{c,in}}\right)}. \quad (E.2)$$

LMTD is purely dependent on the process fluid operating conditions at the inlet and outlet of a heat exchanger. The *LMTD* calculated in Equation (E.2) is for a pure counter-current flow, however the actual flow path in heat exchangers is never 100% counter-current. In order to consider the effect of deviation from counter-current condition, an additional correction factor (F) is applied to the *LMTD* calculated from Equation (2.13). The overall heat load of a heat exchanger can then be written as:

$$Q = U_0 A (F \Delta T_m). \quad (E.3)$$

Step 5: Calculate the heat transfer area

Based on the assumed overall heat transfer coefficient U_0 and corrected LMTD, the heat transfer area can be evaluated from Equation (E.4).

$$A = \frac{Q}{U_0 F \Delta T_m} \quad (\text{E.4})$$

The area calculated above is highly dependent of the U_0 value. The final overall heat transfer coefficient U_0 can then be estimated based on individual heat transfer coefficients of hot and cold fluid, fouling factors. This is done by the sum of the individual resistances. For shell and tube heat exchanger the U_0 is calculated from Equation (E.5).

$$\frac{1}{U_0} = \frac{1}{\alpha_s} + \frac{1}{\alpha_{f,s}} + \frac{d_o \ln\left(\frac{d_o}{d_i}\right)}{2\lambda_w} + \frac{d_o}{d_i} \frac{1}{\alpha_{f,t}} + \frac{d_o}{d_i} \frac{1}{\alpha_t}. \quad (\text{E.5})$$

For plate heat exchanger the U_0 is calculated from Equation (E.6).

$$\frac{1}{U} = \frac{1}{\alpha_h} + \frac{1}{\alpha_{f,h}} + \frac{t_p}{\lambda_p} + \frac{1}{\alpha_c} + \frac{1}{\alpha_{f,c}}. \quad (\text{E.6})$$

The further steps for each heat exchanger is different and is included in the individual sections.

E.1. Shell and Tube HEX

The further steps for the design of Shell and Tube HEX are as follows:

Step 6: Decide HEX model, tube size, material layout and fluid allocation

This step is necessary to determine the layout of the HEX. Further the fluid allocation criteria has been explained in detail in Chapter 2.6.1. The tube size and material selection is done based on the standard charts available in Sinnott and Towler [81].

Step 7: Calculate number of tubes

The total number of tubes (N_t) is determined by dividing the total area of the exchanger by the area of a single tube (A_t), as given in Equation (E.7).

$$N_t = \frac{A}{A_t}, \quad \text{where } A_t = d_o \pi L \quad (\text{E.7})$$

where d_o , L is the outside diameter and length of a tube respectively. The designer has the choice of fixing the number of tube passes ($N_{p,t}$). A high number of tube pass results in a higher pressure drop. However it also plays a role in increasing the fluid velocity, in case, overall mass flow is less. The tube side velocity u_t can be calculated using Equation (E.8).

$$u_t = \frac{\dot{m}}{N_{p,t} \rho_t \left(\frac{\pi}{4} d_i^2\right)} \quad (\text{E.8})$$

where, \dot{m} , d_i , ρ_t is the total mass flow rate, inside diameter of the tube and density of the fluid at tube side respectively.

Step 8: Calculate bundle and shell diameter

The bundle's diameter is influenced by the number of tubes, tube passes, and configuration of the tubes. Constants K_1 and n_1 that are obtained from typical tube layouts are used to gauge the bundle diameter d_b . It is given by the empirical relation in Equation (E.9).

$$d_b = d_o \left(\frac{N_t}{K_1}\right)^{\frac{1}{n_1}} \quad (\text{E.9})$$

The Values of these constants are taken from Sinnott and Towler [81]. Further, the shell diameter is chosen based on a standard clearance with the bundle diameter.

Step 9: Calculate tube side pressure drop and heat transfer coefficient

The main sources of pressure drop within a tube of a S&T HEX are the frictional losses through the span of the tube length and the sudden expansion, contraction, and flow reversal losses considering the tube arrangement. The combined effect of these losses has been formulated and developed by Frank (1978) and is presented in Sinnott & Towler [81], which is stated here as follows:

$$\Delta P_t = N_p \left[8j_f \left(\frac{L}{d_i} \right) \left(\frac{\mu}{\mu_w} \right)^{-m} + 2.5 \right] \frac{\rho u_t^2}{2} \quad (\text{E.10})$$

$$m = 0.25; \quad \text{for laminar flow, } \text{Re} < 2100$$

$$= 0.14; \quad \text{for turbulent flow, } \text{Re} > 2100$$

where, ΔP_t is the tube side pressure drop (N/m^2), N_p is the number of tube passes, L is the length of a single tube (m), d_i is the inside diameter of the tube (m), u_t is the tube side velocity (m/s), μ is the fluid viscosity at the bulk fluid temperature (Ns/m^2), μ_w is fluid viscosity at the wall temperature, and j_f is the tube side dimensionless friction factor and is a function of Reynolds number (Re). The value of j_f can be read from the Figure shown in E.1 against the calculated Re .

Similar to friction factor in the pressure drop relation, Equation (E.10), the heat transfer data has been correlated to a heat transfer factor (j_h , which allows to evaluate heat transfer coefficients for laminar and turbulent flows through a single Equation (E.11).

$$\alpha_t = j_h \text{RePr}^{0.33} \left(\frac{\mu}{\mu_w} \right)^{0.14} \frac{\lambda_f}{d_i} \quad (\text{E.11})$$

where, j_h can be read from the Figure E.2. λ_f is the thermal conductivity of the fluid within the tube.

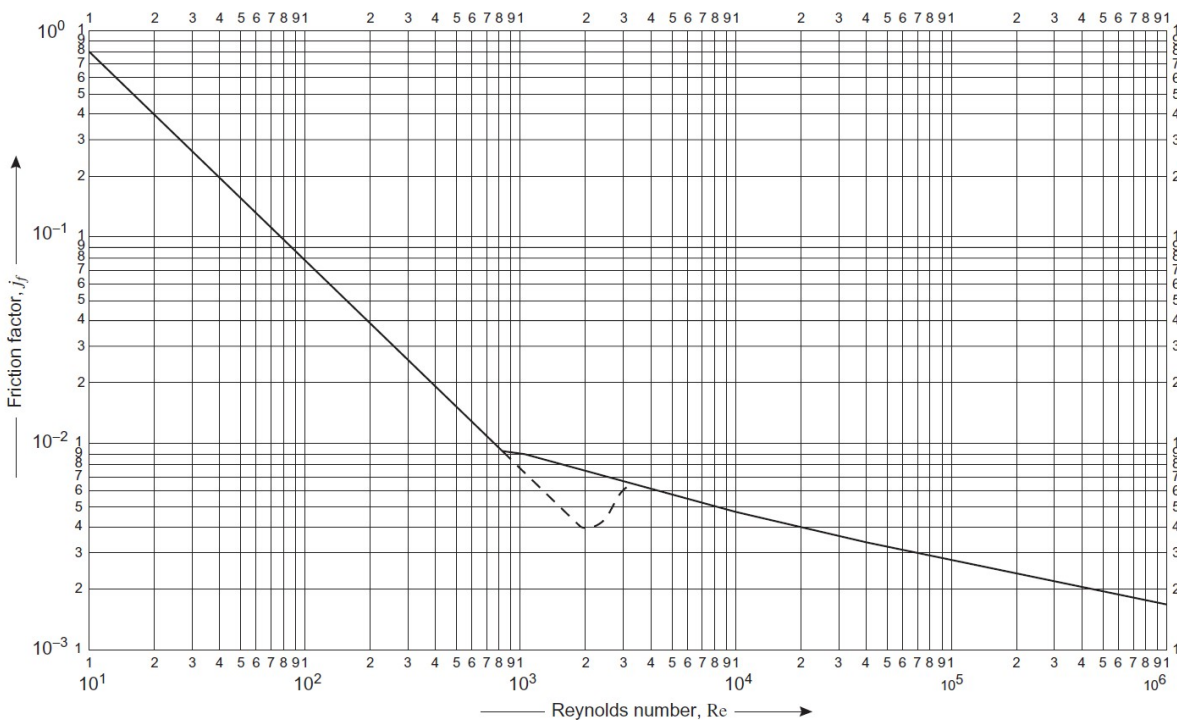


Figure E.1: Tube side friction factors

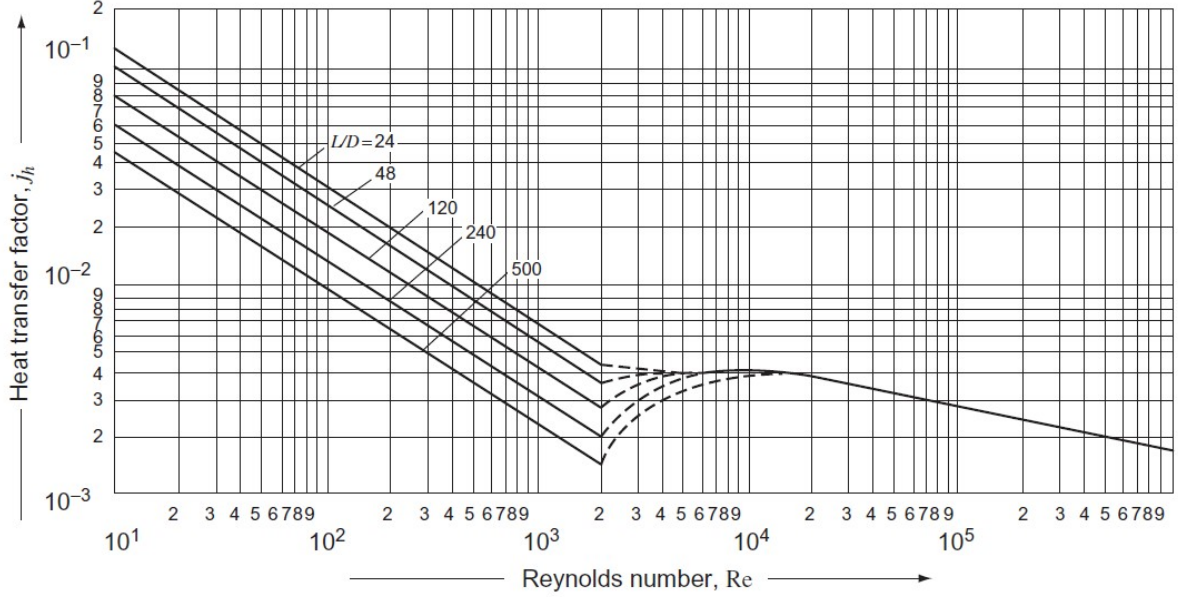


Figure E.2: Tube side heat transfer factors

Step 10: Calculate shell side pressure drop and heat transfer coefficient

Similar to tube side correlations, the shell side pressure drop and heat transfer relations are also based on friction and heat transfer factors respectively. These are based on the method developed by Kern and collected in Sinnott and Towler [81]. The correlations for pressure drop and heat transfer are given in Equation (E.12), and (E.13).

$$\Delta P_s = 8j_f \left(\frac{D_s}{d_e} \right) \left(\frac{L}{l_B} \right) \frac{\rho u_s^2}{2} \left(\frac{\mu}{\mu_w} \right)^{-0.14} \quad (\text{E.12})$$

$$\alpha_s = j_h Re Pr^{0.33} \left(\frac{\mu}{\mu_w} \right)^{0.14} \frac{\lambda_f}{d_e} \quad (\text{E.13})$$

where, j_f and j_h can be read from the Figures E.3 and E.4 respectively. Re represents the Reynolds number for the flow on the shell side and is calculated using the Equation (E.14). The term d_e is the hydraulic diameter of the shell and is estimated using relation Equation (E.15).

$$Re = \frac{\rho u_s d_e}{\mu} \quad (\text{E.14})$$

$$d_e = \frac{1.27}{d_o} (p_t^2 - 0.785 d_o^2) \quad (\text{E.15})$$

$$u_s = \frac{G_s}{\rho} \quad (\text{E.16})$$

$$G_s = \frac{\dot{m}_s}{A_s} \quad (\text{E.17})$$

$$A_s = \frac{(p_t - d_o) D_s l_B}{p_t} \quad (\text{E.18})$$

where, D_s is the shell diameter, \dot{m}_s is the mass flow rate of fluid on shell side, u_s is the shell velocity, p_t is the pitch of the tube arrangement, G_s is mass flux, and A_s is the cross flow area.

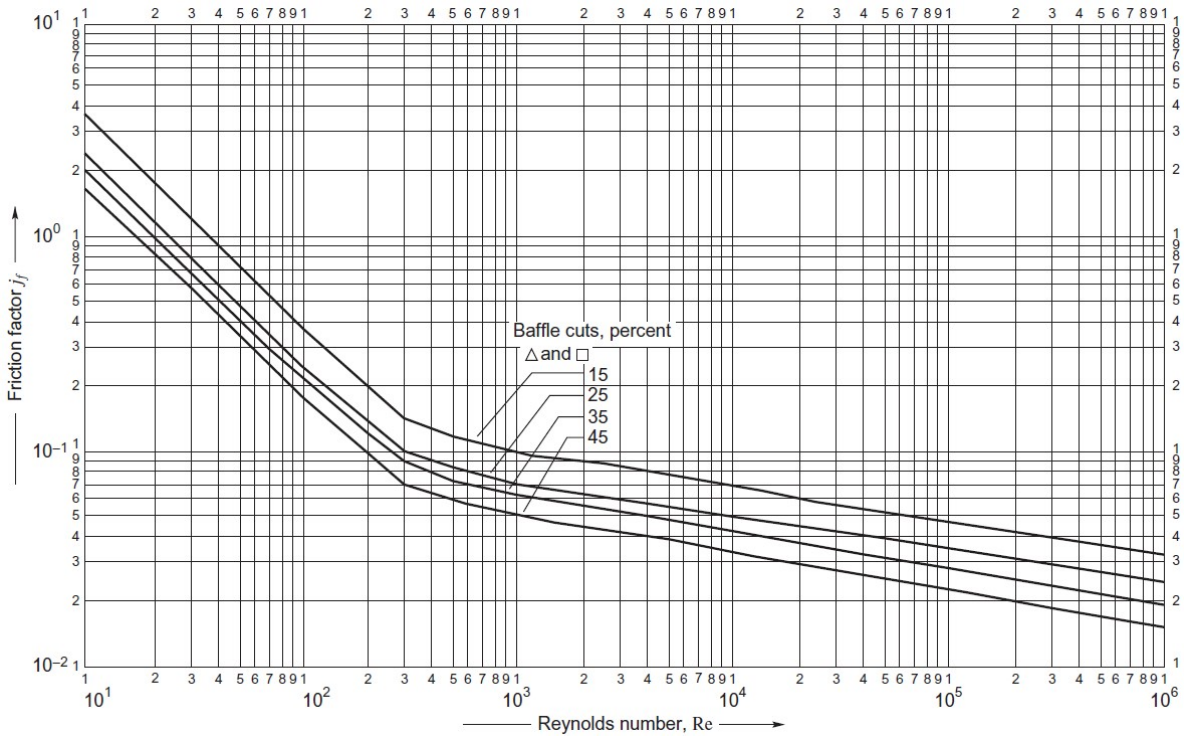


Figure E.3: Shell side friction factors

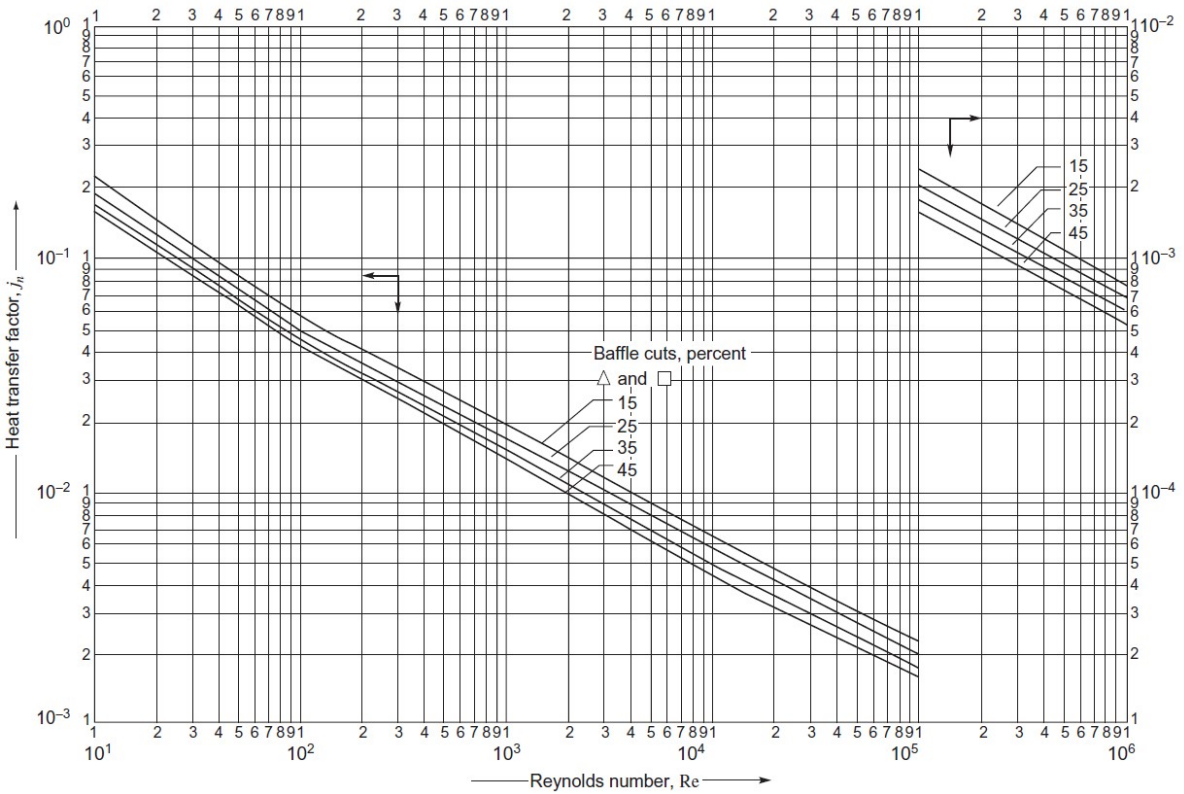


Figure E.4: Shell side heat transfer factors

E.2. Plate Hex

Step 7-9: Geometric design specifications

The plate dimensions are selected from the standard catalogue. Some standard plate dimensions have been given in Sinnott and Towler [81]. The total number of plates, however, can be calculated from the a single plate area as given in Equation (E.19).

$$N_p = \frac{A}{A_p}, \quad (\text{E.19})$$

$$A_p = \phi L_p B_p. \quad (\text{E.20})$$

Where, ϕ is the coefficient for corrugated plates and is taken 1.22. The designer has the choice to fix the number of passes. Generally, it is kept 1-1 pass. So, total number of effective plates excluding the front and rear plate are $N_p - 2$. This leads to estimating number of fluid channels ($N_{c,pass}$) per pass as $\frac{N_p - 1}{2}$. The channel velocity can be calculated using Equation (E.21)

$$u_p = \frac{\dot{m}}{N_{c,pass} \rho t_g B_p} \quad (\text{E.21})$$

Where, \dot{m} is the total mass flow of the fluid through the plate HEX, t_g is the channel width/gap, B_p is the channel length or width of the plate.

Step 10-11: Calculate the film heat-transfer coefficients for each stream

The heat transfer coefficient for a fluid stream is calculated using the Nusselt's number as follows:

$$\alpha = \frac{N_u \lambda}{d_e}. \quad (\text{E.22})$$

where, λ is the thermal conductivity of the fluid. In literature, the researchers have provided a number of correlations for Nusselt number with different validation ranges. One of the standard correlation of Nusselt number for single phase operation is provided in Sinnott and Towler [81], formulated as:

$$N_u = 0.26 Re^{0.65} Pr^{0.4}. \quad (\text{E.23})$$

which is valid for a turbulent flow across a typical plate. Another correlation much more efficient as compared to other correlations is provided by Infante Ferreira is formulated as follows:

$$Nu_{sp} = \frac{\alpha_{sp} d_e}{\lambda} = 0.275 Re^{0.7} Pr^{1/3}; \quad 320 \leq Re \leq 2600 \quad (\text{E.24})$$

Step 12: Calculate the overall heat transfer coefficient

The overall heat transfer coefficient of the plate heat exchanger is calculated using Equation (E.6). The fouling factors for the streams have been taken from standard HEX books [81, 37].

Step 13: Check the pressure drop for each stream

The total pressure drop for a fluid stream in a plate heat exchanger is a result of frictional pressure loss across plates and in the main conduit while expansion and contraction losses across the exit and inlet ports respectively.

$$\Delta P = \Delta P_{plate} + \Delta P_{conduit} + \Delta P_{ports}, \quad (\text{E.25})$$

$$\Delta P_{conduit} = 8j_f \left(\frac{L_p}{d_e} \right) \frac{\rho W_{pt}^2}{2}, \quad (\text{E.26})$$

$$\Delta P_{ports} = 1.3 \frac{\rho W_{pt}^2}{2} N_{pass} \quad (\text{E.27})$$

where, j_f is the friction factor in the conduit and is approximated by $j_f = 0.6Re^{-0.3}$. The terms $w_p t$, L_p , d_e , and N_{pass} corresponds to the fluid velocity in the conduit/port, path length, hydraulic diameter of the conduit and number of passes respectively.

The friction factor (ξ) correlation for a single phase flow in a plate HEX is taken from VDI Heat Atlas [43] and is defined across the plate, which is formulated as follows:

$$\Delta p_{plate} = \xi \left(\frac{1}{2} \rho w_p^2 \right) \frac{L_p}{d_e}, \quad (E.28)$$

$$\frac{1}{\sqrt{\xi}} = \frac{\cos\phi}{\sqrt{0.18 \tan\phi + 0.36 \sin\phi + \xi_0 / \cos\phi}} + \frac{1 - \cos\phi}{\sqrt{3.8 \xi_1}}, \quad (E.29)$$

$$\xi_0 = \frac{64}{Re}; \quad \xi_1 = \frac{597}{Re} + 3.85, \quad Re < 2000, \quad (E.30)$$

$$\xi_0 = (1.8 \ln Re - 1.5)^{-2}; \quad \xi_1 = \frac{39}{Re^{0.289}}, \quad Re \geq 2000. \quad (E.31)$$

where, w_p , L_p , d_e corresponds to the plate channel velocity, plate length, and hydraulic diameter of the channel. Greek letter ϕ corresponds to the corrugation angle on the plate ($0^\circ < \phi < 90^\circ$). ξ_0 , and ξ_1 represents the friction factor for the smooth longitudinal flow ($\phi = 0^\circ$), and wavy longitudinal flow ($\phi = 90^\circ$) and are a function of Reynolds number (Re).

E.3. Widom Line

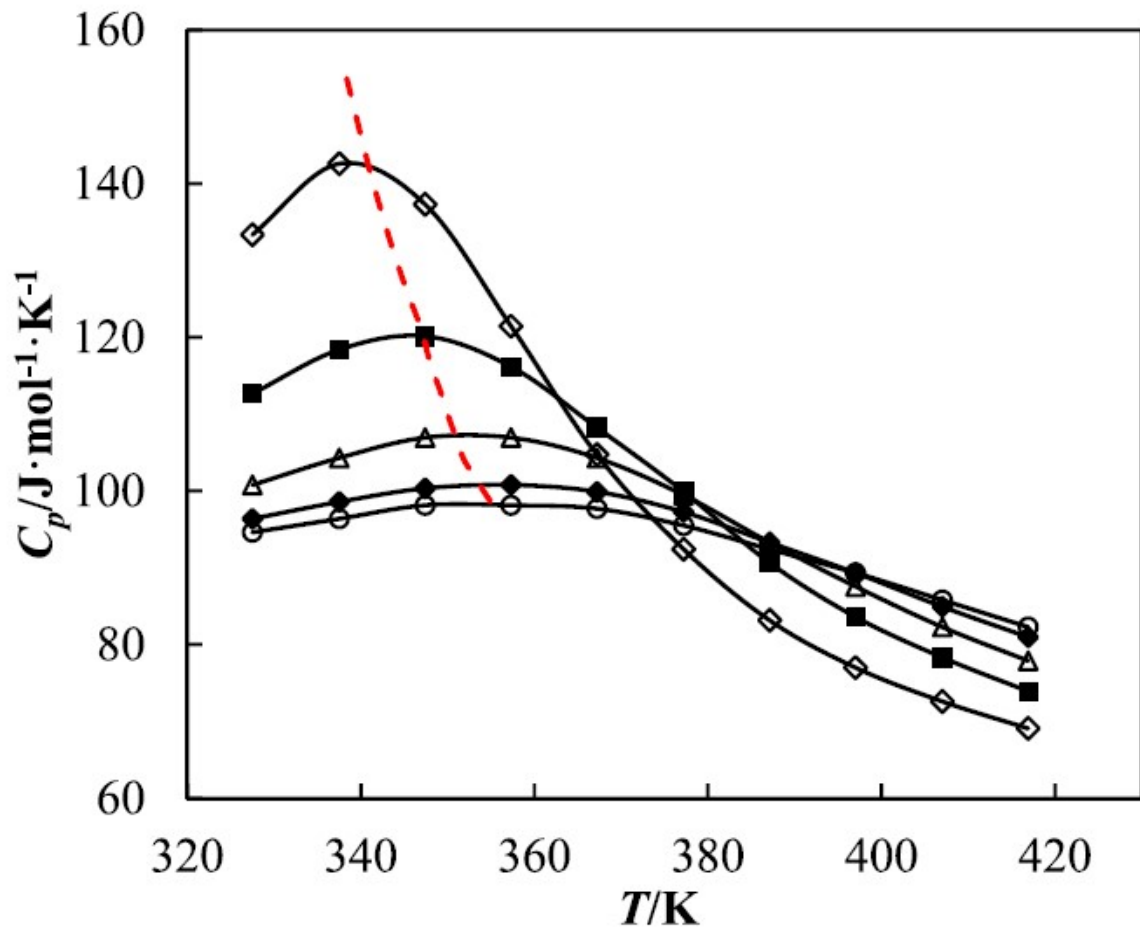


Figure E.5: Widom line for CO_2 from experimental calculations [93].

Bibliography

- [1] DURATHERM Heat Transfer Fluids. URL: <https://durathermfluids.com/products/duratherm-hf/>.
- [2] China Energy Storage Alliance (CNESA). *CNESA Global Energy Storage Market Analysis – 2020.Q1*. 2020. URL: <http://en.cnesa.org/latest-news/2020/5/28/cnesa-global-energy-storage-market-analysis-2020q1-summary>.
- [3] Michael Adewumi. *Principle of Corresponding States*. PennState College of Earth & Mineral Sciences. URL: https://www.e-education.psu.edu/png520/m8_p2.html.
- [4] Vipluv AGA et al. 'Supercritical CO₂-Based Heat Pump Cycle for Electrical Energy Storage for Utility Scale Dispatchable Renewable Energy Power Plants'. In: (2016). URL: <http://sco2symposium.com/papers2016/Thermal/094paper.pdf>.
- [5] Roberto Agromayor and Lars Nord. 'Preliminary Design and Optimization of Axial Turbines Accounting for Diffuser Performance'. In: *International Journal of Turbomachinery, Propulsion and Power* 4 (Sept. 2019), p. 32. DOI: [10.3390/ijtp4030032](https://doi.org/10.3390/ijtp4030032).
- [6] G Angelino and C Invernizzi. *Prospects for real-gas reversed Brayton cycle heat pumps*. May, 1995. DOI: [10.1016/0140-7007\(95\)00005-V](https://doi.org/10.1016/0140-7007(95)00005-V).
- [7] O. E. Baljé. 'A Study on Design Criteria and Matching of Turbomachines: Part A—Similarity Relations and Design Criteria of Turbines'. In: *Journal of Engineering for Power* 84 (1962), pp. 83–102.
- [8] O. E. Baljé. 'A Study on Design Criteria and Matching of Turbomachines: Part B—Compressor and Pump Performance and Matching of Turbocomponents'. In: *Journal of Engineering for Power* 84 (1962), pp. 103–114.
- [9] J. Barnes et al. 'Characterisation of Molten Salts for Application in Molten Salt Reactors'. In: *Energy Science & Technology* (2019). URL: <https://doi.org/10.5130/pamr.v6i10.1546>.
- [10] Leslie Beck. 'What is 'smoke point' and does it matter when cooking with oil?' In: *The Globe and Mail* (July 20, 2022). URL: <https://www.theglobeandmail.com/life/health-and-fitness/health/smoke-point-matters-in-cooking-with-oil/article26569060/>.
- [11] Ian H. Bell et al. 'Pure and Pseudo-pure Fluid Thermophysical Property Evaluation and the Open-Source Thermophysical Property Library CoolProp'. In: *Industrial & Engineering Chemistry Research* 53.6 (2014), pp. 2498–2508. DOI: [10.1021/ie4033999](https://doi.org/10.1021/ie4033999).
- [12] Alberto Benato. 'Performance and cost evaluation of an innovative Pumped Thermal Electricity Storage power system'. In: *Energy* 138 (2017), pp. 419–436. ISSN: 0360-5442. DOI: <https://doi.org/10.1016/j.energy.2017.07.066>.
- [13] Thomas Bowen et al. *USAID Grid-Scale Energy Storage Technologies Primer*. 2021. URL: <https://www.nrel.gov/docs/fy21osti/76097.pdf>.
- [14] Meherwan P. Boyce. *Axial Flow Compressors*. URL: <https://www.netl.doe.gov/sites/default/files/gas-turbine-handbook/2-0.pdf>.
- [15] R P Cahn. 'Thermal energy storage by means of reversible heat pumping'. In: (May 1978). URL: <https://www.osti.gov/biblio/6899536>.
- [16] R P Cahn. *Thermal energy storage by means of reversible heat pumping*. U.S. Patent US4089744, May 1978. URL: <https://worldwide.espacenet.com/patent/search?q=pn%3DUS4089744A>.
- [17] A. Carro et al. 'Energy storage system based on transcritical CO₂ cycles and geological storage'. In: *Applied Thermal Engineering* 193 (2021), p. 116813. ISSN: 1359-4311. DOI: <https://doi.org/10.1016/j.applthermaleng.2021.116813>.
- [18] Emmanuel Cayer et al. 'Analysis of a carbon dioxide transcritical power cycle using a low temperature source'. In: *Applied Energy* 86.7 (2009), pp. 1055–1063. ISSN: 0306-2619. DOI: <https://doi.org/10.1016/j.apenergy.2008.09.018>.
- [19] R. Chacartegui et al. 'Alternative cycles based on carbon dioxide for central receiver solar power plants'. In: *Applied Thermal Engineering* 31.5 (2011), pp. 872–879. ISSN: 1359-4311. DOI: <https://doi.org/10.1016/j.applthermaleng.2010.11.008>.

- [20] Huijuan Chen, D. Yogi Goswami, and Elias K. Stefanakos. 'A review of thermodynamic cycles and working fluids for the conversion of low-grade heat'. In: *Renewable and Sustainable Energy Reviews* 14.9 (2010), pp. 3059–3067. ISSN: 1364-0321. DOI: <https://doi.org/10.1016/j.rser.2010.07.006>.
- [21] *Compressed Heat Energy Storage for Energy from Renewable sources*. URL: https://www.chester-project.eu/wp-content/uploads/2019/01/CHESTER_D2.2.pdf.
- [22] TMI Staff & Contributors. 'AXIAL AND RADIAL TURBINES'. In: *Turbomachinery International* (November 1, 2012). URL: <https://www.turbomachinerymag.com/view/axial-and-radial-turbines-2>.
- [23] LDES Council. *Net-zero power: Long duration energy storage for a renewable grid*. McKinsey & Company. URL: <https://www.mckinsey.com/business-functions/sustainability/our-insights/net-zero-power-long-duration-energy-storage-for-a-renewable-grid>.
- [24] T. Desrues et al. 'A thermal energy storage process for large scale electric applications'. In: *Applied Thermal Engineering* 30.5 (2010), pp. 425–432. ISSN: 1359-4311. DOI: <https://doi.org/10.1016/j.applthermaleng.2009.10.002>.
- [25] G. Di Marcoberardino, E. Morosini, and G. Manzolini. 'Preliminary investigation of the influence of equations of state on the performance of CO₂ + C₆F₆ as innovative working fluid in transcritical cycles'. In: *Energy* 238 (2022), p. 121815. ISSN: 0360-5442. DOI: <https://doi.org/10.1016/j.energy.2021.121815>.
- [26] G. Di Marcoberardino et al. 'Experimental characterisation of CO₂ + C₆F₆ mixture: Thermal stability and vapour liquid equilibrium test for its application in transcritical power cycle'. In: *Applied Thermal Engineering* 212 (2022), p. 118520. ISSN: 1359-4311. DOI: <https://doi.org/10.1016/j.applthermaleng.2022.118520>.
- [27] G. Di Marcoberardino et al. 'Thermal efficiency gains enabled by using CO₂ mixtures in supercritical power cycles'. In: *Energy* 238 (2022), p. 121899. ISSN: 0360-5442. DOI: <https://doi.org/10.1016/j.energy.2021.121899>.
- [28] Gioele Di Marcoberardino et al. 'Investigation of CO₂ mixtures to overcome the limits of sCO₂ cycles'. In: *76th Italian National Congress ATI (ATI 2021)*. Vol. 312. 2021, pp. 08010–08019. URL: <https://re.public.polimi.it/handle/11311/1190354>.
- [29] Jasper van Dijk. *Industrial Waste Heat Recovery: Save Energy and reduce costs*. July 2022. URL: <https://joaairsolutions.com/industrial-waste-heat-recovery-save-energy-reduce-costs/>.
- [30] O. Dumont and V. Lemort. 'Mapping of performance of pumped thermal energy storage (Carnot battery) using waste heat recovery'. In: *Energy* 211 (2020), p. 118963. ISSN: 0360-5442. DOI: <https://doi.org/10.1016/j.energy.2020.118963>.
- [31] Olivier Dumont et al. 'Carnot battery technology: A state-of-the-art review'. In: *Journal of Energy Storage* 32 ((2020)), p. 101756. ISSN: 2352-152X. DOI: <https://doi.org/10.1016/j.est.2020.101756>.
- [32] Hans-Peter Ebert et al. 'Thermophysical properties of a volcanic rock material'. In: *High Temperatures-high Pressures - HIGH TEMP-HIGH PRESS* 34 (Jan. 2002), pp. 561–568. DOI: [10.1068/htjr058](https://doi.org/10.1068/htjr058).
- [33] Tom Evertse. *The design of an innovative hydrogen-oxygen power system based upon a solid oxide fuel cell and an advanced thermodynamic cycle*. Delft University of Technology, 2021.
- [34] Sebastian Eyerer et al. 'Experimental investigation of modern ORC working fluids R1224yd(Z) and R1233zd(E) as replacements for R245fa'. In: *Applied Energy* 240 (2019), pp. 946–963. ISSN: 0306-2619. DOI: <https://doi.org/10.1016/j.apenergy.2019.02.086>. URL: <https://www.sciencedirect.com/science/article/pii/S0306261919303861>.
- [35] O.O. Fasina and Z. Colley. 'Viscosity and Specific Heat of Vegetable Oils as a Function of Temperature: 35°C to 180°C'. In: *International Journal of Food Properties* 11.4 (2008), pp. 738–746. DOI: [10.1080/10942910701586273](https://doi.org/10.1080/10942910701586273). URL: <https://doi.org/10.1080/10942910701586273>.
- [36] Helder Lopes Ferreira et al. 'Characterisation of electrical energy storage technologies'. In: *Energy* 53 (2013), pp. 288–298. ISSN: 0360-5442. DOI: <https://doi.org/10.1016/j.energy.2013.02.037>.
- [37] Ann Marie Flynn, Toshihiro Akashige, and Louis Theodore. 'Chapter 7 - Shell-and-Tube Heat Exchangers'. In: *Kern's Process Heat Transfer (Second Edition)*. 2019. ISBN: 978-1-119-36364-4.
- [38] Guido Francesco Frate, Lorenzo Ferrari, and Umberto Desideri. 'Rankine Carnot Batteries with the Integration of Thermal Energy Sources: A Review'. In: *Energies* 13.18 (2020). ISSN: 1996-1073. DOI: [10.3390/en13184766](https://doi.org/10.3390/en13184766). URL: <https://www.mdpi.com/1996-1073/13/18/4766>.
- [39] Tobias Funke et al. 'Utilization of Waste Heat in the Data Center'. In: *A white paper by NeRZ in collaboration with eco – Association of the Internet Industry* (). URL: <https://international.eco.de/topics/datacenter/white-paper-utilization-of-waste-heat-in-the-data-center/#download>.

- [40] Marco Gambini and Michela Vellini. 'Fundamentals of Thermodynamics and Fluid Dynamics of Turbomachinery'. In: Springer International Publishing, Sept. 2020. DOI: [10.1007/978-3-030-51299-6_2](https://doi.org/10.1007/978-3-030-51299-6_2).
- [41] J.R. García-Cascales et al. 'Assessment of boiling and condensation heat transfer correlations in the modelling of plate heat exchangers'. In: *International Journal of Refrigeration* 30.6 (2007), pp. 1029–1041. ISSN: 0140-7007. DOI: <https://doi.org/10.1016/j.ijrefrig.2007.01.004>.
- [42] Jessica Gavin. *Smoke Points of Cooking Oils*. 2018. URL: <https://www.jessicagavin.com/smoke-points-cooking-oils/>.
- [43] VDI Gesellschaft. *VDI Heat Atlas*. VDI-Buch. Springer Berlin Heidelberg, 2010. ISBN: 9783540778769. URL: <https://books.google.nl/books?id=0t-HrUflaHEC>.
- [44] Dolf Gielen. *GLOBAL ENERGY TRANSFORMATION - a roadmap to 2050*. Apr. 2018.
- [45] Maria A. Grompone. 'Sunflower oil'. In: *Vegetable Oils in Food Technology*. Blackwell Publishing Ltd., Mar. 2011. ISBN: 9781444339925. DOI: [10.1002/9781444339925](https://doi.org/10.1002/9781444339925).
- [46] Said Hagrey, Daniel Köhn, and Wolfgang Rabbel. 'Geophysical assessments of renewable gas energy compressed in geologic pore storage reservoirs'. In: *SpringerPlus* 3 (May 2014), p. 267. DOI: [10.1186/2193-1801-3-267](https://doi.org/10.1186/2193-1801-3-267).
- [47] Dr. Tim Held. *Supercritical CO₂-Based Long-Duration Electrical Energy Storage Technical Overview*. ECHOGEN power systems. URL: https://www.echogen.com/_CE/pagecontent/Documents/Echogen-Technical%20Overview%207.18.19-3.pdf.
- [48] J. D. Hunter. 'Matplotlib: A 2D graphics environment'. In: *Computing in Science & Engineering* 9.3 (2007), pp. 90–95. DOI: [10.1109/MCSE.2007.55](https://doi.org/10.1109/MCSE.2007.55).
- [49] Henning Jockenhöfer, Wolf-Dieter Steinmann, and Dan Bauer. 'Detailed numerical investigation of a pumped thermal energy storage with low temperature heat integration'. In: *Energy* 145 (2018), pp. 665–676. ISSN: 0360-5442. DOI: <https://doi.org/10.1016/j.energy.2017.12.087>.
- [50] FREDRIK JONSSON and ANDREA MILJANOVIC. *UTILIZATION OF WASTE HEAT FROM HYDROGEN PRODUCTION*. Mälardalen University, June 2022.
- [51] A. Landelle et al. 'Experimental Investigation of a Transcritical Organic Rankine Cycle with Scroll Expander for Low—Temperature Waste Heat Recovery'. In: *Energy Procedia* 129 (2017), pp. 810–817. ISSN: 1876-6102. DOI: <https://doi.org/10.1016/j.egypro.2017.09.142>.
- [52] Michael Langan and Kevin O'Toole. 'A new technology for cost effective low grade waste heat recovery'. In: *Energy Procedia* 123 (2017), pp. 188–195. ISSN: 1876-6102. DOI: <https://doi.org/10.1016/j.egypro.2017.07.261>. URL: <https://www.sciencedirect.com/science/article/pii/S1876610217328357>.
- [53] Robert B. Laughlin. 'Pumped thermal grid storage with heat exchange'. In: *J. Renewable Sustainable Energy* 9 (2017). DOI: <https://doi.org/10.1063/1.4994054>.
- [54] Anaa Lavaa. 'The Differences Between Axial Compressor & Centrifugal Compressor'. In: *Industrial Manufacturing Blog | linqip* (June 16, 2021). URL: <https://www.linqip.com/blog/differences-between-axial-compressor-centrifugal/>.
- [55] Florine Le Coultre. *Utilisation of Heat Released During the Production of Green Hydrogen Using Alkaline Electrolysis*. Delft University of Technology, June 2022.
- [56] E. W. Lemmon et al. *NIST Standard Reference Database 23: Reference Fluid Thermodynamic and Transport Properties-REFPROP, Version 10.0*, National Institute of Standards and Technology. 2018. DOI: <https://doi.org/10.18434/T4/1502528>.
- [57] Eric W. Lemmon and Reiner Tillner-Roth. 'A Helmholtz energy equation of state for calculating the thermodynamic properties of fluid mixtures'. In: *Fluid Phase Equilibria* 165.1 (1999), pp. 1–21. ISSN: 0378-3812. DOI: [https://doi.org/10.1016/S0378-3812\(99\)00262-9](https://doi.org/10.1016/S0378-3812(99)00262-9).
- [58] Giovanni A. Longo, Giulia Righetti, and Claudio Zilio. 'A new computational procedure for refrigerant condensation inside herringbone-type Braze Plate Heat Exchangers'. In: *International Journal of Heat and Mass Transfer* 82 (2015), pp. 530–536. ISSN: 0017-9310. DOI: <https://doi.org/10.1016/j.ijheatmasstransfer.2014.11.032>.
- [59] Ashmore Mawire, Abigail Phori, and Simeon Taole. 'Performance comparison of thermal energy storage oils for solar cookers during charging'. In: *Applied Thermal Engineering* 73.1 (2014), pp. 1323–1331. ISSN: 1359-4311. DOI: <https://doi.org/10.1016/j.applthermaleng.2014.08.032>. URL: <https://www.sciencedirect.com/science/article/pii/S1359431114006942>.

- [60] Ashmore Mawire, Abigail Phori, and Simeon Taole. 'Performance comparison of thermal energy storage oils for solar cookers during charging'. In: *Applied Thermal Engineering* 73.1 (2014), pp. 1323–1331. ISSN: 1359-4311. DOI: <https://doi.org/10.1016/j.applthermaleng.2014.08.032>.
- [61] Mehmet Mercangözü et al. *Electro-thermal energy storage system and method for storing electro-thermal energy*. ABB RESEARCH LTD, European Patent EP2698506A1, Feb. 2014. URL: <https://worldwide.espacenet.com/patent/search?q=pn%3DEP2698506A1>.
- [62] Mehmet Mercangözü et al. 'Electrothermal energy storage with transcritical CO₂ cycles'. In: *Energy* 45.1 (2012), pp. 407–415. ISSN: 0360-5442. DOI: <https://doi.org/10.1016/j.energy.2012.03.013>.
- [63] María E. Mondéjar, Mark O. McLinden, and Eric W. Lemmon. 'Thermodynamic Properties of trans-1-Chloro-3,3,3-trifluoropropane (R1233zd(E)): Vapor Pressure, (p, ρ, T) Behavior, and Speed of Sound Measurements, and Equation of State'. In: *Journal of Chemical & Engineering Data* 60.8 (2015), pp. 2477–2489. DOI: [10.1021/acs.jced.5b00348](https://doi.org/10.1021/acs.jced.5b00348).
- [64] Matteo Morandin et al. 'Conceptual design of a thermo-electrical energy storage system based on heat integration of thermodynamic cycles – Part A: Methodology and base case'. In: *Energy* 45.1 (2012), pp. 375–385. ISSN: 0360-5442. DOI: <https://doi.org/10.1016/j.energy.2012.03.031>.
- [65] Matteo Morandin et al. 'Conceptual design of a thermo-electrical energy storage system based on heat integration of thermodynamic cycles – Part B: Alternative system configurations'. In: *Energy* 45.1 (2012), pp. 386–396. ISSN: 0360-5442. DOI: <https://doi.org/10.1016/j.energy.2012.03.033>.
- [66] Vaclav Novotny et al. 'Review of Carnot Battery Technology Commercial Development'. In: *Energies* 15.2 (2022). ISSN: 1996-1073. URL: <https://www.mdpi.com/1996-1073/15/2/647>.
- [67] Olumide Olumayegun, Meihong Wang, and Greg Kelsall. 'Thermodynamic analysis and preliminary design of closed Brayton cycle using nitrogen as working fluid and coupled to small modular Sodium-cooled fast reactor (SM-SFR)'. In: *Applied Energy* 191 (2017), pp. 436–453. ISSN: 0306-2619. DOI: <https://doi.org/10.1016/j.apenergy.2017.01.099>.
- [68] Andreas V Olympios et al. 'Progress and prospects of thermo-mechanical energy storage—a critical review'. In: *Progress in Energy* 3.2 (Mar. 2021), p. 022001. DOI: [10.1088/2516-1083/abdbba](https://doi.org/10.1088/2516-1083/abdbba).
- [69] Marco Pasetti, Costante M. Invernizzi, and Paolo Iora. 'Thermal stability of working fluids for organic Rankine cycles: An improved survey method and experimental results for cyclopentane, isopentane and n-butane'. In: *Applied Thermal Engineering* 73.1 (2014), pp. 764–774. ISSN: 1359-4311. DOI: <https://doi.org/10.1016/j.applthermaleng.2014.08.017>.
- [70] Ghalya Pikra et al. 'Pressure drop analysis for organic Rankine cycle power generation system using low-grade heat sources'. In: *Case Studies in Thermal Engineering* 32 (2022), p. 101864. ISSN: 2214-157X. DOI: <https://doi.org/10.1016/j.csite.2022.101864>.
- [71] Omar A. Radwan et al. 'Evaluating properties of Arabian desert sands for use in solar thermal technologies'. In: *Solar Energy Materials and Solar Cells* 231 (2021), p. 111335. ISSN: 0927-0248. DOI: <https://doi.org/10.1016/j.solmat.2021.111335>.
- [72] Lewis RI. 'Turbomachinery Performance Analysis'. In: Elsevier Science & Technology Books, May 1996. ISBN: 0340631910.
- [73] T.A. Rigter. *Valorization of waste heat in the food industry. A thermo-economic-environmental analysis of heat recovery technologies in a milk powder factory*. Delft University of Technology, June 2020. URL: <https://repository.tudelft.nl/islandora/object/uuid:c7479ea4-27ae-46bb-bed7-bcc4059a0339/datastream/OBJ/download>.
- [74] Alejandro Rivera-Alvarez et al. 'Predicting the Slope of the Temperature–Entropy Vapor Saturation Curve for Working Fluid Selection Based on Lee–Kesler Modeling'. In: *Industrial & Engineering Chemistry Research* 59.2 (2020), pp. 956–969. DOI: [10.1021/acs.iecr.9b05736](https://doi.org/10.1021/acs.iecr.9b05736). URL: <https://doi.org/10.1021/acs.iecr.9b05736>.
- [75] Jahar Sarkar. 'Review and future trends of supercritical CO₂ Rankine cycle for low-grade heat conversion'. In: *Renewable and Sustainable Energy Reviews* 48 (2015), pp. 434–451. ISSN: 1364-0321. DOI: <https://doi.org/10.1016/j.rser.2015.04.039>.
- [76] G. G. Simeoni et al. 'The Widom line as the crossover between liquid-like and gas-like behaviour in supercritical fluids'. In: *Nature Physics* 6.7 (July 2010), pp. 503–507. ISSN: 1745-2481. DOI: [10.1038/nphys1683](https://doi.org/10.1038/nphys1683).
- [77] Heber Sugo, Erich Kisi, and Dylan Cuskelly. 'Miscibility gap alloys with inverse microstructures and high thermal conductivity for high energy density thermal storage applications'. In: *Applied Thermal Engineering* 51.1 (2013), pp. 1345–1350. ISSN: 1359-4311. DOI: <https://doi.org/10.1016/j.applthermaleng.2012.11.029>.

- [78] Xuan Tao and Carlos A. Infante Ferreira. 'Heat transfer and frictional pressure drop during condensation in plate heat exchangers: Assessment of correlations and a new method'. In: *International Journal of Heat and Mass Transfer* 135 (2019), pp. 996–1012. ISSN: 0017-9310. DOI: <https://doi.org/10.1016/j.ijheatmasstransfer.2019.01.132>.
- [79] *Technical comparisons: Combustion engines and gas turbines*. WARTSILA. URL: <https://www.wartsila.com/energy/learn-more/technical-comparisons/gas-turbine-for-power-generation-introduction>.
- [80] H. Tian and G.Q. Shu. '17 - Organic Rankine Cycle systems for large-scale waste heat recovery to produce electricity'. In: *Organic Rankine Cycle (ORC) Power Systems*. Ed. by Ennio Macchi and Marco Astolfi. Woodhead Publishing, 2017, pp. 613–636. ISBN: 978-0-08-100510-1. DOI: <https://doi.org/10.1016/B978-0-08-100510-1.00017-X>.
- [81] Gavin Towler and Ray Sinnott. 'Chapter 19 - Heat-Transfer Equipment'. In: *Chemical Engineering Design (Second Edition)*. 2013, pp. 1047–1205. ISBN: 978-0-08-096659-5. DOI: <https://doi.org/10.1016/B978-0-08-096659-5.00019-5>.
- [82] Guido Van Rossum and Fred L. Drake. *Python 3 Reference Manual*. Scotts Valley, CA: CreateSpace, 2009. ISBN: 1441412697.
- [83] Pauli Virtanen et al. 'SciPy 1.0: Fundamental Algorithms for Scientific Computing in Python'. In: *Nature Methods* 17 (2020), pp. 261–272. DOI: [10.1038/s41592-019-0686-2](https://doi.org/10.1038/s41592-019-0686-2).
- [84] Dongxiang Wang et al. 'Efficiency and optimal performance evaluation of organic Rankine cycle for low grade waste heat power generation'. In: *Energy* 50 (2013), pp. 343–352. ISSN: 0360-5442. DOI: <https://doi.org/10.1016/j.energy.2012.11.010>.
- [85] Hanwei Wang et al. 'A Comparison of Partial Admission Axial and Radial Inflow Turbines for Underwater Vehicles'. In: *Energies* 14 (Mar. 2021), p. 1514. DOI: [10.3390/en14051514](https://doi.org/10.3390/en14051514).
- [86] *Waste heat from data centres*. URL: <https://celsiuscity.eu/wp-content/uploads/2020/06/Waste-heat-from-data-centres.pdf>.
- [87] R. L. Webb. 'Convective Condensation of Superheated Vapor'. In: *Journal of Heat Transfer* 120.2 (May 1998), pp. 418–421. ISSN: 0022-1481. DOI: [10.1115/1.2824266](https://doi.org/10.1115/1.2824266).
- [88] *WHY ARE MISCIBILITY GAP ALLOYS A SUPERIOR TECHNOLOGY?* URL: <https://miscibilitygapalloy.blogspot.com/p/advantages.html>.
- [89] D. Winkelmann. *Condensation of pure refrigerants and their zeotropic mixtures in plate heat exchangers*. Technical University of Berlin, 2010.
- [90] Y.-Y. Yan and T.-F. Lin. 'Evaporation Heat Transfer and Pressure Drop of Refrigerant R-134a in a Plate Heat Exchanger'. In: *Journal of Heat Transfer* 121.1 (Feb. 1999), pp. 118–127. ISSN: 0022-1481. DOI: [10.1115/1.2825924](https://doi.org/10.1115/1.2825924).
- [91] Ahmet Yasli and Nemika Cellatoğlu. 'FEASIBILITY ANALYSIS OF DUAL ENERGY SYSTEMS: A CASE STUDY OF NORTHERN CYPRUS'. In: Nov. 2010. URL: https://www.researchgate.net/publication/325035854_FEASIBILITY_ANALYSIS_OF_DUAL_ENERGY_SYSTEMS_A_CASE_STUDY_OF_NORTHERN_CYPRUS/stats.
- [92] Yong Zhou et al. 'An Equation of State for the Thermodynamic Properties of Cyclohexane'. In: *Journal of Physical and Chemical Reference Data* (2014). DOI: <https://doi.org/10.1063/1.4900538>.
- [93] Chenyang Zhu et al. 'A comprehensive study on thermophysical properties of carbon dioxide through the Cubic-Plus-Association and crossover Cubic-Plus-Association equations of state'. In: *Journal of Chemical & Engineering Data* 65.9 (2020), pp. 4268–4284. DOI: [10.1021/acs.jced.0c00236](https://doi.org/10.1021/acs.jced.0c00236).